UNIVERSITÀ DELLA CALABRIA

UNIVERSITA' DELLA CALABRIA

Dipartimento di Fisica

Scuola di Dottorato

Bernardino Telesio - Scuola di Scienza e Tecnica

Indirizzo

Fisica dei Sistemi Complessi

Con il contributo di

Consiglio Nazionale delle Ricerche

Istituto di Scienze dell'Atmosfera e del Clima

CICLO

XXVII

A study of wind behavior from the micro to the mesoscale of different temporal and spatial horizons: turbulent regime, mean and climate

Settore Scientifico Disciplinare: FIS/07

Direttore: Prof. Roberto Bartolino

Firma _____

Supervisori: Dott.ssa Anna Maria Sempreviva

Firma _____

Prof. Vincenzo Carbone

Firma _____

Dottorando: Dott. Luca Tiriolo

Firma _____

Contents

List of Figures

List of Tables

Summary

This work presents three scales in order to describe wind phenomena: spatial: few meters; half hour velocity: turbulence and intermittent actions; 150 m atmospheric range wind profiles of semi empirical laws and the use of Regional Weather Forecast System (RAMS); and finally decade long data synoptic analysis of extreme events.
The results support the hypothesis about the necessity of the study of broad view wind phenomenology in all scales. A single high resolution comprehensive model is not sufficient to reproduce the effects of wind due to conformation and stability conditions.
On the other hand, a semi-empirical model based on a reasonable number of parameters collected on the ground, which also takes account of the effects of turbulence can never be self-consistent: it does not contain information about large atmospheric circulations that are the main channel of kinetic energy transport and thermal energy input on a local scale.
The following conclusion comes from deviation analysis between field and model observations; typical large, medium and small scales physical laws tend to describe most of the phenomena; however, ground conformation, obstacles and unpredictable atmospheric instability generate strong deviations from the models.
The choice of limiting the investigation only on one scale gives rise to a lack of the aforesaid differences. That is why it is necessary to extend the investigation to many different fields together; this work presents methods, techniques, case studies and particular examples. They are all intended to provide a set of useful tools for studying the behavior of the wind on any site of interest.
The presented concepts can be applied to many fields, one of which is the use of wind as a renewable source of energy. In this case we present an application within the verification model (Chapter 5). When the total energy output of a power plant spread over a fairly large area (about 100 km radius) is available and the individual production of each wind turbine is unknowing, a methodology to estimate energy production can be created. Using 90% of samples available a power curve is obtained and then applied for the remaining data. The result gives an error of about 20%: this methodology can be improved by applying the other smaller scales survey instruments for the output of energy analysis from individual wind turbines.For the single blade we have to consider wind evolution altitude and deviation due to atmospheric phenomena of stability, to particular orographic conditions, but also to sudden velocity variations on small scale atmospheric turbulence. In short, studying turbulence means to know how the energy is distributed from large to small scales; applying this to a wind turbine means understanding how much energy can

be converted into electrical energy and how much of it is dissipated due to resistance in the rotor hub and damage in the structure. Similar remarks along these lines could be made with regard to feasibility studies of bridges, skyscrapers and tall structures in general.
Finally, a study on 30 years of climatological data simulated by the meteorological model was carried out: it was done to show how wind direction and, therefore, the origin of the perturbation can have the same impact on even distant Italian regions. This conclusion brings interesting observations on the characterization of homogeneous climatic areas.

Sommario

In questo lavoro sono stati presentati delle metodologie per descrivere il fenomeno vento in tre differenti scale: su scale spaziali dell'ordine di qualche metro studiando l'azione della turbolenza e dell'intermittenza all'interno di campioni di velocità raccolti alla mezz' ora; su scale intermedie considerando l'evoluzione in quote non superiori ai 150 m attraverso previsioni create da leggi semi-empiriche e da sistemi di previsioni atmosferica; infine quella sinottica, analizzando eventi estremi su una base pluridecennale di dati.
Il risultato che ne consegue tende a sostenere l'ipotesi che è necessaria un'ampia visione della problematica per descrivere il comportamento del vento. Non è sufficiente basarsi su un modello, anche per alte risoluzioni, per poter riprodurre gli effetti del vento su un edificio, un ponte o una pala eolica perchè sono le condizioni stesse del territorio che cambiano, accelerano o fermano la sua azione; d'altra parte un modello semi-empirico basato su un numero ragionevole di parametri raccolti a terra, che tiene conto anche degli effetti sulla turbolenza non può mai essere autoconsistente in quanto non contiene informazioni sulle grande circolazioni atmosferiche che sono il principale canale di immissione per il trasporto di energia cinetica e termica nella scala locale.
Questa conclusione nasce dall'analisi del discostamento delle osservazioni dai modelli: anche se per la maggior parte dei casi e del tempo le leggi fisiche tipiche delle grandi, medio e piccole scale tendono a riprodurre la maggior parte dei fenomeni, la particolare conformazione del terreno, la presenza di ostacoli, la non prevedibile instabilità atmosferica generano forti discostamenti dai modelli. Quest'ultime differenze sono, appunto dovute, alla scelta di limitare l'indagine su una scala soltanto: ecco quindi la necessità, nata in questo lavoro, di ampliare le indagini anche su campi molti diversi fra loro. Sono stati quindi illustrate metodologie, tecniche, casi studio e situazioni particolari che vogliono costituire un set di utili strumenti per studiare il comportamento del vento su ogni tipo di sito di interesse.
Tutti i concetti qui presentati possono trovare applicazione in molteplici campi: il più immediato è quello della verifica da modello (RAMS cap. 5) relativo all'applicazione del vento come fonte rinnovabile di energia. Pur avendo a disposizione l'output energetico totale di un impianto energetico distribuito su un territorio piuttosto ampio (intorno ai 100 km di raggio) e non conoscendo la singola produzione di ciascuna pala eolica, è stata creata una metodologia *ad hoc* per creare una curva di potenza globale e stimare la previsione della produzione energetica su un periodo noto. Il risultato ha dato un errore di circa il 20% delle previsioni rispetto le osservazioni: ulteriori approfondimenti possono essere effettuatu

applicando anche gli altri strumenti di indagine adottati su scale più piccole nell'eventuale analisi di output energetici da singoli aerogeneratori. Per quanto riguarda la singola pala ci sono infatti da considerare sia l'evoluzione del vento con la quota e la sua deviazione per via di fenomeni di stabilità atmosferica e di particolari condizioni orografici, ma anche delle improvvise variazioni di velocità dello stesso sulle piccole scale dovuta alla turbolenza atmosferica. In poche parole studiare la turbolenza significa studiare come l'energia si distribuisce dalle grandi alle piccole scale e applicarlo ad una pala eolica significa capire quanta di questa energia può essere trasformata in energia elettrica e quanta invece causa, ad esempio, resistenza nel mozzo del rotore della pala e eventuali danni nella struttura. Discorsi analoghi su questa scia possono essere fatti per quanto riguarda studi di fattibilità di ponti, grattacieli e alte strutture in genere.
Infine, è stato realizzato uno studio climatologico su 30 anni di dati simulati tramite modello meteorologico: ciò è stato fatto per dimostrare come la direzione di provenienza del vento e, quindi, l'origine della perturbazione posso avere lo stesso impatto in regioni italiani anche distanti fra loro. Tale conclusione porta interessanti considerazioni sulla caratterizzazione di aree climatologicamente omogenee dal punto di vista della loro ventosità.

Ringraziamenti

Questo lavoro è stato un percorso, una sfida, una passione, una fatica, una definizione di me stesso, un canto e un grido; ma sarebbe stato solo un mucchio di parole al “vento"" senza l’aiuto di tutti quelli che mi hanno teso la mano durante questo cammino.
Innanzitutto ringrazio la mia relatrice, la Dott.ssa Anna Maria Sempreviva: è stata lei a spalancare per me le porte della fisica del boundary layer. Il suo animo mai stanco e sempre in movimento, mi ha indicato che la ricerca è il viaggio.
Sono grato anche al co-relatore Prof. Vincenzo Carbone, scienziato eclettico, puntuale e stimolante; da lui ho appreso gli strumenti, la fervente curiosità e la consapevolezza che nel caos della turbolenza, l’ordine c’è e può essere studiato.
Proseguo i miei ringraziamenti con la Dott.ssa Claudia Roberta Calidonna, figura preziosa e essenziale nel mia esperienza all’ISAC-CNR di Lamezia Terme; motore continuo, ha incanalato questa tesi con consigli sempre molto validi.
Ringrazio di tutto cuore il Dott. Stefano Federico, che mi ha accompagnato nel mondo delle simulazioni numeriche e dei loro errori; Fabio Lepreti, che ha avuto la pazienza di rispondere alle mie domande e ai miei dubbi; le mie colleghe Claudia e Stefania, con cui ho condiviso stanza, stress e passione nell’apprendimento; Daniel, Elenio, Teresa, Manuela e Maria Francesca, veri esempi di professionalità e dispensatori mai stanchi di aiuto e di utilissimi suggerimenti.
Ha tutta la mia gratitudine anche il Prof. Rino Sia che mi ha aiutato a trasformare pensieri vaghi in frasi di senso compiuto, grazie alla sua straordinaria esperienza nella lingua anglosassone.
Ho il forte desiderio di ringraziare i miei genitori perchè hanno dato e continuano a dare la loro vita per me e per i miei fratelli; anche voi, Roberto e Matteo vi sono grato per tutto il sostegno morale e materiale che gratuitamente mi avete donato.
Don Francesco, Don Mimmo, Don Sandro, Don Gesualdo, Don Davide, le vostre preghiere hanno dato frutto e vi ringrazio per questo.
Dulcis in fundo, ricordo nei miei ringraziamenti la mia cara Valeria, vero ciclone umano in grado di trasmettere forza, vita, passione, amore, compassione e gioia a tutto ciò che la circonda: grazie per avermi sostenuto e per non smettere mai di starmi vicino.

Chapter 1

Introduction

1.1 Background

Studying wind means also to understand how a real fluid moves in a system that changes and that interacts with other system. Wind is important to mitigate temperature and transport hot or cold air that made a perfect but delicate equilibrium in innumerable processes.
Wind is used also to create electric energy for our work, for our houses, for the transport and so on. Windmills were used for centuries to extract kinetic power and transform it into mechanical power. And on the last part of the 19^{th} century it became the source of mechanical power of some industries in central Europe. Since the year 2000 the production of the wind power as a source of electric power has grown exponentially and nowadays wind power industry is considered one of the most promising industries of the word. The possibility to harvest energy from the wind is necessarily subject to an estimation of its strength, its persistence and the turbulence it generates.

1.2 Aim

The aim of this work it is to demonstrate that to understand deeply the behavior of wind, it is necessary to considered all the scales interested by this phenomenon: to do this three different examples are presented. First we address the smaller scale i.e. local scale (around 1 m) where the principal variation on wind evolution is created by intermittency, i.e. by the irregular distribution of energy from large to small scale, typical on turbulent fluid. For intermediate scales (around) semi-empirical laws are used to simulate the wind behavior to ground level until 150 meters for all the seasons and for different stability conditions: all the laws are verified using data collected from a wind Lidar installed on Institute of Atmospheric Science and Climate (ISAC) of the Italian National Council of Researches (CNR) of Lamezia Terme (CZ). In the same scale also a verification with a Regional Atmospheric Model System (RAMS) was made. At the end we will show methodologies

to made a climatology characterization of Italy regions in order to separate homogeneous zone interested by the same perturbation for most of the time on a simulated sample of thirty years.

1.3 The influence of turbulence

Atmospheric turbulence in the surface layer that is the lowest part of the planetary boundary layer (PBL), is very different from the above layers. The radiation coming from the sun heats the surface and, for convection, the air above it becomes warmer and more buoyant. Going up toward the atmosphere, the air parcel colds down and, in the same time, becomes denser: if it becomes denser and colder than air surrounding, parcel goes down toward the soil. At each point of his ascendent and then descendent trajectory there are three different situation that depend on balance between air parcel temperature (T_p) and surrounding environment temperature T_e: if the temperature difference is positive $T_p > T_e$ the parcel is positively buoyant, it is less dense and will rise. With $T_p < T_e$ the parcel is negatively buoyant, it is more dense and will sink. Finally if $T_p = T_e$ the parcel is neutrally buoyant, it will not rise or sink. From these considerations it is possible to link temperature gradient to stability condition defined as resistance of the atmosphere to vertical motion B. [6]. For each case, respectively corresponds a instability situation($T_p > T_e$: the parcel diverges from equilibrium position), stability situation ($T_p < T_e$: if the trajectory of the particle undergoes a deviation it tends to return to the equilibrium position) and neutral situation ($T_p = T_e$: an intermediate phase).
All this causes the formation of particular structure, called eddies. Each eddy is then looked upon as a a parcel of air or turbulent blob, over which the temperature, moisture, flow velocity and other quantities deviates from average. In general, turbulence effects are considered to be isotropic for eddy sizes less than some value L called the outer scale of turbulence.
These structure are initially fed by energy from wind shear and convective heating from ground: when this energy exceeds a critical level defined by the Reynold's number, they break up into smaller and smaller eddies gradually. This energy cascade occurs until, for very small eddies, viscous effect became important and the energy is dissipated. This viscous dissipation begins for eddies smaller than some value l_0, called the inner scale of turbulence.
Between these two scales there is a interval where the passage of energy from large to small eddies where it is possible to ignore effect of inner and dissipation scales: this interval is called inertial range. Studies of Kolmogorov (Kolmogorov [44]) in this particular interval reveal that it is possible to describe the energy cascade with a power law: this is a reference law to analyze the phenomenon of intermittency, i.e. the dispersion energy between the turbulent eddies. From this basis, and through the use of advanced analytical techniques such as structure functions (Milan et al. [51]) it was possible, therefore, to characterize the turbulence in various scales and then deal with, in a quantitative way, the impact that turbulence can have on a structure. The study on turbulence was made in collaboration

with University of Calabria (UNICAL) of Cosenza and, in particular, with the research group of Prof. Vincenzo Carbone on fluid turbulence: it is presented on Chap. 2 and Chap. 3.

1.4 Wind profile in atmospheric boundary layer

The mean wind regime is that most studied simple because, in this scale, the variation of wind speed with height affects their daily lives. The nature of variation on profile dictates the structure of buildings, bridges, snow fences, wind breaks, pollutant dispersion, and wind turbines, for example. As introduced in the previous paragraph, studying evolution of wind on stability conditions means follows trajectory of air parcel in quote. To create a complete and representative model the evolution of scaling parameters of surface boundary layer are reproduced .
First of all we define atmospheric boundary layer (ABL) using the two concept analyzed by Sutton (1953) Sutton [66]:

- A surface layer region 50-100 m deep of approximately constant (in the vertical) shearing stress, where the flow is insensitive to the earth's rotation and the wind structure is determined primarily by surface friction and the vertical gradient of temperature.

- a region above that layer extending to a height of 500-1000 m, where the shearing stress is variable and the wind structure is influenced by surface friction, temperature gradient, and the earth'rotation.

Based on this definition, in addition to the aforementioned temperature gradients and vertical speeds an other important scale parameter to consider is the friction velocity u^*. The friction velocity (also known as the shear-stress velocity), u^*, of a flow is defined by the relation:

$$u^* = \sqrt{\frac{\tau}{\rho}} \tag{1.1}$$

where τ is the shear stress and ρ the fluid density. This quantities give a measure of the effect on the forces caused by interaction between air and land, sea, lakes and so on, on the ground.
The interaction among all this parameters and their influence of variation on stability condition could be studied considering the Obukhov length defined as a ratio between the mechanical production of turbulence by shear flows and by buoyancy driven by heat flux. Finally this quantities determinate the stability category and then set what are the best laws to reproduce the wind behavior.
Using a set of heterogeneous data acquired in different sites and times, it was possible to create a model based on semi-empirical laws to simulate scale parameters for a complete

description of evolution of wind and turbulence up to 150 m to soil. All the scale parameters are verified, and the final output, i.e. wind velocities are compared with observed data acquired by a wind Lidar placed on UOS ISAC-CNR at Lamezia Terme (Chap.4). All the work is a portion of that made for a scientific advisory agreement between ISAC and University of Reggio Calabria inside the project PON A300308 GELMINCAL "Generatore Eolico a Levitazione Magnetica in Calabria".

1.5 Model

Considering bigger scales, we have been investigated the performance for a regional weather forecasting systems, using data from Global Telecommunication System (GTS) on the South Italy. In the case of a system for forecasting atmospheric, algorithms are constituted by the set of partial differential equations describing the dynamics of the atmosphere. The data input of the regional model are the output of global model, in our case the European Centre for Medium-Range Weather Forecasts (ECMWF).
The goal of a prediction is to provide, after the calculations, wind speed, temperature, pressure, humidity at various heights from the ground. From these we can then derive all other dependent variables such as precipitation, cloudiness, and others. The main equations used by the model are:

- Navier-Stokes equations for the definition of the components of the wind field (also called balance equations of momentum in a fluid).

- Equation of thermodynamics (the first fundamental law of thermodynamics, also known as energy conservation).

- Equation of evolution of water vapor (takes account of all processes that make up the water cycle and its state transitions, that is, evaporation, condensation, melting, solidification and sublimation).

- Continuity equation (which is derived from the law of conservation of mass). It ensures that in a given volume the amount of air that enters is equal to that leaving.

At these, we have to consider also conservative prognostic equations, namely equations where the time dependency are explicit. They are:

- Equation of state of gas, which binds pressure, density, temperature and volume of an air mass.

- Hydrostatic equation, which relates the approximate relationship between the pressure variation with altitude and air density.

The Navier - Stokes equations are used to define the components of the wind field. The resolution of the system of equations is obtained by decoupling the movement of the air mass along the horizontal planes,that they are described by Navier-Stokes equations, than along the vertical axis (upward movements of thermal currents) described by balance equations heat. The calculation accuracy is intrinsically linked at the density point of the grid used by the numerical scheme as a result of the system discretization of the equations. To solve the flow field in its smallest details you should use a dense grid dramatically increasing resources and computation time. In this work we used a 3 km resolution grid to test the performance of the model on a one year period (1 December 2012 - 30 November 2013) for temperature, relative humidity, wind speed and direction (Chap. 5): after this verification, we have used the model to show a new methodology to predict wind power energy. This last has been compared with power output observed by a wind plant placed in the middle of Italy.
The data simulated by the model RAMS are obtained inside a nation project PON04a2E "Res Novae", that permits us to acquire resources and instruments that realized this research.

1.6 Map of extreme events

To characterize a site and the behavior of wind on it, it is also necessary study the climatology of wind. In Italy there is a standard procedure given in Ballio et al. [8] and Ballio et al. [9] where, starting from consideration of extreme winds, standard procedures to divide the peninsula in well defined wind areas are proposed. Unfortunately these procedures does not take into account the phenomena that provide to generate perturbation. In this thesis an attempt to provide an alternative method for zoning Italy according to different origin conditions of the perturbations is presented.
Also this work like, the model on wind profiles, is just a little part of that made for a scientific advisory agreement between ISAC and University of Reggio Calabria inside the project PON A300308 GELMINCAL - "Generatore Eolico a Levitazione Magnetica in Calabria".

Chapter 2

Turbulence

Turbulence is caused by a non-stationary irregular motion in a fluid. A fluid could be considered chaotic if a little oscillation of his trajectory causes high-amplitude fluctuation. This reason explains also how a gas could be diffuse in a time lesser than same defined from its intrinsic velocity.
A typical example of this is the diffusion of a gas in a limited portion of space: if we image spraying a perfume in a room, it's common experience that, in few seconds, the presence of perfume could be perceive throughout the room. At first guess, someone could consider that the perfume has spread everywhere for the phenomenon of diffusion. A simple count excludes this conclusion: if we define ν and L respectively the air kinematic viscosity and the distance traveled by perfume, the time taken to travel this distance is $T_\nu = L^2/\nu$ that, utilizing air data ($\nu = 2.3 \cdot 10^{-6} m^2/s$) and considering $L = 4\ m$ gives $T_\nu \simeq 7 \cdot 10^6 s$ (almost 80 days).
Indeed we should consider not ν (quantity for the air momentum), but the diffusivity of perfume in air $\kappa = \nu/Sc$ (being $Sc = 0.7$ the Schmidt number for air): in this way we have $T_\kappa \sim 56$ days, even too large comparing with the real experience. We could consider also the natural convection caused by difference of temperature between air and perfume, but anyhow we have velocity of few cm/s direct upwards and then a time scale of hours.
The real reason is inside the presence of turbulence: velocity fluctuations caused by turbulent motion of fluid are able to transport a quantity (scalar or vector) very fast, also without mean horizontal motion. This causes a increment of velocity of two-three order of magnitude on velocity respect diffusivity.
Also with these simple considerations, it is clear how turbulence could be very important in the study of air motion in atmosphere: in particular we are interest to show how the energy is distributed to the large scale at the smaller scale, and how the turbulence influence this cascade in different wind regimes and stability conditions. In few words we are interest to show that we have not consider only the advection of wind (and eventually a wind energy production), but we need concepts like intermittency, isotropic and homogeneous turbulence, inertial range to characterize, to predict the behavior of wind, at least the necessary,.
A brief explanation and the fundamental relations used in this work are shown in this

chapter. All the pictures here below are made using data from Lamezia Terme campaign of 2009: other information about this data are reported in the next chapter (Chap. 3).

2.1 The Reynolds number

The motion of a viscous and incompressible fluid should have two different regimes: laminar, when a fluid flows in parallel layers, with no disruption between the layers, and turbulent, when fluid velocities have changing direction with time and then a whirling motion.
Experimentally it is possible to observe that, under some conditions, laminar flux could be make on turbulent motion. Osborne Reynolds, around 1883, studied experimentally and theoretically the nature of these conditions: through experiments in which a flow of colored water of adjustable speed, he derived the formula of a dimensionless parameter that characterizes the type of fluid motion:

$$N_R = \frac{\rho \langle V \rangle L}{\mu} \tag{2.1}$$

This number is called the Reynolds number. In the formula, $\langle V \rangle$ is the average fluid velocity with respect to the solid with which it is in contact, ρ is density, μ is the viscosity coefficient and L is the characteristic scale of the solid (for a cylindrical pipe, for example, the latter may be identified with the diameter). Reynolds showed that the behavior of a fluid could be categorized in three cases:

- for $R \leq 2100$ flow can be defined as stationary. Fluid appears as a ensemble of laminae (from which the term laminar flow) flowed over each other only through interacting of the tangential stresses. This behavior was noted by observing the evolution of a ink streak line released from a fixed position inside the pipe; in fact, the line of colorant rectilinear flows away from the source spreading very weakly.

- Reynolds observed that for $2100 \leq R \leq 4000$ line of colorant lost its stationarity and it propagates along a wavy path with time-dependent characteristics. In this transitional regime, however, the trace of colorant preserves its spatial coherence staying in a thin line.

- for R$>$ 4000, after an initial stretch with oscillations of amplitude growing, the trace of ink was spread vigorously throughout the cross section of the tube not to be distributed homogeneously throughout the flow. The latter regime is called turbulent and it is characterized by a disordered motion, fully three-dimensional and unsteady, and gives the velocity fluctuations with non-deterministic characteristics.

2.2 The open question of Navier-Stokes equations

Another feature common to all turbulent flows is the following: if it repeats the same experiment, and measure the same quantity at the same point for the same time inter-

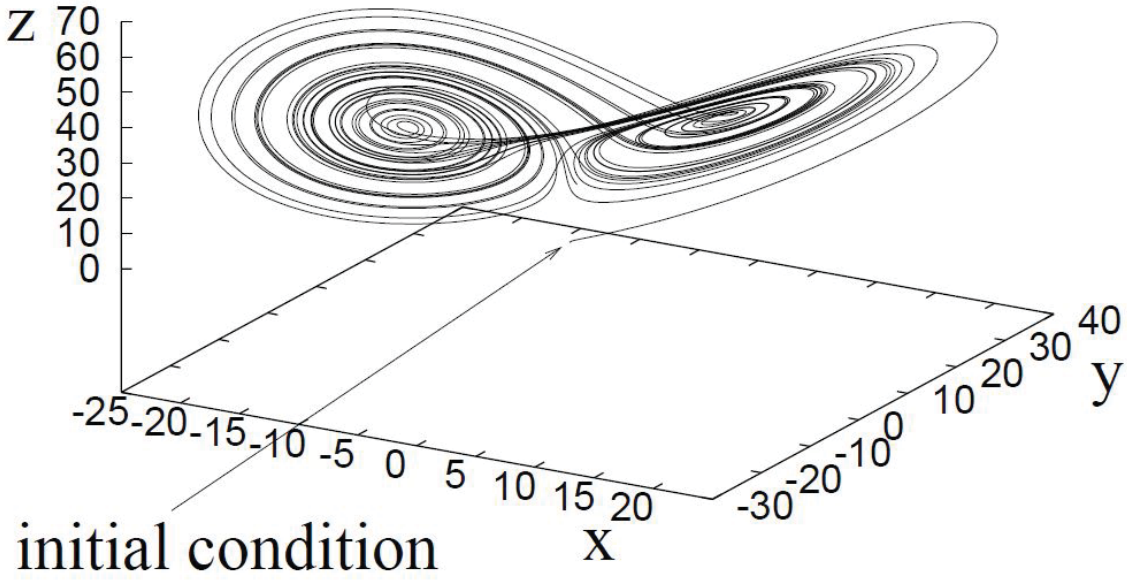

Figure 2.1: Lorentz attractor for the tridimensional space x, y, z

val, all the measure obtained are significantly different when compared time by time, but they have the same statistical characteristics (mean value , standard deviation, etc.). This observation seems at first sight irreconcilable with the nature of the equations governing the phenomenon, namely the Navier-Stokes equations; this equations are deterministic, and then, for fixed initial conditions the solution must be well determined in space and time. This dilemma was solved by Lorentz in 1963 showed that some nonlinear systems have a particular sensitivity to initial conditions: a little perturbations at the boundary counditions provide solutions also completely different.
To understand this conclusion, let consider a classical [1] example. If we consider the following equation:

$$\dot{x} = \sigma(y - x), \dot{y} = \rho x - y - xz, \dot{z} = -\beta z + xy, \tag{2.2}$$

where $\sigma = 10, \beta = 8/3$ and $\rho = 35$ with the initial condition $x(0) = 0.5$, $y(0) = 0.1$ e $z(0) = 0.3$; the solution of this system is the famous Lorentz attractor (Fig. 2.1). On the other side, if we consider the initial conditions $x(0) = 0.5, y(0) = 0.100001$ and $z(0) = 0.3$ we note that, after a little initial time (in this case $t \geq 15$ but it depends on initial conditions and on σ,β and ρ) the two solutions are different and could be compared each other only on mean values and on fluctuation amplitudes (Fig. 2.1).

[1] This example is a extract of "Turbulent Flows" by S.B. Pope, Cambridge Univ. Press, 2000.

2.3 Navier-Stokes Equations

As the equation 2.2, also the Navier-Stokes equations have the same behavior. Let consider these equations:

$$\frac{\partial \mathbf{u} \partial t}{+}(\mathbf{u} \cdot \nabla)\mathbf{u} = -\frac{1}{\rho}\nabla p + \gamma \nabla^2 \mathbf{u} + \frac{1}{\rho}\mathbf{F} \tag{2.3}$$

Here $\otimes$ denotes the tensorial product. A double bar denotes a tensor. How it is possible to see, the initial parameter for these equation are: velocity field $\overrightarrow{u}$, pressure p, space geometry and nature of fluid (given by viscosity γ, density ρ and body forces f), but also the initial temperature distribution, that it is not directly express by 2.3, that it is important to define γ. Temperature and body forces f could not be controlled with infinite precision and this caused, through the no-linearity of the equations, a not deterministic solution. In other words, as we try to maintain controlled all the parameters of an experiment, two subsequent realizations of the same phenomenon with initial conditions replicated with infinite precision for Reynolds numbers sufficiently large, have divergent solutions in time. The no-linear term of 2.3 are also responsible of local velocities fluctuations and they create fluid-dynamical structures on little scales. Come back at example with the ink, a little variation on the initial field causes only a variation on mean motion, meanwhile the ink dispersion on fluid could be caused by the action of little structure respect the typical fluid scale, to local mix the colorant with all fluid.
For this reason, to understand the fluid motion in turbulent regime it is necessary study how the bigger scales feed the littler scales: furthermore only an statistical approach can provide an global comprehension because of non-determinist solution of Navier-Stokes equations.

2.4 Structure Functions

Great success in the field of turbulence was obtained by Kolmogorov in 1941 (Kolmogorov [44]), when he looked for a statistical description of the homogeneous and isotropic turbulence based on a few simple assumptions of similarity. The Russian mathematician realized that the time evolution of a turbulent signal shows a large variability, but there are particular lengths and correlation times that are easy to describe with simple laws.
To understand this Kolmogorov's vision of turbulence, we have to define the n-point correlation tensor as the mean value of n functions defined in different time and positions

$$\langle f_1(x_1, t_1) ... f_n(x_n, t_n) \rangle \tag{2.4}$$

where the operator $\langle . \rangle$ indicates the mean of the functions. Meanwhile the correlation tensor of the second order with velocity fluctuations at two points and at three points are, respectively

$$Q_{ij}(\mathbf{x}, \mathbf{x}', t_1, t_2) = \langle v'(\mathbf{x}, t_1) v'(\mathbf{x}, t_1) \rangle \tag{2.5}$$

$$S_{ijk}(\mathbf{x}, \mathbf{x}', t) = \langle v_i(\mathbf{x}, t) v_j(\mathbf{x}, t) v_k(\mathbf{x}, t) \rangle \tag{2.6}$$

where $v_i' = v_i - \langle v_i \rangle$. The tensor Q_{ij} provides an indication of the closeness, in statistical sense, between two velocity components at two points or to two different instants. The choice $t_1 = t_2$ could be useful to identify the structures, their spatial form, their size features: for distances $|\mathbf{x}' - \mathbf{x}|$ smaller than the spatial correlation length of the value will be next to v_0^2 (assuming that the speed is function continues in space), while for value larger than the correlation becomes negligible. In turbulence the spatial correlation length is very small compared to the size of the fluid and it is know as spatial chaos. If $\mathbf{x} = \mathbf{x}'$ Q_{ij} is called auto-correlation, and provides a quantitative value of the correlation time of the turbulent signal: if $t_1 - t_2 \ll$ then the speeds are highly correlated. For $t_2 - t_1 \gg$ the two quantities are practically uncorrelated because of the turbulent motion variability. We can, also, define correlation time t_c as the interval separating the time on what the auto-correlation assume a finite value by those in which it is close to zero. In the fully developed turbulence, t_c is much smaller than the time scales on which features you want to study the system and it is a measure of temporal chaos.
At this point we can define the n-order structure function S_n are the two time-points function correlation of a function f as

$$S_n = \langle [f(x, t+\tau) - f(x,t)] \rangle \tag{2.7}$$

In our study we are interest to investigate the behavior the wind speed in the different condition and for this, we found that it is very instructive to use the velocity increments $\delta v(x,t,\tau) = v(x,t+\tau) - v(x,t)$: in this way it is possible to understood how the velocity vortices, or *eddies*, evolve in analyzed atmospheric portion.
Using the versor $\boldsymbol{e}$ along the mainstream wind component, the p-order structure function for velocity increments could be written as

$$S_p(x, \mathbf{e}, t, \tau) = \langle [\delta v(x,t,\tau) \cdot \boldsymbol{e}] \rangle \tag{2.8}$$

We can define *homogeneous* turbulence if all the ensemble mean are invariant respect spatial translation. In other words the second-order correlation tensor depend only by relative position of two points

$$Q_{ij}(\mathbf{x}, \mathbf{x'}, t_1, t_2) = Q_{ij}(\mathbf{r}, t_1, t_2) \tag{2.9}$$

and

$$Q_{ij}(\mathbf{r}) = Q_{ij}(-\mathbf{r}) \tag{2.10}$$

with $\mathbf{r} = \mathbf{x}' - \mathbf{x}$. Similarly the structure function S_p not depend on the x coordinate:

$$S_p(\mathbf{r}, \mathbf{e}, t) = \langle [\delta v(\mathbf{r}, \mathbf{e}, \mathbf{t}] \rangle \tag{2.11}$$

The turbulence is *isotropic* if all ensemble means have the property of invariance under rotations. If we have homogenous and isotropic turbulence then we can define the p-order structure function as a simple function of t and the delay time τ

$$S_p(t, \tau) = \langle [\delta u_l(t,\tau)]^p \rangle \tag{2.12}$$

In the Fig. 2.2 it is possible to match the first five order structure functions for stable atmospheric condition measured in a synoptic regime.

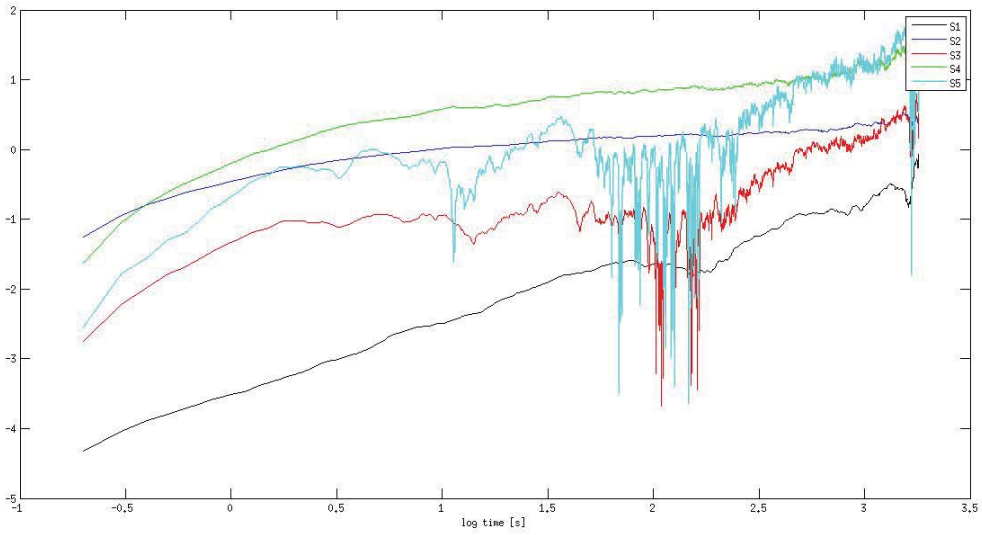

Figure 2.2: Structure function from order 1 to 5 against incremental time from wind speed incremental. These functions are calculated for the stable atmospheric condition in synoptic regime.

2.5 Scales of turbulence and Intermittency

In a fluid we could be considered a list of typical scales: the largest is L_0 that is the outer scale of turbulence where there is the energy input; at the opposite, there is l_0, the little one, where viscous effect becomes important and the energy can be efficiently dissipated. At the fist scale, the fluid is feeding by largest eddies, caused by the largest turbulence fluctuation. These eddies are unstable and thus disappear, transferring their energy to smaller eddies with a efficiency that is related at Reynolds number; if this number is high (depending on the nature of the fluid) the energy cannot be efficiently dissipated and non-linear effect play to distribute in non Gaussian way the energy at smaller scale. Anyway this process is repeated until sufficiently small sizes are reached for viscosity to become significant, and energy is dissipated into heat.
The most important concept in this perspective is that, at intermediate scales $L_0 \ll l \ll l_0$, fluid could be considered far from both than input scale than dissipation scale, and then it is unruffled by these two phenomena: in this case the intermediate scales are the so-called inertial regime, and they are characterized only by action of the inertial terms of the Navier-Stokes equation. In this range, at very high Reynolds number, Kolmogorov found that the averaged square of longitudinal velocity increments follow a power law.

Formally this scaling law for the second-order moment of fluctuations, should leads to the conjecture that all moments of fluctuation, i.e. the p-th order structure function 2.12

must scales as $p/3$

$$S_p(l) = C_p \epsilon^{p/3} l^{p/3} \tag{2.13}$$

for any positive integer p. The case $p = 3$ deserves special mention because Kolmogorov showed that this function is proportional at the scale length of observation

$$S_3(l) = -\frac{4}{5}\epsilon l \tag{2.14}$$

This last equation and one of its consequences, namely that the energy spectrum of turbulence should follow a $k^{-5/3}$ law (where k is the wavenumber) is reasonably well supported by data.
In Fig. 2.3 there is a example of third-order structure function that shows a inertial range. In this plot we can see that in the range $[0.428, 4.276]$ Eq. (2.14) is valid to reproduce the data: this is the inertial range where the classical picture of the energy cascade from large scales to smaller scales gives rise to an exact relation.

Anywhere experimental investigation of the scaling laws of turbulence shows that scal-

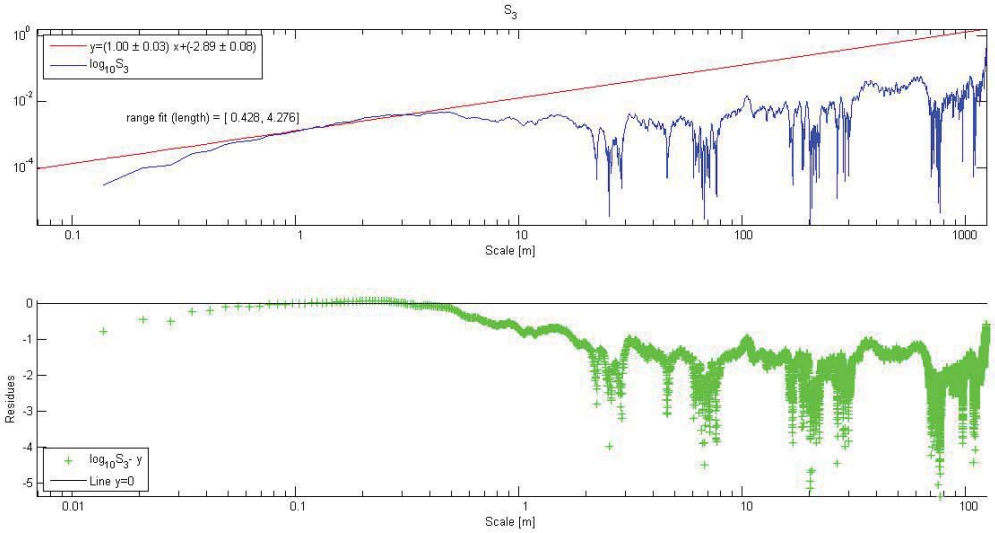

Figure 2.3: *Upper Panel* Linear fit (red) on third-order structure function of velocity increments from sonic anemometer data (blue). It is present a magnitude from ~ 0.4 m to ~ 4 m where Eq. (2.14) is valid (inertial range).*Bottom Panel* Residues between data fit. They are lower in the inertial range.

ing laws are more complicated that expected. In fact, experiments on homogenous and isotropic turbulence established that the n-th order structure function scales as

$$S_p(l) \sim l^{\xi_p/3} \tag{2.15}$$

where $\xi_p = p/3 + \alpha_n$, with α_n a non-linear function of p. This means that the Kolmogorov law is not exact in any case, but there is another phenomenon, not considered yet, that

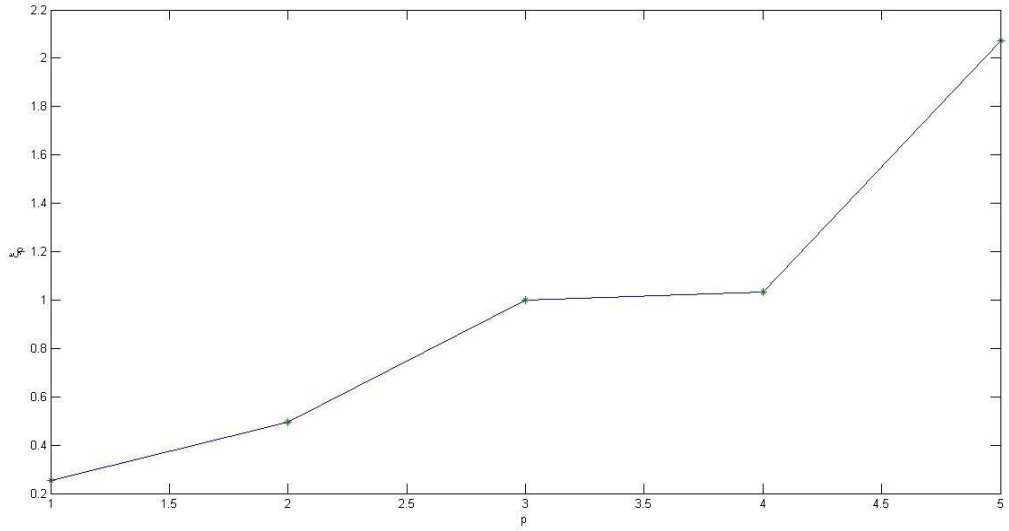

Figure 2.4: Evolution of ξ_p with the order of structure function p. Only in case $p/3 = 3/3 = 1$ the Kolmogorov law is true.

changes the behavior of the simple linear scaling.
This deviation has been attributed to intermittency: there is intermittency in a cascade process, when in the energy transfer from the big scales to the smaller scales there is a non-homogeneous leakage in space and time. This causes, in the fragmentation process, a shift of α_p towards another analytical forms of 2.15 (Frish [31]). It is possible to summarize all these concepts with one word, that is *multifractality*: the same law is repeated on different scales.
In Fig. 2.4 we calculated η against p from data on 16 July 2000, in breeze regime and stable condition. It is possible to note that only in case $p/3 = 3/3 = 1$ the Eq. 2.14 is valid: in the other cases, from $p = 1$ to $p = 5$ there is a increment of η, but is different from the conclusion of Kolmogorov because the presence of intermittency.

2.6 The Yaglom law and the energy dissipation rate

An alternative method for the derivation of the energy cascade rate is to use the Yaglom law, which relates the third order structure function to the mean energy cascade rate and represents one of the most fundamental relations in the theory of turbulence (Yaglom [76];Chandrasekhar [18]; Frish [31]).
Here we report an alternative and more general derivation of the Yaglom's law (Sorriso-Valvo et al. [64], Sorriso-Valvo et al. [65]; Carbone et al. [14])

Through the Yaglom's law, it is possible show that the results of Kolmogorov, based on experiments and similarity considerations on scaling laws in the inertial range, could be

derived from the Navier-Stokes equation.
If we write the Navier-Stokes equation as

$$\partial_t u_i + u_\alpha \partial_\alpha u_i = -\partial_i P + \nu \partial_\alpha^2 u_i \tag{2.16}$$

Using the (2.7) (complete derivation on Bruno and Carbone [13]) obtain that

$$\left\langle \Delta u_l \Delta \left| \mathbf{v}_l \right|^2 \right\rangle = -\frac{4}{3}\epsilon l \tag{2.17}$$

where $\left\langle \Delta u_l \Delta \left| \mathbf{v}_l \right|^2 \right\rangle$ is defined as mixed third-order structure function and ϵ is the energy dissipation rate per mass and time unit. The negative sign is crucial because it reveals the irreversibility of energy cascade. The mixed third-order moment of fluctuations is related to the energy dissipation rate and if it is different from zero than the turbulence must shows some nongaussian features, at least within a certain ranges of scales. This law is important because define the inertial range of turbulence as the range of scales l where the relation (2.17) is exactly verified. This implies that the mixed third-order structure function, unless the second-order one, being unaffected by intermittency ($\alpha_3 = 0$), should be important to investigate the dynamics of turbulence even in situations far from homogeneity and isotropy.
From Eq. 2.17 it is possible calculate, using the third order structure function, the energy dissipation ϵ: a typical example of this last concept is reported in Fig. 2.5. Here it is possible to note a plateau of $F_3/\bar{u} \cdot \tau$, corresponding at inertial range (τ is the time scale): the average of the values plateau c is linked to ϵ. In fact from (2.17) we have that

$$\frac{F_3}{\bar{u} \cdot \tau} = \frac{4}{3}\epsilon \tag{2.18}$$

where

$$F_3 = \left\langle \Delta u_l \Delta \left| \mathbf{v}_l \right|^2 \right\rangle \tag{2.19}$$

and $\bar{u}$ is the mean mainstream component velocity.

2.7 Probability Density

If the fluctuations of a signal follow a scaling law then the phenomenon represented by this signal is self-similar. To argument this sentence lets consider a observable $u(l)$, depending on a scaling variable l, then is invariant with respect to the scaling relation l to λl only if exist a parameter $\mu(\lambda)$ such that $u(l) = \mu(\lambda)u(\lambda l)$. The solution of this last equation is a power law $u(l) = Cl^h$ similar to Eq. 2.15, and then, in the inertial range, the fluctuations of signal are self-similar.
This means that using the probability density function (PDF) of the velocity increments $z_\tau = \Delta u_\tau / \left\langle \Delta u_\tau^2 \right\rangle$ we have:

$$PDF(z_{l\tau}) = PDF(l^h z_\tau) \tag{2.20}$$

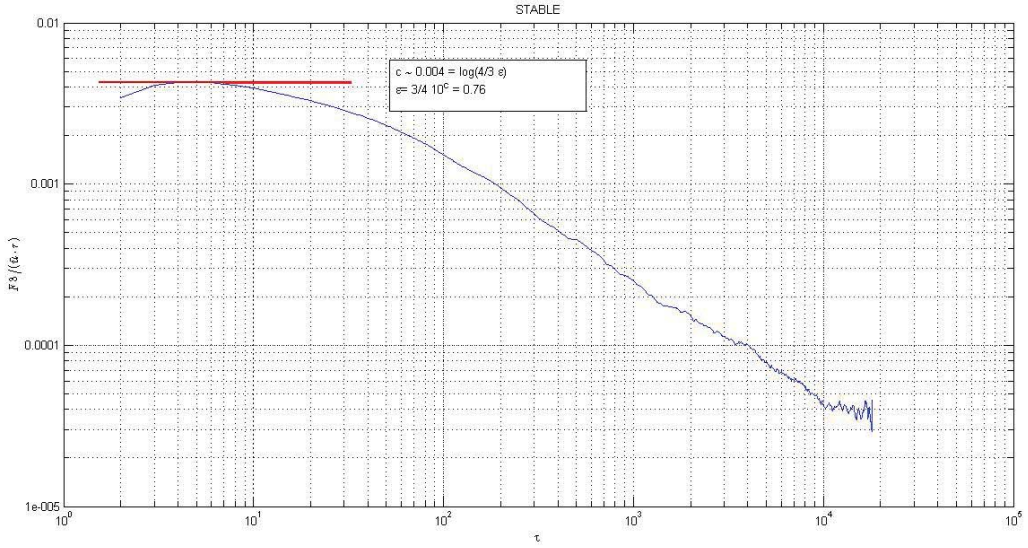

Figure 2.5: Method used to calculate the energy dissipation rate per mass and time unit ϵ for 16 July 2009 in stable condition. The average value of $F_3/\bar{u} \cdot \tau$ plateau is associated at ϵ

An example of PDF calculated with wind speed increments for Lamezia Terme data-set (see next chapter 3) in different atmospheric stability conditions is reported in Fig. 2.6: for small increments ($z_\tau < 1\ m/s$) the PDF is well described by a Gaussian fit; at high increments ($z_\tau > 1\ m/s$) there is a increasingly depart from a Gaussian distribution. It appears evident that at the tails of the distribution the self-similarity is broken. This is caused by the presence of *intermittency* in the transport of turbulent energy, that for high-amplitude fluctuations of a signal have a probability of occurrence grater than a Gaussian distribution: the fluctuations cannot be globally self-similar, as in the Kolmogorov theory, rather a local self-similarity can be invoked, and turbulence can be characterized by a theoretical multifractal framework (Castaing et al. [17], Sorriso-Valvo et al. [64], Bruno and Carbone [13]).

2.8 Kurtosis

Another way to see the variation of PDFs is using the normalized fourth-order moment, named Kurtosis. The fourth central moment is a measure of whether the distribution is tall and skinny or short and squat, compared to the normal distribution of the same variance. Since it is the expectation of a fourth power of the fourth central moment, where defined, is always positive. Kurtosis is defined as

$$K_\tau = \frac{S_4(\tau)}{[S_2(\tau)]^2} \tag{2.21}$$

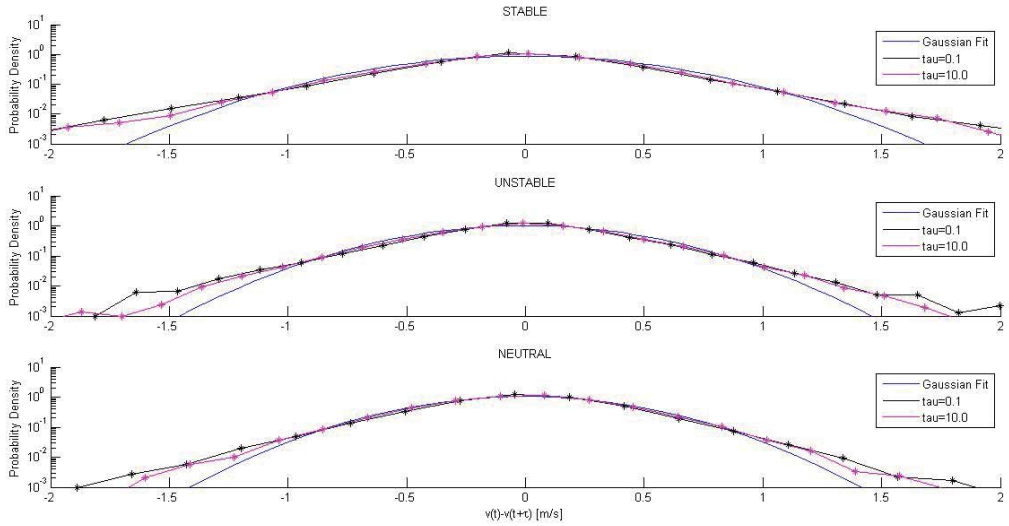

Figure 2.6: Probability density function in the synoptic regime for all stability cases. If the increment are low then the distribution of velocity difference follow the Gaussian distribution; at the tails of distribution for increment than 1 m/s, high-fluctuations have greater probability than Gaussian fit. This is caused by intermittency of energy propagation in all stability cases.

This parameter reveals how the distribution of the signal changes with the scale parameter τ. In the self-similarity situation, for definition, this parameter does not change with τ. In the Fig. 2.7 there is plotted the Kurtosis calculated using structure function of 2.2 (black line): also here the difference between the Gaussian distribution (K_τ on red line) is evident. It worth to note that for $t \longrightarrow \infty$ the structure functions tend to be constant (this behavior was also present in Fig. 2.2).

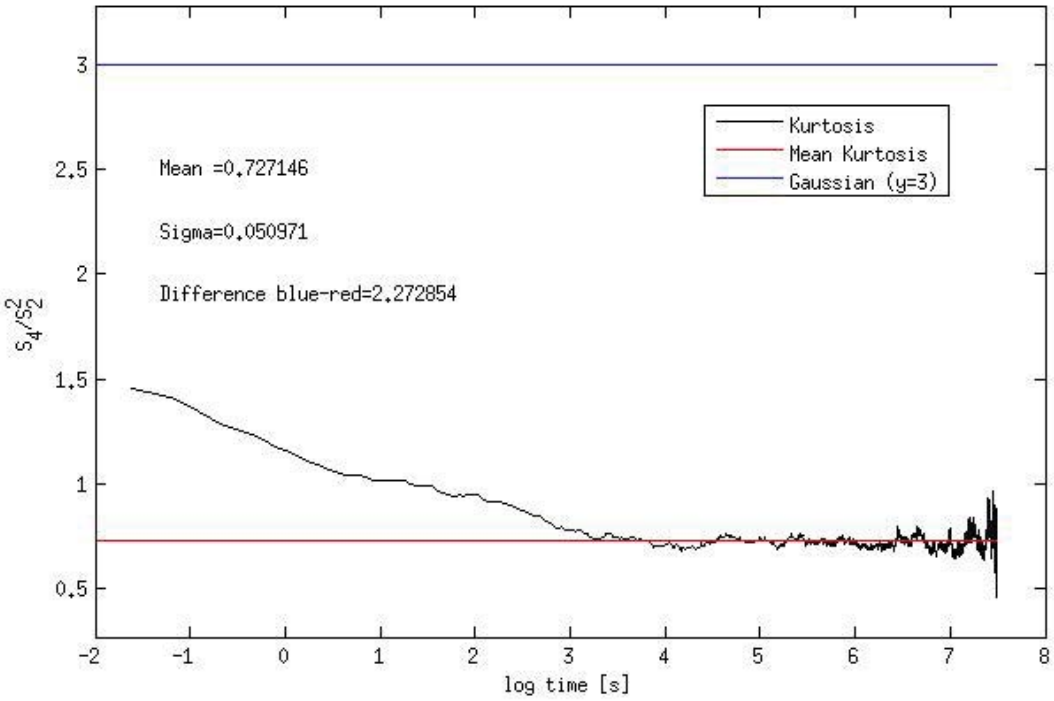

Figure 2.7: Kurtosis (black line) for stable atmospheric condition. Because of the presence of intermittent there is a divergence between this function from Gaussian kurtosis ($K = 3$ red line) at small scales that, then at high scales, is canceled.

Chapter 3

The variation of turbulence with wind regimes and stability conditions

In this chapter we present an application of the concepts of the previous chapter: we used the structure functions to study the variation of behavior of intermittency in different wind regimes and stability classification. The classification of the days in the different regimes has been defined in the work of Sempreviva et al. [61] meanwhile the stability classification inside each day was made using the Obukhov length.

3.1 Experimental Field

For our analysis we have used data from a campaign conducted from July the 2nd to August 6th 2009 at experimental field installed in Lamezia Terme, Catanzaro (Italy). Lamezia Terme's CNR-ISAC station is located in a strategic and isolated position, 600 m from the coastline of the Lamezia Terme airport, in the only valley in Calabria which allows the Tyrrhenian Sea to connect with the Ionian Sea 3.1.
Its complex orography and its long and narrow shape create a complex interaction of breezes which develop perpendicularly the two coasts with the synoptic circulation, that mainly blows from west. In detail, breezes from the sea go mainly W-WSW, while breezes from the earth go mainly E-ENE. Breezes are characterized by seasonal cycles modulated by the temperature gradient between sea and land in addition to the synoptic circulation (more prevalent in determining local circulation in late fall and winter). In particular, while during the summer, there are strong breezes from the sea during the day, in winter there are, at night, intense breezes coming from the land. It was also demonstrated how the breeze system dominated atmospheric circulation in Lamezia Terme and it has an important role to define local climates (Federico et al. [28], Federico et al. [25]).

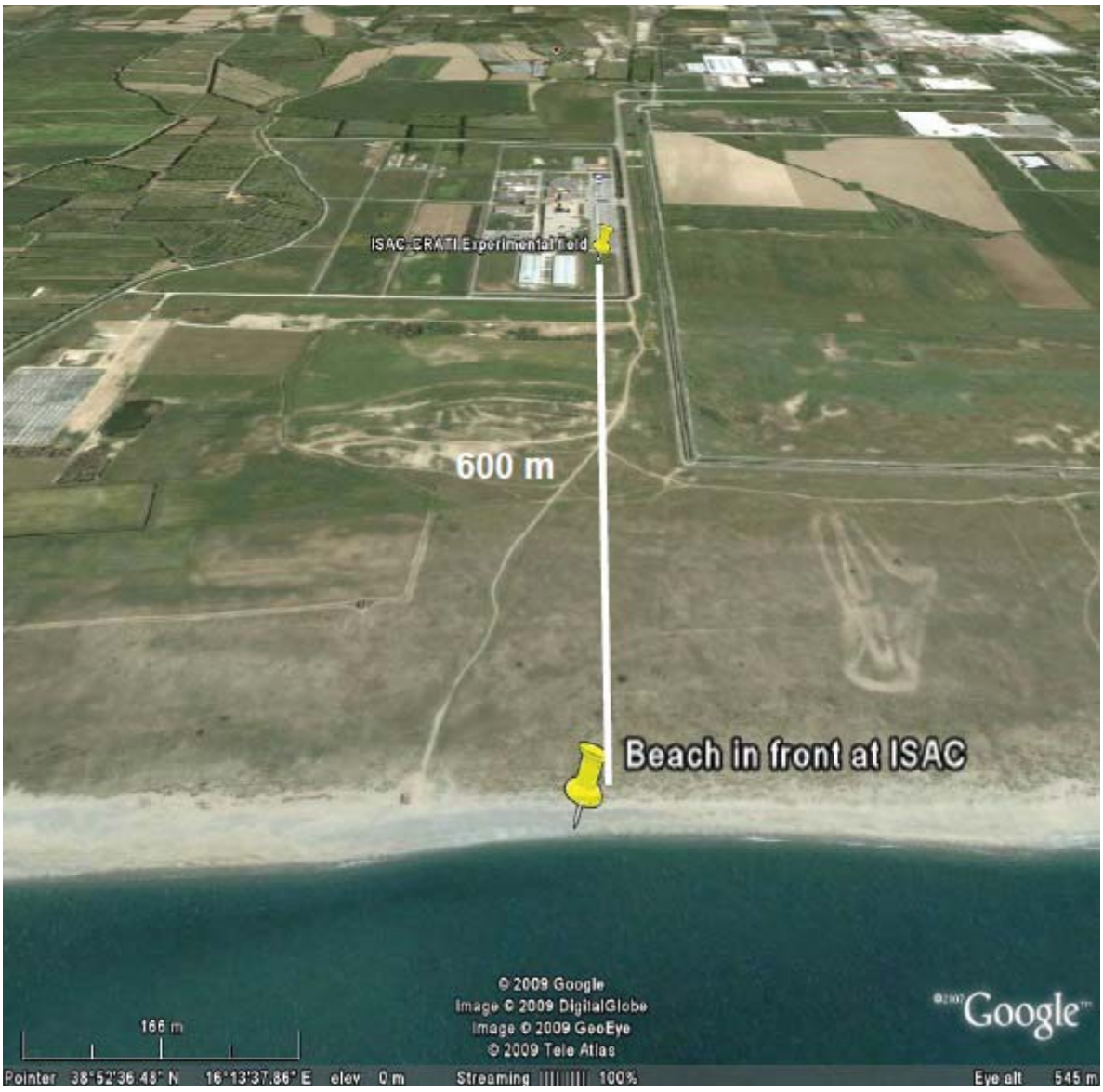

Figure 3.1: Position of ISAC experimental field.

Figure 3.2: 3D Ultrasonic Anemometer. [Credits: www.gillinstrument.com]

3.2 Sonic Anemometer

The velocity data was collected with a sonic anemometer, the 3D Ultrasonic WindMaster^{TM}Pro 3-Axis Anemometer located on the top of 10 meters high mast: in this position we can ignore effects of environmental obstacles in the experimental camp.
Sonic anemometers, first developed in the 1950s, use ultrasonic sound waves to measure wind velocity. It is designed to emit ultrasonic pulses between opposing transducers: in this way the instrument measure the effect of shifting of the air on the signal velocity sound emitted by transducer art [1]. They measure wind speed based on the time of flight of sonic pulses between pairs of transducers. Measurements from pairs of transducers can be combined to yield a measurement of velocity in 1-, 2-, or 3-dimensional flow. The spatial resolution is given by the path length between transducers, which is typically 10 to 20 cm. Sonic anemometers can take measurements with very fine temporal resolution which makes them well suited for turbulence measurements: in our case we have data at 10 Hz. The lack of moving parts makes them appropriate for long term use in exposed automated weather stations and weather buoys where the accuracy and reliability of traditional cup-and-vane anemometers is adversely affected by salty air or large amounts of dust. Their main disadvantage is the distortion of the flow itself by the structure supporting the transducers, which requires a correction based upon wind tunnel measurements to minimize the effect. An international standard for this process, ISO 16622 Meteorology Sonic anemometers-thermometers Acceptance test methods for mean wind measurements is in general circulation. Another disadvantage is lower accuracy due to precipitation: indeed rain drops may vary the speed of sound. Since the speed of sound varies with temperature, and is virtually stable with pressure change, sonic anemometers are also used as thermometers. In addition to these quantities from sonic anemometer it is possible to obtain heat flux, friction velocity, Obukhov length, H_2O and $CO2$ fluxes: all these measures are elaborated thought a data-logger every half-hour.

3.3 Classification: regimes and stability conditions

3.3.1 Data set

For our data we consider to be valid the Taylor's hypothesis: turbulence might be considered to be frozen as it advects past a sensor. Thus, the wind speed could be used to translate turbulence measurements as a function of time to their corresponding measurements in space. It is necessary to keep in mind that turbulence is not really frozen. Taylor's simplification is thus useful for only those cases where the turbulent eddies evolve with a timescale longer than time it takes the eddy to be advected past a sensor (Powell and Elderkin [59]).
Formally if U and V are, respectively, the eastward-moving and the northward-moving Cartesian wind components then the total wind magnitude is $M^2 = U^2 + V^2$: when an eddy of diameter α is advected at mean wind speed M, the time period P for it to pass by stationary sensor is given by $P = \lambda/M$.
For any variable ξ, Taylor's hypothesis states that turbulence is frozen when $d\xi/dt = 0$. But the total derivative is defined by $d\xi/dt = \partial\xi/\partial t + U\partial\xi/\partial x + V\partial\xi/\partial y + W\partial\xi/\partial z$.
Thus, the general form of Taylor's hypothesis is

$$\partial\xi/\partial t = -U\partial\xi/\partial x - V\partial\xi/\partial y - W\partial\xi/\partial z \tag{3.1}$$

This hypothesis can also be stated in terms of a wavenumber, κ, and frequency, f:

$$\kappa = f/M \tag{3.2}$$

where $\kappa = 2\pi/\lambda$, and $f = 2\pi/P$, for wavelength λ and wave period P (Wyngaard and Clifford [75]). The dimensions of κ are radians per unit length, while f has dimensions of radians per unit time.
To satisfy the requirement that the eddy have negligible change as it advects past a sensor, Willis and Deardorff [74] suggest that

$$\sigma_M < 0.5M \tag{3.3}$$

where the standard deviation of wind speed σ_M is a measure of the intensity of turbulence. Thus, Taylor's hypothesis should be satisfactory when the turbulence intensity is small relative to the mean wind speed.

3.3.2 Wind regime

All data sets used gave us a a precise definition of the boundary layer. Using data from many instruments 3.3 it was possible to establish that the wind is in a synoptic regime, by breeze and with an uncompleted sea breeze. In the following sections we present a brief description of this regimes.

Breeze regime

A sea breeze front usually originates along the coastline between land and a large body of water. The thermal properties of water allow incoming radiation to be absorbed in the water column primarily near the surface. This causes the surface temperature of a large bay or ocean to be minimally responsive to diurnal forcing. In direct contrast, most land surface types poorly disperse heat. In particular, urban surfaces have been observed to be heated to surface temperatures well in excess of the surrounding air temperature. Together these processes create a temperature and pressure gradient from which a sea breeze circulation can develop . The sea breeze front is located where advancing cool marine air meets warmer continental air. Typically the continental air mass is drier than the corresponding marine air but this is not always the case. Surface friction and opposing air flow forces some of the advancing sea air to be pushed upward and backward, which then mixes with the drier air. This forms the sea breeze head which lags behind the sea breeze front. More turbulence occurs behind the head and this can result in Kelvin-Helmholtz billows which form along the top of the sea breeze circulation. Surface friction also causes warm air to sink beneath the advancing sea breeze front. This air mixes with the sea breeze after the front passes and can form a series of lobes and clefts (McGowan [49]). The height of the sea breeze is smallest at the front where it can be less than 500 meters thick. In the same study, the researchers showed that the height of the front is inversely proportional to the headwind (Simpsono and Britter [62]). However, throughout the length of the sea breeze, a typical frontal height is about 1 kilometer (Barry and Chorley [11]). The difference between air temperature over land and over the sea surface that is needed to develop a sea breeze can be as little as $1°C$. Generally, offshore wind has the effect of blocking the propagation of a sea breeze. However, this can be overcome if the temperature gradient is sufficient.
A study on the site of our analysis (Federico et al. [28]) shows that breezes dominate the local circulation and play a major role for the local climate. They are modulated by the season, through the sea-land temperature difference and the large-scale flow. The large-scale forcing acts in phase with the diurnal breeze and opposes the nocturnal breeze. In summer, the daytime difference between the land surface temperature and the sea surface temperature) reaches its maximum, while the nigh-time difference has its minimum. This causes a strong, frequent and intense diurnal breeze and a weak nocturnal breeze. In winter and fall the nocturnal difference between the sea and land surface temperature reaches a maximum value, while the diurnal difference is at its minimum value. This causes a strong, frequent and intense nocturnal breeze despite of the large-scale forcing that is usually opposed to local-scale flow.

Synoptic regime

Fig. 3.3 from Sempreviva et al. [61] shows that the days with breeze regime are more than the synoptic regime and also semi-breeze regime. How we said previously the climate of the

Lamezia Terme experimental camp is determinate by the proximity of the sea. Nevertheless there is a presence at day with synoptic regime. These day are characterized by a almost constant direction of wind and by lower temperature respect breeze regime days. In the synoptic regime the circulation of at scales bigger than regional overhangs the local climate and erases the condition for the development of the breeze.

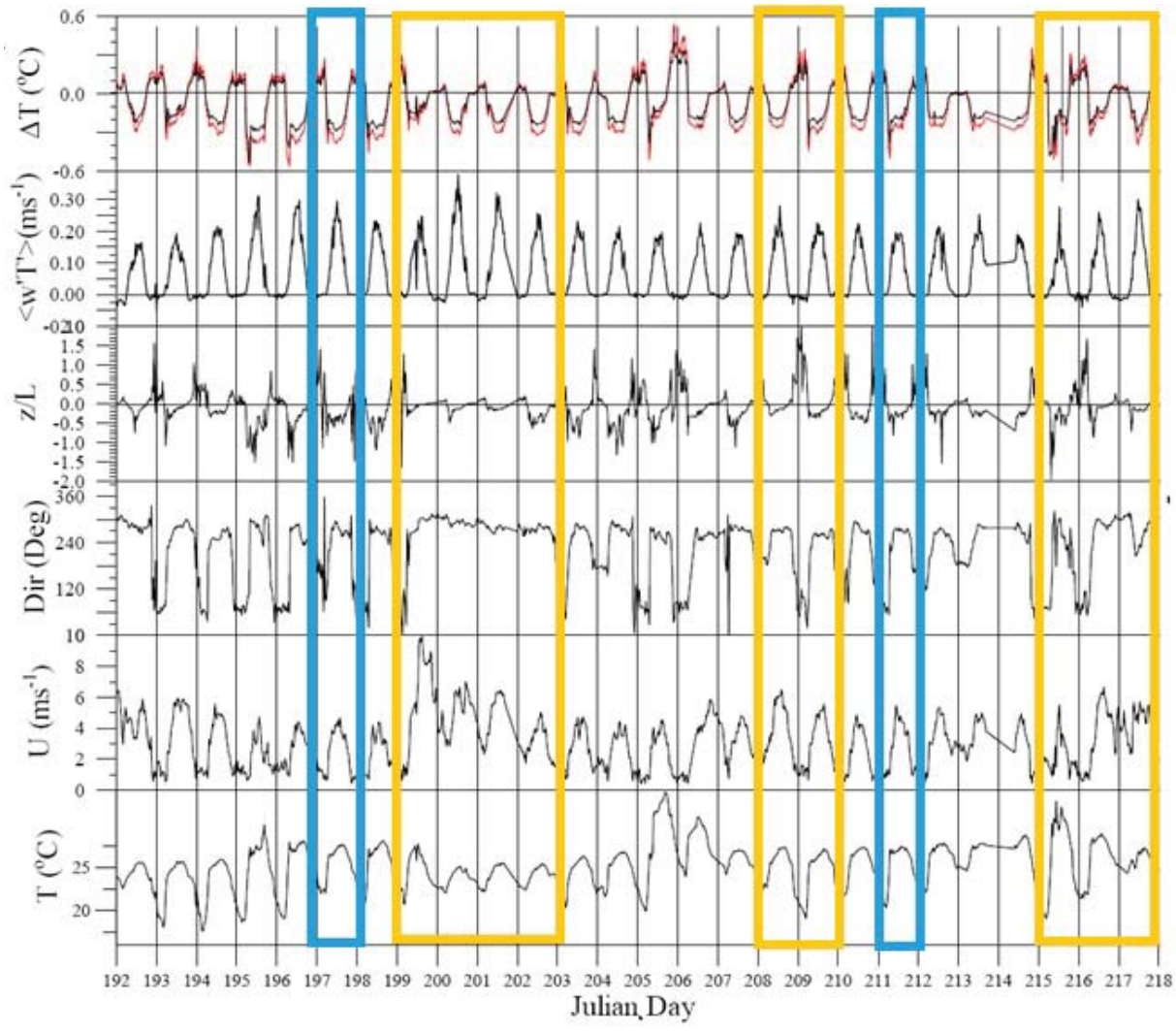

Figure 3.3: Data collected by Lamezia Terme experiment from July,11^{th} to August, 6^{th}. All the day are classified in synoptic (yellow), incomplete sea breeze(blue) and breeze (all the rest) regimes.

Incomplete sea breeze

The regime of incomplete sea breeze is a transition situation between normal local conditions and synoptic perturbations: as it is possible to see in Fig. 3.3 only a portion of the days characterized by incomplete sea breeze shows the usual diurnal variation in direction and temperature. This behavior is explained by the imminent arrival or passing of a large scale perturbation.

3.3.3 Choice of the sample and stability condition

For the our analysis on intermittency, we taken three day with different wind regime and inside each day we have selected three groups of two hours (sampled in four half-hour) for three different stability conditions.
Briefly PBL is unstable when air flows become or remain turbulent. In stable condition flows become or remain laminar. There are many factors that can cause laminar flow to become turbulent, and other factors that tend to stabilize flows. If the net effect for all the destabilizing factors exceeds the net effect of the stabilizing factors, then turbulence will occur.
Static stability is a measure of the capability for buoyant convection and it does not depend on wind motion. Air is statistically unstable when less-dense air (warmer and/or moister) underlies more dense air. The flow respond to this instability by supporting convective circulations such as thermals that allow buoyant air to rise to the top of the unstable layer, thereby stabilizing the fluid. Thermals also need some trigger mechanism to get them started. In the real boundary layer, there are so many triggers (hills, buildings, trees, dark fields, or other perturbations to the mean flow) that cause a formation of mechanical convection, decoupled by intrinsic atmosphere stability.
To simplify the problem, investigator have historically paired one destabilizing factor with one stabilizing factor, and expressed these factors as a dimensionless ratios. In this study we used two factor to express the balance between stability and instability: the z/L and the turbulence intensity (TI).

3.3.4 The Obukhov length and the z/L ratio

The parameter z/L is the ratio between the height from the ground z (the sonic anemometer used in this study is $z = 10$m) and the Obukhov length L defined as:

$$L = \frac{-\overline{\theta}_v u_*^3}{kg(\overline{w'\theta'_{vs}})} \tag{3.4}$$

where $\overline{\theta}_v$ is the virtual potential temperature, u_* is the friction velocity, $\overline{w'\theta'_v}$ is the mean heat flux, g is the gravity acceleration and k is the Von Korman constant (= 0.4, B. [6]). The Obukhov length depend on the inverse of buoyant factor (the denominator) and on the mechanical production of turbulence (*shear*, the numerator).
The z/L ratio is sometime named stability parameter, even if its absolute value is not

linked to the static stability or a the atmospheric dynamic. Under night stable conditions the friction force dominate and z/L results negative, while under unstable, which usually happens in the middle of day, the buoyancy forces overhang frictional force due to the strong convective motion. Furthermore, during the night the forces are balanced because of the high velocity and the absence of temperature gradient. In these condition the planetary boundary layer is well mixed and we observe a neutral situation for stability. Then, values of $z/L > 0$ define a stable situation,while $z/L < 0$ define an unstable planetary boundary layer. When the amplitude $|z/L| \simeq 0$ the planetary boundary layer is under neutral conditions.

3.3.5 Turbulence intensity

The turbulence intensity is a first order estimation of the turbulence and it is defined as

$$TI = \frac{\sigma_M}{\overline{M}} \tag{3.5}$$

Where σ_M is the standard deviation of wind speed M and $\overline{M}$ is its mean. Near the Earth surface, it is expected that turbulence intensity grow with the mean wind speed; for mechanical turbulence, σ_M is a simple function of M. The Fig. 3.4 show the TI and the z/L for 19, July: it's important to note that TI is never up to 0.5 and then the Taylor hyphotesis is respected (B. [6]).
Using similar analysis for other day, it was possible to choice the data set shown in table (3.1). According to the definition of the stability parameter 3.4, all the regimes have been divided in some ranges, each lasting two hours, sampled in groups of half-hours by the data logger linked to sonic anemometer. In this way we recover four samples for each stability condition, as reported on Table (3.1). At the rate of 10 Hz, this means that, every data set lasting 30 minutes is made by 18000 data points, that is each regime is probed trough $\mathrm{N} = 7.2 \cdot 10^4$ points. This was possible for all the data-set except for neutral condition in semi-breeze regime, where there are not four half hour recorder for that day at these condition. Finally, by investigating the fluctuations of velocity in three directions, we found that the averaged speed intensity is of the same order of the means tram component, as reported in Table 3.1.

3.4 Structure functions in the different wind regimes

In order to obtain a complete overview of the variability of intermittency with the wind regimes, many aspects have been considered.
The third order structure function is only the starting point to define which are scales that respect the Kolmogorov law (Eq. 2.14) or the more general Yaglom law (Eq. 2.17). Probability density functions (PDFs) reveal how the intermittency acts at bigger velocity increments expressed by a bigger deviation of these quantities from the normal distribution. With kurtosis it is possible to confirm the result achieved from PDFs and separating

Table 3.1: Characteristic parameters of wind turbulence in each wind regime and for the three stability conditions investigated are reported. The two last two columns refer to the extension of the inertial range and the energy dissipation rate ϵ estimated from the Yaglom's law.

Stability condition	Time Period [UTC]	$\lvert P \rvert$	$\langle u_{\parallel} \rangle$ Main-stream Component $[m/s]$	$\langle U_{tot} \rangle$ Total Component $[m/s]$	Inertial Range $[m]$	ϵ $(JKg^{-1}s^{-1})$
Semi-breeze regime (16th July)						
Stable	19:30÷20:00 v 23:00÷23:30	$\simeq 0.23$ & $\simeq 0.31$	1.45	1.49	0.173 ÷ 1.211	0.84
Unstable	10:30÷12:30	$\simeq 0.20$	4.00	4.13	0.048 ÷ 0.362	0.77
Neutral	19:00÷20:30 v 22:00÷22:30	$\simeq 0.23$ & $\simeq 0.31$	1.42	1.49	0.124 ÷ 1.180	0.76
Synoptic regime (19th July)						
Stable	00:00÷02:00	$\simeq 0.02$	4.13	4.21	0.047 ÷ 0.332	1.80
Unstable	10:30÷12:30	$\simeq 0.30$	6.22	6.34	0.031 ÷ 0.252	2.37
Neutral	22:00÷00:00	$\simeq 0.02$	4.80	4.88	0.040 ÷ 0.340	1.83
Breeze regime (25th July)						
Stable	00:00÷02:00	$\simeq 0.30$	0.81	0.85	0.140 ÷ 1.403	1.80
Unstable	10:30÷12:30	$\simeq 0.23$	3.60	3.72	0.043 ÷ 0.430	2.37
Neutral	19:00÷21:00	$\simeq 0.17$	5.80	5.76	0.082 ÷ 0.824	0.99

scales of turbulence.
All this investigation tools are used in incomplete sea breeze, synoptic and sea breeze regimes to underline that common characteristics and analyze the differences from a turbulent point of view.

3.4.1 Probability density functions

PDFs in each wind regimes are reported in Fig. 3.5: in all cases there is a deviation of speed increments from the Gaussian density function. From sunrise to sunset there is a strong input of energy from sun that causes convective motion (unstable period) and then a growth of the velocity differences: during the energy cascade the energy dissipation is higher than the other periods and then it appears stronger deviations of PDfs from Gaussian behavior. This behavior is more evident for the middle panel of Fig.s 3.5b and 3.5c (please compare them with values of energy dissipation rate of 3.1. During synoptic regime (Fig. 3.5b) energy are constantly released from large scale perturbation and the energy dissipation rates are consequently higher for all day long (Fig. 3.6). Instead, in the incomplete sea breeze regime (3.5a) there is not a prevalence of a tendency respect the other and for this both the deviation of velocity increments (Fig. 3.5a) that ϵ's are constant during the three different stability conditions.

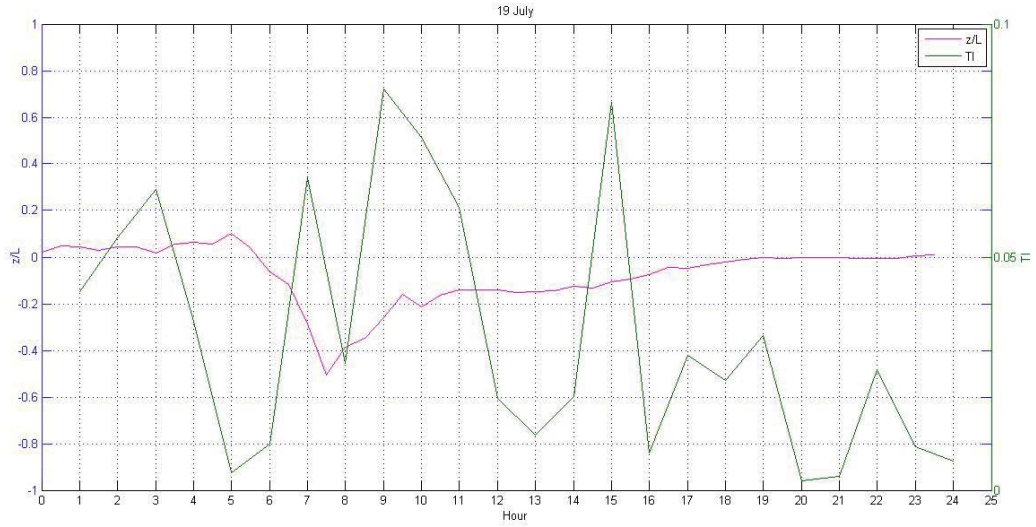

Figure 3.4: The z/L ratio and the turbulent intensity TI for the 19 July. It's worth to note that TI is never up to 0.5 and, then, the Taylor hypothesis is respected.

3.4.2 Kurtosis

As shown in the 2.8 kurtosis is the normalized fourth-order moment of structure functions (2.7) and it is a tool like the probability density function used to quantify intermittency: in the Fig.s 3.7 there is a comparison among kurtosis calculated in the different wind regimes versus temporal scales. For little scale until 15 minutes (10^3 seconds) there is a strong deviation for all kurtosis from Gaussian distribution ($y = 3$): these difference are due at the deviation of the speed increments from the Kolmogorov law (2.14).
There is a little discordance on 3.7a that could be caused by lower number of data available for the regime of incomplete sea breeze (3.1).

3.4.3 Third-order structure functions

As previously mentioned in the previous chapter, the third order structure functions F_3 (2.19) can reveal the range where the Kolmogorov power law for the velocity increment is respected and then give us a starting point to characterize the intermittency in the propagation of energy from large to small scales.
In this section is shown a comparison of the behavior of F_3 (Fig. 2.19) in different wind regimes, also taking account of the variation of atmospheric stability (Fig. 3.8).
The inertial range are shown in black boxes. Inside each wind regime there is a clear tendency: the inertial ranges shift to higher scales as stability increase, because the lower frequencies are more strongly damped by the buoyancy forces. Only the neutral case in synoptic regime show a different behavior. This exception could be cause by the uniformity

of energy input in this regime during all day.
This result is the same of Kaimal et al. [42] (please note spectra in Fig. 3.9) with the difference that in our work this tendency was obtained utilizing structure functions F_3: as said in Chap. 2 the existence of inertial range for F_3's functions confirm the validity of Yaglom law (Eq. 2.17) that is a consequence of Navier-Stokes equations.

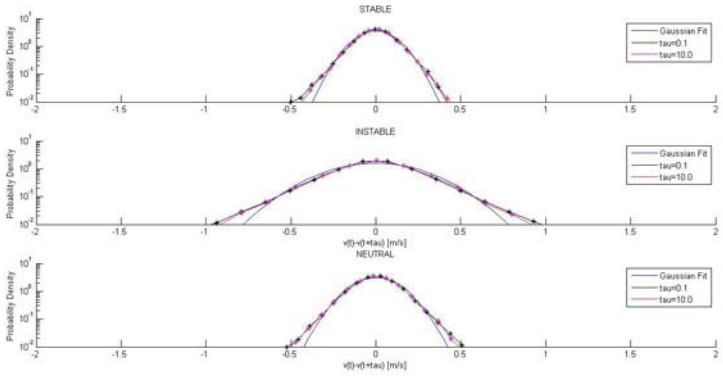

(a) Incomplete breeze

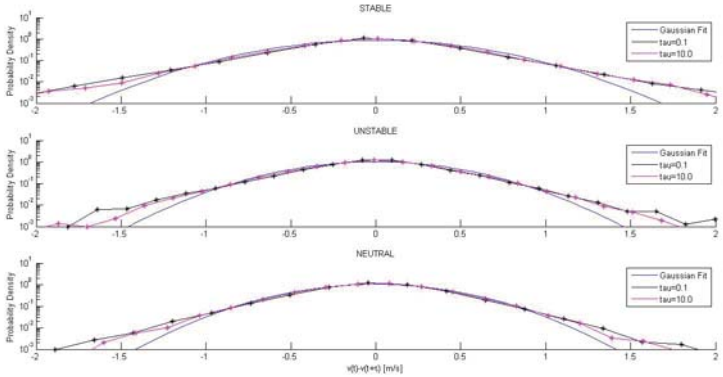

(b) Synoptic

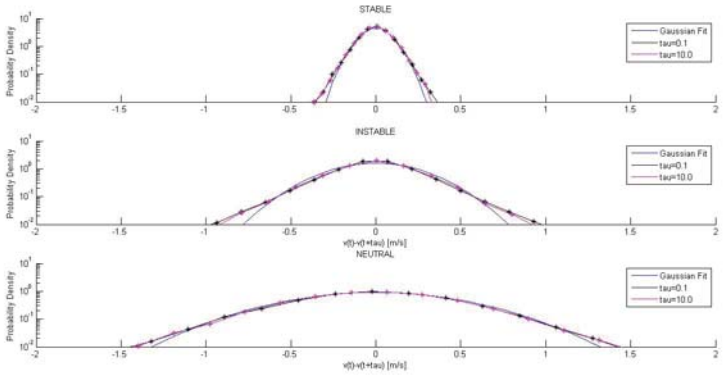

(c) Sea breeze

Figure 3.5: Comparison of probability density functions for the three different wind regime: Incomplete sea breeze (a), synoptic (b) and sea breeze (c). In each panel all the stability cases recorded are shown.

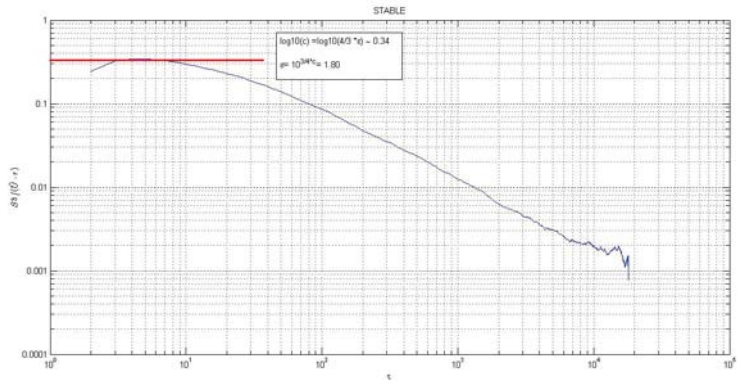

(a) Stable

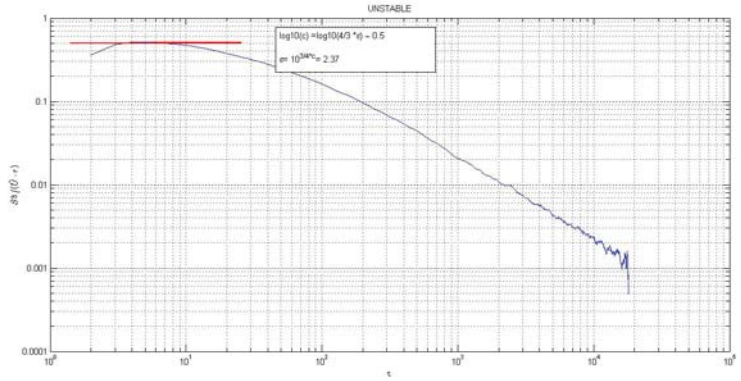

(b) Unstable

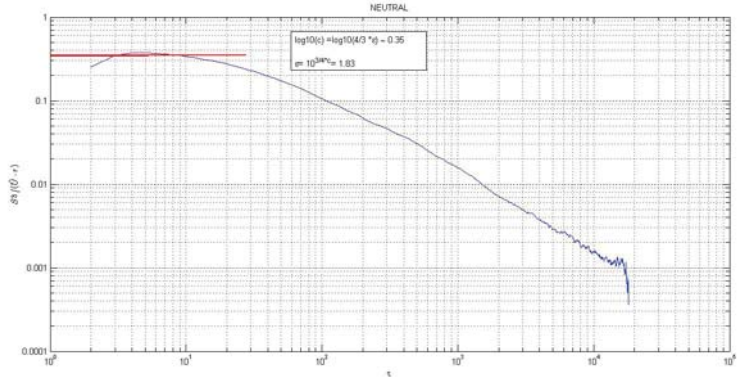

(c) Neutral

Figure 3.6: Energy dissipation rate in the synoptic day (19th July) for the three stability conditions: stable (a), unstable(b), neutral(c).

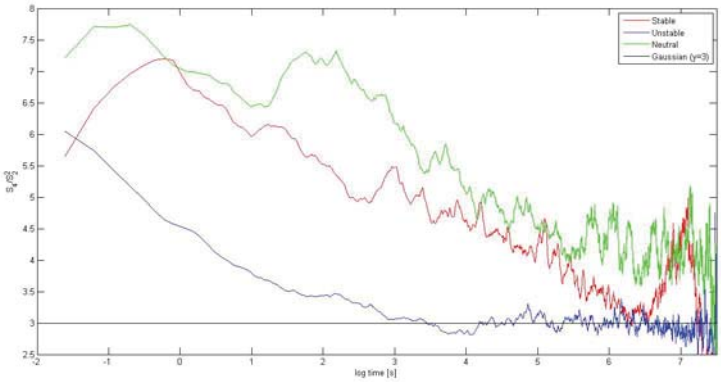

(a) Incomplete breeze

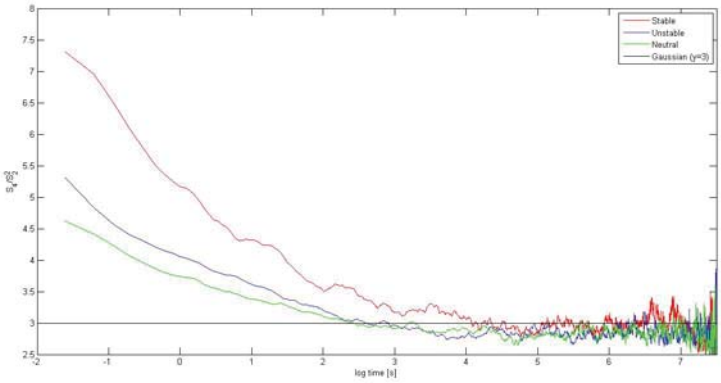

(b) Synoptic

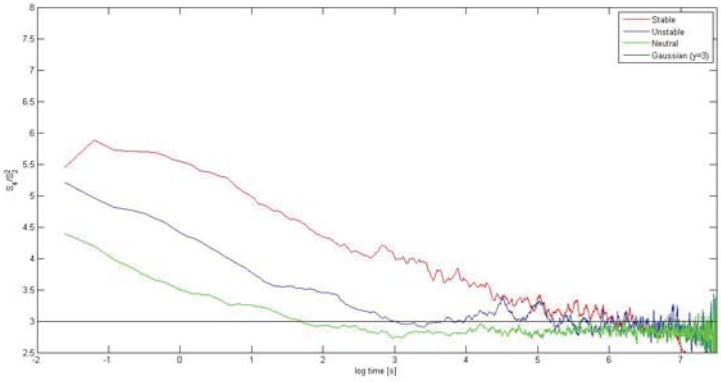

(c) Sea breeze

Figure 3.7: Comparison of kurtosis for the three different wind regime: Incomplete sea breeze (a), synoptic (b) and sea breeze (c). In each panel all the stability cases recorded are shown.

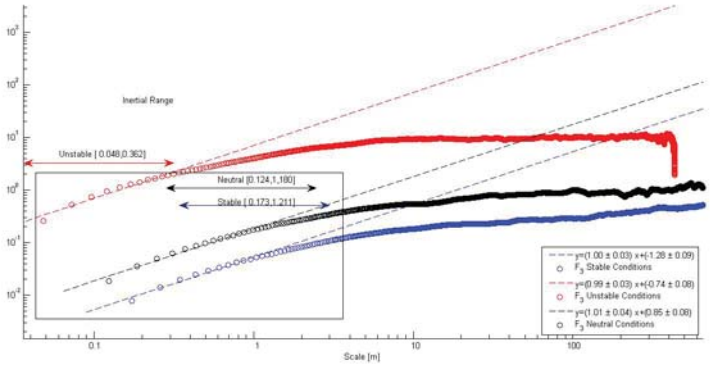

(a) Incomplete breeze

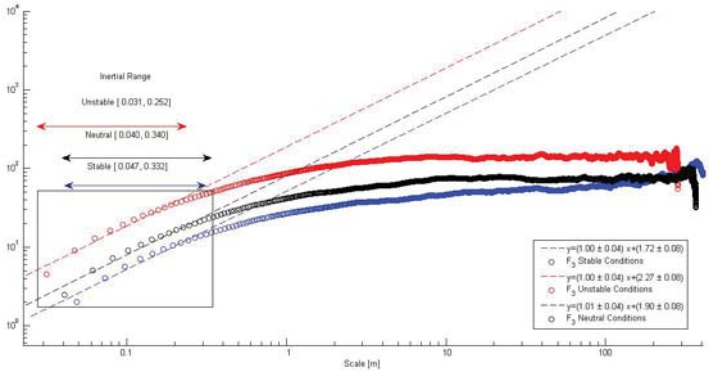

(b) Synoptic

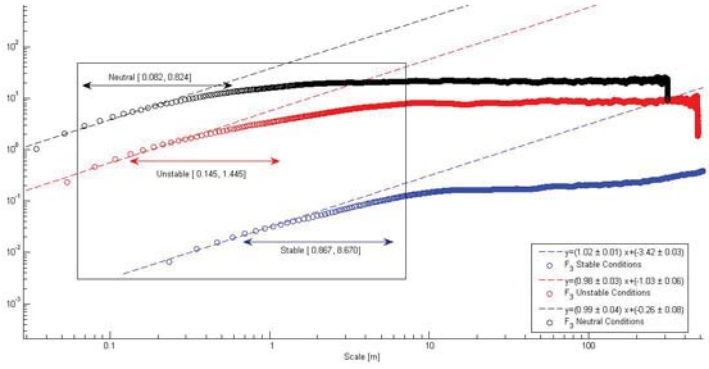

(c) Sea breeze

Figure 3.8: Comparison of all F_3 functions for the three different wind regime: Incomplete sea breeze (a), synoptic (b) and sea breeze (c). In the black boxes inertial ranges for F_3 functions are shown.

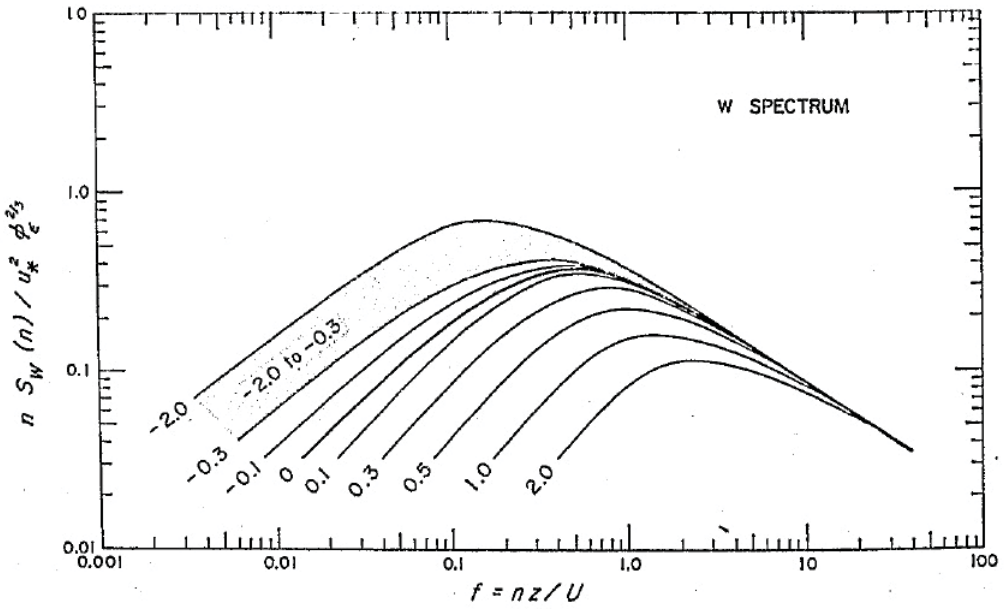

ıre 4. Generalized w spectrum for z/L values ranging from $+2{\cdot}0$ to $-2{\cdot}0$. Stippling indicates absence of any well defined trend with z/L.

Figure 3.9: Generalized u spectrum for z/L values ranging from +2.0 (Stable condition) to −2.0 (Unstable condition). Line $z/L = 0$ is the neutral condition. (Figure from Kaimal et al. [42])

Chapter 4

Wind velocity and turbulence profiles from empiric laws

The following methodologies are based on semi-empiric law obtained from measured data and their iterative correlation: these laws have the goal to simulate the wind behavior at heights until 150 meters from sea level, considering all air stability conditions.
The developed models are useful for the characterization of the vertical profiles of speed and atmospheric turbulence starting from the smallest possible number of meteorological parameters measured near the ground. The physical-mathematical model provides at the lack of meteorological data set, that, in some cases, not are available for the period or the site of interest: in particular it estimates the stability category through Obukhov length (Eq. 3.4) Carruthers et al. [15], turbulence parameters and wind profiles until 150 meters. The simulated wind data were compared with those measured by the Wind Lidar Zephir, in continuous acquisition by July 2013 at the CNR-ISAC Lamezia Terme Institute: the wind Lidar measures a series of meteorological parameters on the profiles of the velocity and direction of the wind at various heights, up to a maximum of 300 m.
These programs do not have the disadvantage of the flow models and the meteorological require huge computing resources and then provide consistent and reliable results: anyway all the outputs obtain from these models are affected by error increasing with the diminution of the parameters available to test the semi-empiric laws, from the atmospheric stability and also by the presence of big obstacles and orographic particular conformations.

4.1 Data sets

Heterogeneous data set are collected to test all the atmospheric parameters. The heterogeneity of the available data and verification of semi-empirical models on the three sets of data available provide a comprehensive comparison and an estimate of the forecast error for all simulated data. This approach permit to calculate trends and profile of wind and turbulence with a good approximation for each levels.

For the developed models, input data at each time t are reported in Table 4.1

Table 4.1: Input parameters for the developed models.

Parameter	Description
T1	Temperature at first level
T2	Temperature at second level
WS	Wind velocity at second level
UR	Relative humidity at first level
z_0	Roughness height of the site

Three data sets are considered:

- Data collected from experimental campaign of 2009 at Lamezia Terme. The period considered is from 00:00 of 11/07/2009 until 23:30 of 06/08/2009 (31 days): all data have temporal frequency of half hour.
- Sounding on Pratica di Mare (LIRE) near Ciampino (ROMA): these data are free and available on website of Wyoming University of USA at the address $http : weather.uwyo.edu$. The period considered is from 1st January 2002 until 31th December 2002, collected each 6 hours.
- Wind profiles measured by Wind Lidar and meteorological date collected by meteo-stations placed in ISAC-CNR UOS of Lamezia Terme from June 2014.

4.1.1 Lamezia Terme experimental campaign

In this database it was possible characterize synoptic wind and sea-breeze regimes. Furthermore the presence of mountains on est side (please compare Fig. 3.1) causes an interaction between sea and land breeze. (For further information please refer to section 3.1).
All instrumentation available during the campaign is reported in Fig. 4.1. Respectively frequencies are associated at each instrument. Quantities are collected from three level, i.e. 2 meters, 5 meters and 10 meters, and they are shown on 4.2.
Obukhov length L_{MO}, friction velocity $u*$, heat flux h_{flux} and wind dispersion are been calculated with the model and verified with data from anemometer sonic; this last instrument was placed at 10 m from the ground and it has a frequency of 10 Hz.

4.1.2 Sounding

Data from sounding are acquired for the station LIRE of Pratica di Mare at Ciampino (12◦ 25′ 48″,41◦ 39′ 0″) for a period of one year from 1st January to 31th December 2002. These data are used principally to test the estimates on humidity at different heights. The soundings are some variables or observations of meteorological parameters collected

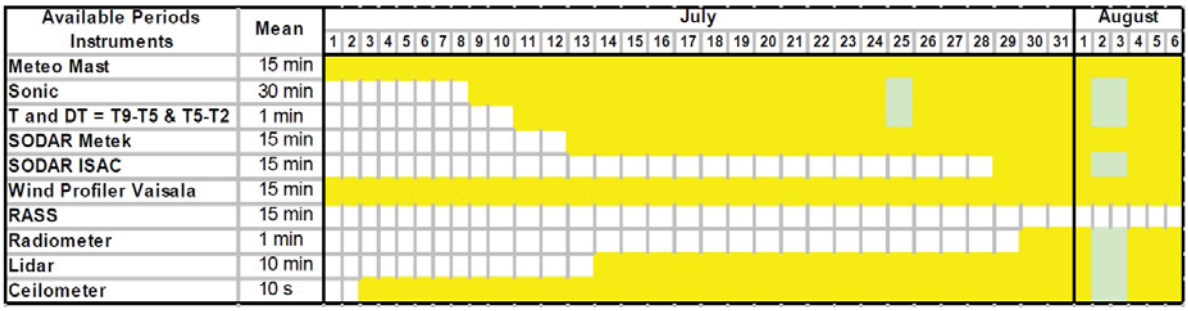

Figure 4.1: Available instruments during the campaign

Table 4.2: Measured parameters

Parameter	Variable
Meteo-station temperature	T_{MS}
Difference of temperature between 5 and 10 m	$T_{diff,1}$
Difference of temperature between 2 and 10 m	$T_{diff,2}$
Difference of temperature between 2 and 10 m	$T_{diff,tot}$
Rate of temporal variation on temperature	DT_{rate}
Mainstream component of sonic anemometer speed	M_{SX}
Longitudinal component of sonic anemometer speed	M_{SY}
Transverse component of sonic anemometer speed	M_{SZ}
Temperature from sonic anemometer	M_{ST}
Friction velocity	u^*
Obukhov length	L_O
Relative humidity	R
Pressure	$Press$
Precipitation	$Prec$
Solar Radiation	Rad

through a measurement instrumentation attached to a weather balloon that is released into the atmosphere. The launches are made with a frequency of 6 hours.

The instrument communicates with the weather center place to the ground using radio signals or a radio. These messages take the name of "TEMP" and are constituted mostly by strings of numbers decipherable manually or with the use of a computer. The balloon is lost after each launch.
The radiosonde mainly analyzes the vertical profile of the atmosphere, i.e. the change of some values such as the temperature and the pressure change as the altitude in the free atmosphere. The release time standard is the so-called *synoptic hours*, in order to compare the data also in the horizontal plane, between stations of different release.

4.1.3 Wind Lidar

Wind Lidar Zephir (Holzworth [38]) measure a series of meteorological parameters about wind intensity and direction profile at several heights. The instrument is in continuous acquisition since July 2013 at CNR-ISAC Lamezia Terme site. The minimum heights is 10

meters and the maximum is 300 meters. Its configuration permits acquisition of 10 values with variable from user steps.
For each heights the Wind Lidar provides all component of wind velocity (horizontal ones and the vertical one), direction an wind shear: this last it is related to the mechanical turbulence.
At each level the instrument acquires 50 sample and then it moves at the next level. Wind profile evolutions are quite comparable to that obtainable from meteorological towers with instruments located at same levels. Wind Lidar has been validated and calibrated up to an altitude of 200 meters above the ground (Carruthers et al. [15]).
The data set available from Wind Lidar is broader and more consistent than those obtained from the campaign of 2009 and to soundings taken account; it also presents a higher sampling frequency. With regard to our studies and characterizations data from July to June 2014 averaged a half hour were been selected. This has allowed us to produce and analyze a classification of the errors of prediction of wind profile as a function of both the seasonal variation of the Pasquill stability classes.

4.2 The semi-empirical laws for the estimation of parameters of turbulence and stability

Every physical quantities are calculated in separate task, except the height of boundary layer that it is iteratively calculate during the day: code separation ensures an inherent ease of use, immediate verifiable observations and prepare for future improvements and also rewrite the individual parts. The design of the model is shown in Fig. 4.2 .

4.2.1 Dew point temperature

Temperature of the dew point T_d is the first physical quantity simulated by the program: an immediate comparison with the sounding observed data was been calculated.
Two types of theories, well known in literature, are used to reproduce the evolution of T_d with height:

- The method of Murphy and Koop (Murphy and Koop [54]), that directly exploits the definition of dew temperature while for the calculation utilizing an empirical expression of the vapor pressure e_w.

- The approximation of Magnus-Tetens (Magnus [46]), which is a simple semi-empirical: for the calculation uses only the humidity and the absolute temperature (quantities available to all heights in the soundings data).

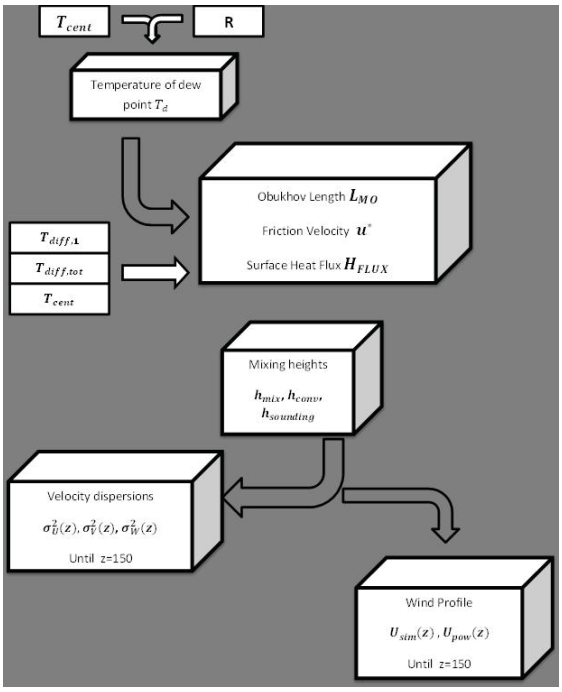

Figure 4.2: Flow diagram of procedures

From the vapor pressure at the dew point temperature (Murphy and Koop, 2005)

By definition, the temperature of the dew point T_d is the temperature at which the air must be cooled to become saturated respect to a planar surface of water.
In other words, T_d is the temperature at which the ratio of air saturation w_s becomes equal to the mixing ratio w. For this the humidity at the temperature T and pressure p is given by:

$$R = 100\frac{w_s(T_d, p)}{w_s(T, p)} \tag{4.1}$$

The water vapor and the dry steam obey the same equation of ideal gases which depends on the vapor pressure of saturation

$$w_s = \frac{\hat{\rho}_{vs}}{\hat{\rho}_d} \sim 0.622\frac{e_w}{p} \tag{4.2}$$

Where $\hat{\rho}_{vs}$ is the partial density of the water vapor required to saturate the air respect to water at the temperature T,$\hat{\rho}_d$ is the partial density of the dry air and p the total pressure. The expression for e_w is empirical and is obtained by Murphy and Koop (2005 Murphy and Koop [54]) test with data from laboratory and several measurement campaigns

$$\begin{aligned}\log e_w = 54.842763 - 6763.22 \cdot T - 4.21 \log T + 0.000367T + \tanh 0.0415 \cdot (218.8) \\ \cdot \left[(53.878 - \frac{1331.22}{T} - 9.44523 \log T + 0.014025 \cdot T\right]\end{aligned} \tag{4.3}$$

With T measured in K and p in Pa. Then through an expression for $\hat{\rho}_{vs}$ and knowing the moisture and the temperature from 4.1 (the pressure cancels out), it is possible to determine the temperature of the dew point.

A direct semi-empirical law

An approximation widely used and proven to standard conditions ($0°C < T_{abs} < 60°C$, $1\% < RH < 100\%$, $0°C < T_d < 50°C$) is the Magnus-Tetens formula(Magnus [46], the formula is known by that name, but his nomination historically more accurate to assign at August, Roche and Magnus). This expression is an empirical law, which contains a formulation of the vapor pressure and latent heat of the air and water (quantities that depend only on the absolute temperature) and is as follows

$$T_d = \frac{b - \alpha}{a - \alpha} \tag{4.4}$$

with

$$\alpha = \frac{aT_abs}{b + T_{abs} + \log R} \tag{4.5}$$

Where $a = 17,27$ and $b = 237.7K$.
From comparisons calculated for a period of one year on data from soundings emerges that the method of Magnus-Tetens presents the RMSE smaller than that of Murphy and Koop. It follows that the method of Magnus-Tetens is always used to calculate T_d. An evident example of this conclusion it is Fig. 4.3: the curve red calculate using Magnus-Tetens method and T_abs is, in every levels, more similar at sounding data (violet curve) respect the dew temperature calculate with Magnus-Tetens method and virtual temperature T_v (black curve) and the Murphy and Koop method and T_{abs} (cyan curve). A quantitative difference between two method is shown in Tab. 4.3

Table 4.3: Errors in the two methods of calculating the T_d for the months of the year acquired.

Month	RMS Magnus-Tetens	RMSE Murphy and Koop
January2002	0.005	3.050
February 2002	0.004	3.551
March 2002	0.007	7.200
April 2002	0.005	6.602
May 2002	0.005	5.579
June 2002	0.007	9.840
July 2002	0.006	7.153
August 2002	0.004	5.369
September 2002	0.005	4.934
October 2002	0.007	6.624
November 2002	0.004	4.196
December 2002	0.003	2.383

To calculate the T_d with data of Lamezia Terme campaign the temperature measured by the meteo-stations T_centr is used because of its lower standard deviation respect the

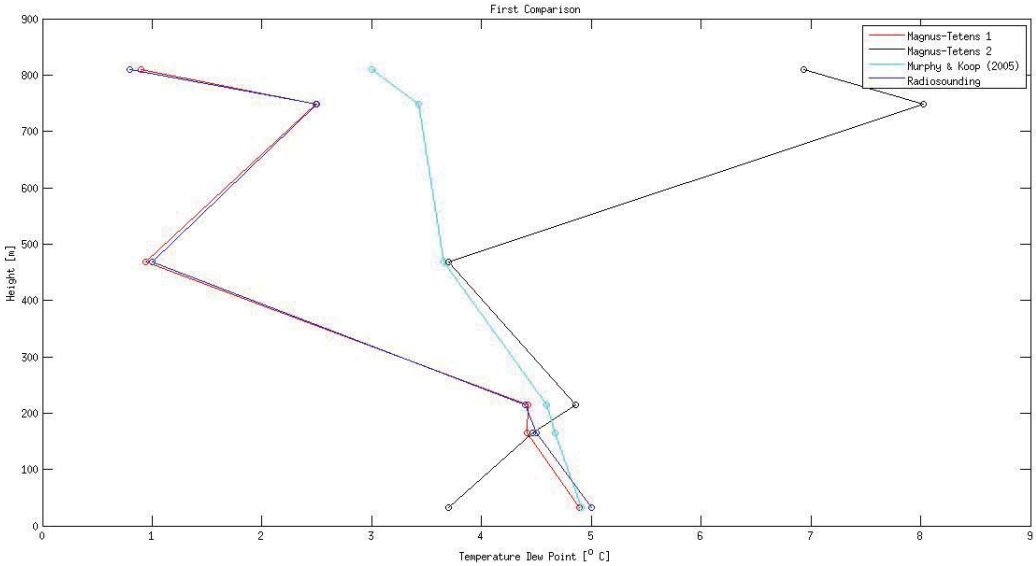

Figure 4.3: Comparison of profiles at high altitude the temperature of the dew point. The violet curve are sounding data for 15 November 200, the red curve is calculate using Magnus Tetens and absolute temperature T_{abs}, the black curve is obtained using Magnus Tetens and virtual temperature T_v, and the cyan curve with Murphy and Koop method and absolute temperature T_{abs}.

thermocouple temperature measured at the ground T_{abs} ($\sigma_{centr} = 2.16 \circ C$ respect $\sigma_{abs} = 2.39 \circ C$).

4.2.2 Scale parameters

Scaling parameters are data input for all analytical models based on stability classification, and for three-dimensional Lagrangian and Eulerian models. For scaling parameters we mean here the friction velocity u^*, the Obukhov length L_O, and the surface heat flux H_{FLUX}; other scaling parameters (like the scale temperature J^*, and the scale vertical velocity w^*, may be obtained from these three and the mixing height h.
The methods for estimating the scaling parameters presently included are described in Val Ulden and Holslag [70]. This "profile method" is based on the solution, by iteration, of three equations:

$$L_O = \frac{u^* T}{kgJ^*} \tag{4.6}$$

$$u^* = \frac{kU(z)}{\ln(z_1)/z_0) - aM(z1/L) + aM(z_0/L)} \tag{4.7}$$

$$J^* = \frac{k\left[J(z_2) - J(z_1)\right]}{\ln(z_2/z_1) - aH(z_2/L) + aH(z_1/L)} \tag{4.8}$$

where k is Von Karman constant ($k \sim 0.41$), a dimensionless constant describing the logarithmic velocity profile of a turbulent fluid flow near a boundary with a no-slip condition; g is the gravitational constant, aM and aH are stability functions, $z21$, z_1 are arbitrary heights in the surface layer and z_0 is the roughness length. This method require a single wind speed at z_1 and two temperature at z_1 and z_0 near the surface. H_{FLUX} is obtained from J^* through:

$$H_{FLUX} = -\rho C_p u^* J^* \tag{4.9}$$

with ρ air density and C_p air specific heat. In Fig. 4.4 is shown a comparison between observation and model data. There are some out-layers, probably missed by instrument, but despite this, correlation factor is high ($cc \sim 0.73$).
Once computed u^* using the aforementioned methods it was possible to compare it with that obtained from sonic anemometers of Lamezia Terme 2009 campaign: as result there is a strong correlation between observed and calculated values of about 94%. (Fig. 4.5. For this comparison z_0 was set equal to 0.1 m, that is the typical height of a grassland.

As regards the comparison between the length of Monin-Obukhov observed and calculated, the correlation is very dependent on the range that is considered (Fig. 4.6). If we consider the entire range (-500, 500), the correlation coefficient is low (about 0:53): indeed, a real comparison could be made only in the significant range in between -100 (very unstable) to 100 (very stable) (B. [6]) in which the correlation coefficient increases to about 0.80 (for a better understanding, see the chapter on classes of Pasquill). A decrease of the

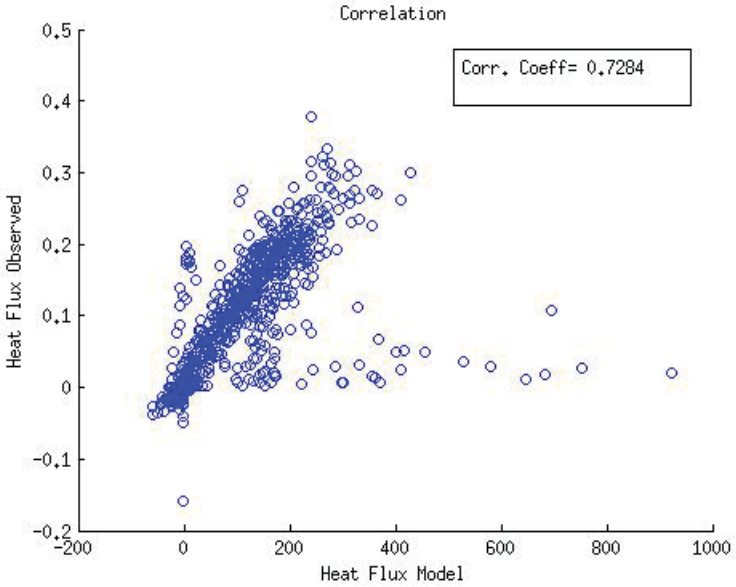

Figure 4.4: Comparison between observed and model H_{FLUX}'s. Also considering probably out-layers, there is a good agreement between obeservations and model.

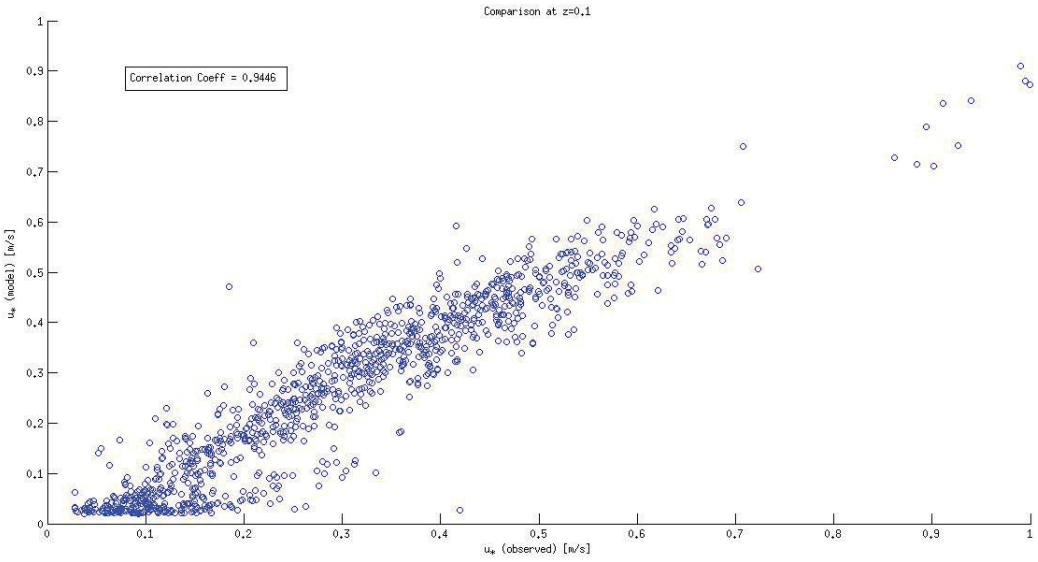

Figure 4.5: Comparison between observed and model u^*'s.

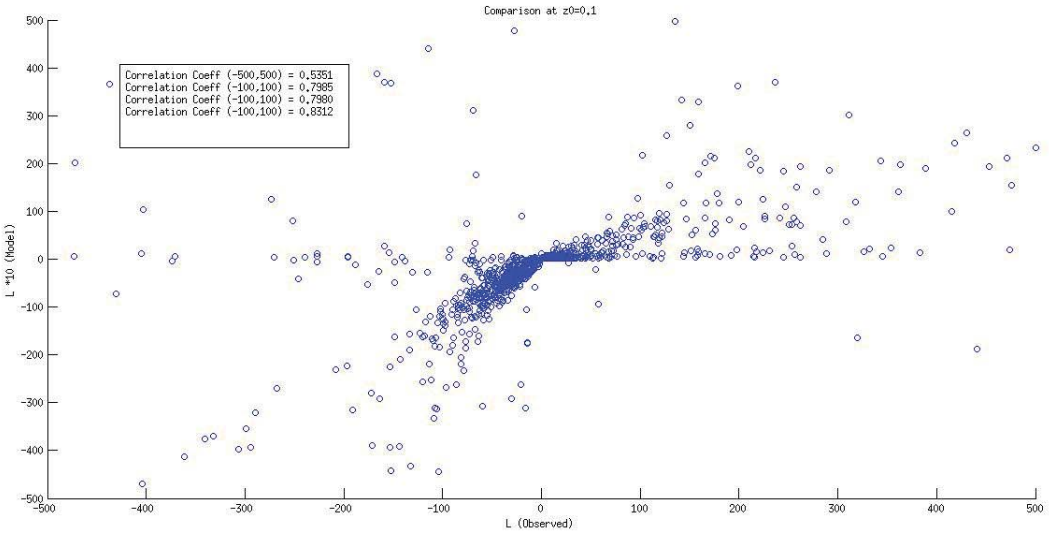

Figure 4.6: Comparison between observed and model L_O's. At significant range $[-100, 100]$ the correlation coefficient is equal to 0.80.

range does not involve significant increases in the correlation coefficient.

4.2.3 Mixing and convective lengths

Mixing heights h is a crucial parameters for any kind of dispersion model non limited to very short distances from release point. In neutral and stable situation ($L > 0$), h is parametrized using surface parameters (Niewstadt [56]):

$$h = \frac{c_1 u^*}{f \cdot (1 + c_3 h / L_O} \tag{4.10}$$

where f is Coriolis parameter ($f = 2\Omega \sin \phi$, with Ω angular velocity of Earth and ϕ latitude of the site), $c_1 = 0.3$ and $c_3 = c_1/c_2$ with $c_2 = 0.7$. This formulation approaches asymptotically the neutral estimate $h_n = c_1 u * /f$ (Deardoff [22]), and approaches $h_n = 1/2 c_2 (u * L_O)/f$ (Zilitinkevich et al. [78]) in stable conditions.
In the unstable boundary layer ($L < 0$) two alternative methods for the estimate of the mixing depth can be used, depending on the primary input data available. If only surface data are available, a "slab" model is adopted, based on the integration of the following rate equation (Batchvarova and Gryning [12]):

$$\frac{h^2}{1.2h - 2L_O} + \frac{8u^* 2T}{gg 1.2h - L_O} \frac{dh}{dt} = \frac{-H}{g\rho C_P} \tag{4.11}$$

gg is the potential temperature gradient above the mixed layer and it is set to $0.005°C/m$. If the vertical profiles of temperature and humidity (or dew point temperature) are avail-

able, the "dry parcel intersection method" (Holzworth [38]) is adopted. The mixing height is obtained by lifting a parcel with virtual potential temperature J'_v up to the intersection with the virtual potential temperature profile. J'_v is given by the virtual potential temperature near the surface, J_{vs}, plus a scaled virtual temperature excess (Troen and Mahrt [69], Holtslag et al. [37]):

$$J'_v = J_{vs} + 10 \cdot \frac{H}{\rho C_p w^*} \tag{4.12}$$

this equation is resolved iteratively since w^* is a function of h.

4.2.4 Wind profile

The directional wind shear is an important aspect to model wind profile at high levels. As shown in Fig. 4.7, the wind speed usually varies approximately logarithmically with height in the surface layer. Frictional drag causes the wind speed to become zero close to the ground, while the pressure gradient forces cause the wind to increase with height. In neutral situations, occurring usually during the night (blu in Fig. 4.7) a logarithmic curve well fit the behavior of wind speed with the height. For non-neutral situations, there is no equilibrium between buoyancy parameter and surface heat flux and wind profile deviates slightly from logarithmic. If buoyancy is stronger than heat flux, there are stable conditions (for example the violet curve on second panel of Fig. 4.7) and wind profile is concave downward logarithmic plot: reversal, if heat flux is stronger than buoyancy (for example the cyan curve during transition period on fourth panel) the boundary layers are unstable and the trend of wind speed with heights is concave upward on a logarithmic plot.

To test the influence of these tendency on deviation by logarithmic behavior, two approaches for the estimate of vertical profile are included in the our model. The first is based on Monin-Obukhov similarity theory for the surface layer Monin and Obuhov [52]:

$$U(z) = U(z_1))\frac{\ln(z/z_0) - aM(z/L)}{z_1/z_0 - aM(z_1/L)} \tag{4.13}$$

where z_1 is the height at which a wind observation is available. Empirical functions aM with an acceptable performance in the range $0 < z < h$ are used (Val Ulden and Holslag [70]). To avoid unreliable values of $U(z)$ for large z, $U(z)$ is set to $U(150)$ for $z > 150$ m. The second method is based on the widely used "power-law" wind profile; the exponent is tabulated as a function of the surface roughness and of the stability category, which must be previously estimated with one of the method described in Irwin [40]. The power law is considered valid up to 150 m; for $z > 150$ m, $U(z) = U(150)$.

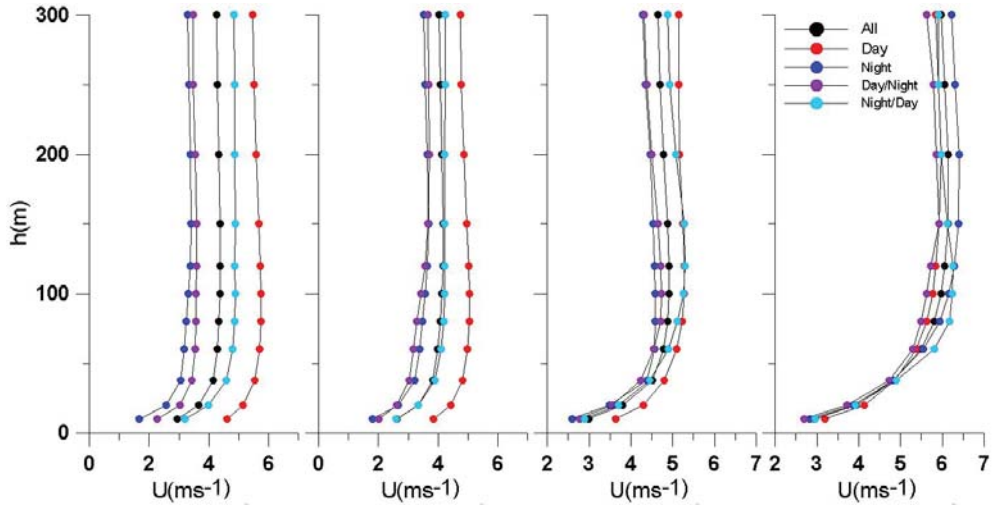

Figure 4.7: Wind profile collected by Wind Lidar at Lamezia Terme CNR-ISAC in different days. The variation of wind speed with height is typically logarithmic in neutral surface layer, but it changes in stable and unstable conditions.

4.2.5 Turbulence

To calculate the parameters of the turbulence (dispersion of the components of the velocity) was used to model atmospheric dispersion Carruthers et al. [15] adoptable to lower altitudes up to mixing of the boundary layer. In convective conditions the speed scale of the mixed layer is defined as

$$(w^*)^3 = \frac{h_m ix (u^*)^2}{k\,|L_O|} \tag{4.14}$$

In this way we can define the velocity dispersion components depending on stability conditions:

- In unstable condition $h_{mix}/L_O < -0.3$)

$$\sigma_u^2 = 0.3w^{(*2)} + 6.25T_{W_N}^2(z)u^{(*2)} \tag{4.15}$$

$$\sigma_v^2 = 0.3w^{(*2)} + 4.0T_{W_N}^2(z)u^{(*2)} \tag{4.16}$$

$$\sigma_w^2 = \left\{0.4T_{W_C}^2(z) + (1.3T_{W_N}(z)u^*/w^*)^2\right\} w^{(*2)} \tag{4.17}$$

where

$$T_{W_C}(z) = 2.1\frac{z}{h_m ix}^{1/3}(1 - 0.8z/h) \tag{4.18}$$

$$T_{W_N}(z) = 1 - 0.8z/h \tag{4.19}$$

- In neutral condition ($-0.3 < h_{mix}/L_O < 1$)

$$\sigma_u^2 = 2.5u^* T_{W_N}(z) \tag{4.20}$$
$$\sigma_v^2 = 2.0u^* T_{W_N}(z) \tag{4.21}$$
$$\sigma_w^2 = 1.3u^* T_{W_N}(z) \tag{4.22}$$

- At the end in stable condition ($h_{mix}/L_O > 1$)

$$\sigma_u^2 = 2.5u^*(1 - \alpha_s z/h_{mix})^(3/4) \tag{4.23}$$
$$\sigma_v^2 = 2.0u^*(1 - \alpha_s z/h_{mix})^(3/4) \tag{4.24}$$
$$\sigma_w^2 = 1.3u^*(1 - \alpha_s z/h_{mix})^(3/4) \tag{4.25}$$

  where $\alpha_s = 0.9$ in ideal conditions or when it is assumed that neither the topography nor the roughness change over time, while it is equal to 0.5 when this does not occur.

4.3 Comparison with data from wind Lidar

Fig. 4.8 shows the trends and values of the mean square error (RMSE) calculated for the whole year available respectively for the method of similarity and power law. Here we see, as expected, the error increases with altitude. Normally this can be caused by two reasons. The natural increase of the uncertainty of the forecast as the share given that the values of the lower altitudes have been parametrized on the basis of existing data sets. The second reason is due to the increase in RMSE, as the sum of the squared differences between observed and calculated, due to the higher value of the measure (wind speed) and its comparison.
Anyway, sometimes and especially during the winter night (stable cases) there are low-level jets that increment the errors (Fig. 4.9): power law method (red line) is not able to follow the velocity trend in stable cases because it is not directly influenced by stability variation. Stability method follows more closely the observed velocity variation with height, but the particular position of valleys and mountains near the institute causes a amplification of wind around 100 m. In the lowest 2 to 10 m, cold air will drain down hill. Wind direction in this layer is determined by local; wind speed is governed by buoyancy, friction, and entrainment. At the bottom of valleys the wind become calm, but higher in stable boundary layer, synoptic and mesoscale forcing become important. The wind speed can increase with height, reaching a maximum near the top of the stable layer, that could be greater than the geostrophic speed of the upper level. This wind jet, than, are not predictable using just 2 levels under 20 m, but it necessary to acquire other data also on the particular terrain shape and its effects on wind velocity (for example using a fluid-dynamic model applied to the terrain).

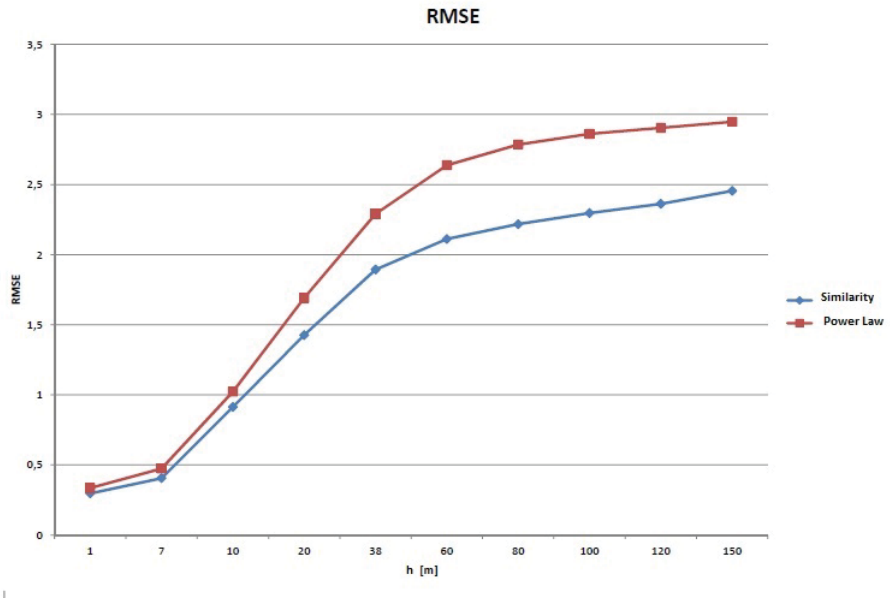

Figure 4.8: Annual RMSE for similarity theory wind speed profile (blu curve) and that for power law (red curve) calculated with data from Wind Lidar.

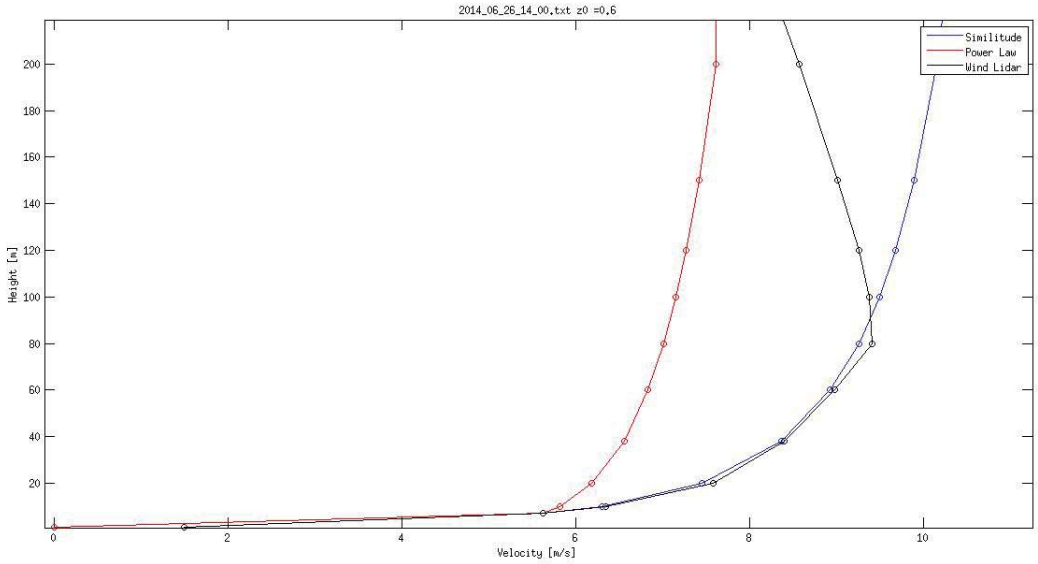

Figure 4.9: Observed wind profiles (black curve), provided by similarity theory (blue curve) and according to the power law (red curve) during not neutral conditions. Probabily the deviation is caused by low-level jet.

4.3.1 Errors

Each semi-empirical law has been verified by experimental data, using a not homogeneous dataset. Anyway, considering the figures 4.3, 4.4, 4.5, 4.6, it is possible to conclude that the parameters all well singularly reproduced. From the error estimation (Seasonal Fig.4.10, 4.11 and considering the angular distribution of wind direction Fig.4.12, 4.13) it is possible to have a overview on the performance of the forecast methodology. For all figures it is clear that similarity method presents errors always smaller respect power curve law in almost the totality of cases: the difference between the two methods is bigger at higher altitudes and it comes close 2 m/s of RMSE.

In Figs.4.10, 4.11 it is shown that the RMSE is higher in winter than in summer: there are differences between the RMSE's on the seasons of a few tenths to a maximum of 1 m/s, depending on the altitude and on methodology used.
This may be caused by the synoptic conditions prevailing in the winter than the local breeze conditions. Spring and autumn are intermediate conditions that depend on the number of days in which there is the prevalence of conditions or synoptic breeze.
On areas of prevalence of the wind (west to areas with $225° < \theta < 255°$ and $255° < \theta < 285°$), corresponding to purely local conditions (sea breeze) RMSE's are always smaller than in other cases.
Finally it was been analyzed the evolution of RMSE with height in different stability conditions in the two methods followed (Fig. 4.14): here, it is interesting to note that the similarity better reproduce observed data respect the power law method in stable and neutral cases, but the two methods give similar errors in the unstable case.
This result could be explained a not correct estimate of vertical heat flux, connected with a not modeled turbulent effect on velocity variation.

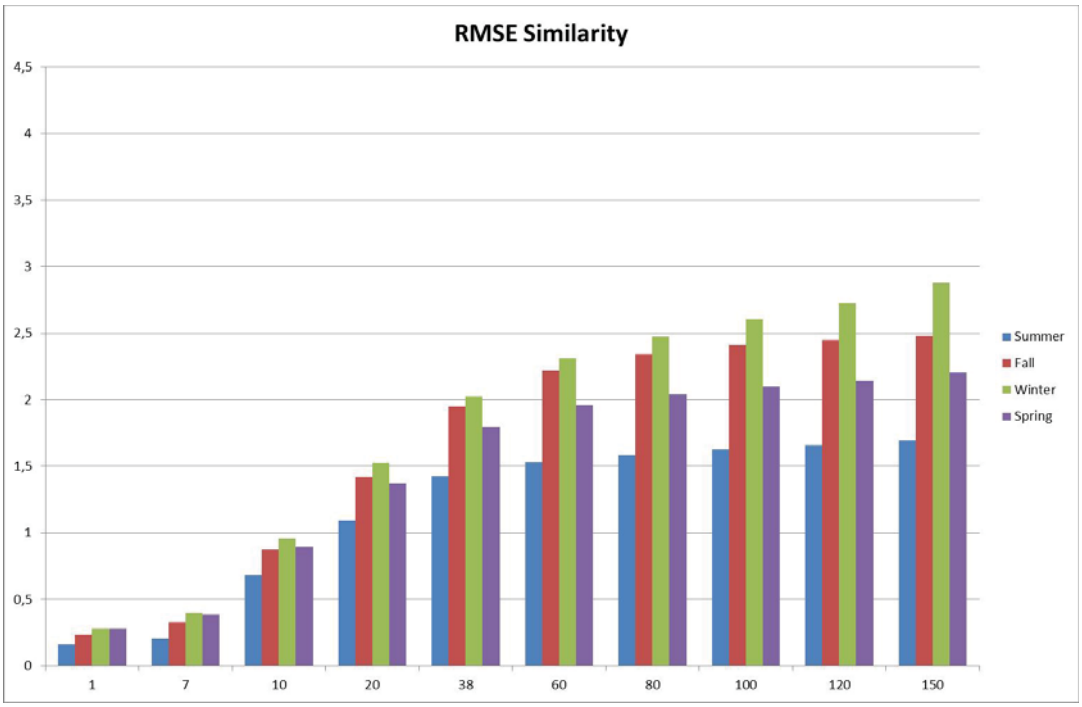

Figure 4.10: Root mean square error between modeled wind profile with similarity theory and data from Wind Lidar

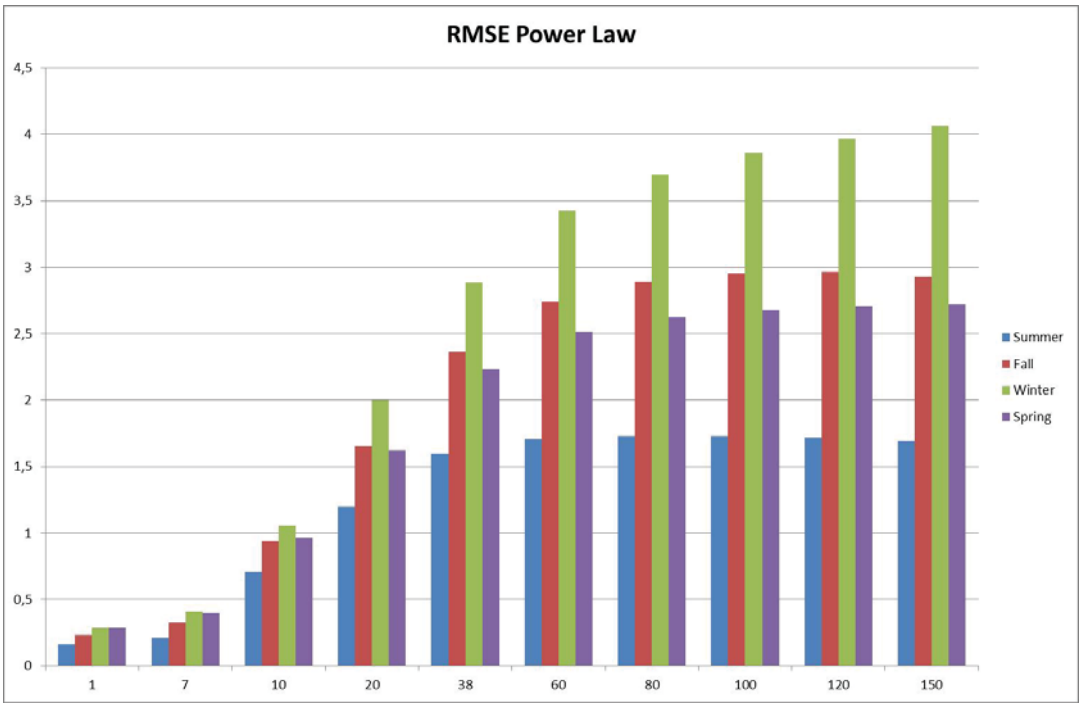

Figure 4.11: Root mean square error between modeled wind profile with power law theory and data from Wind Lidar

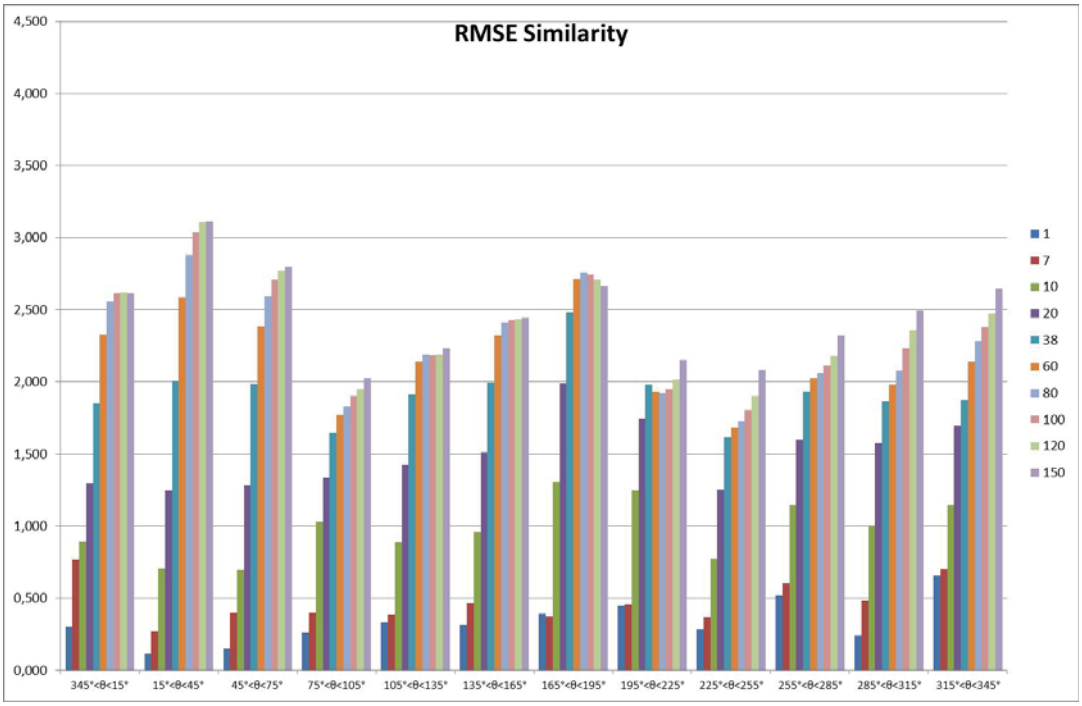

Figure 4.12: Angular distribution of RMSE's for all levels (Similarity theory).

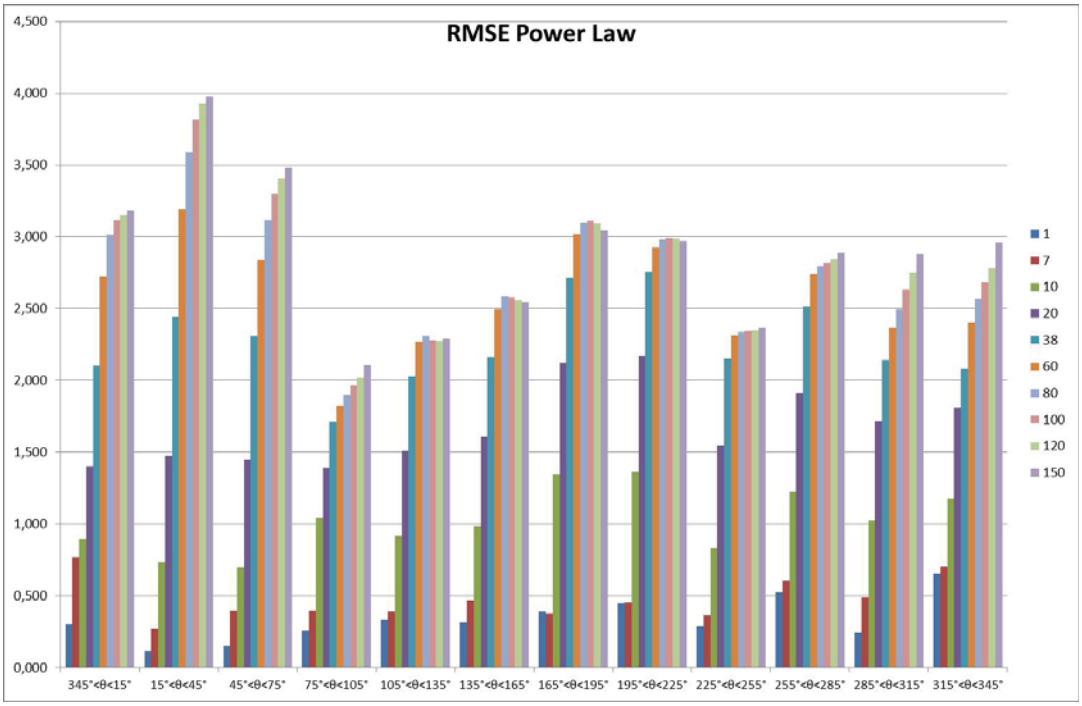

Figure 4.13: Angular distribution of RMSE's for all levels (Power law theory).

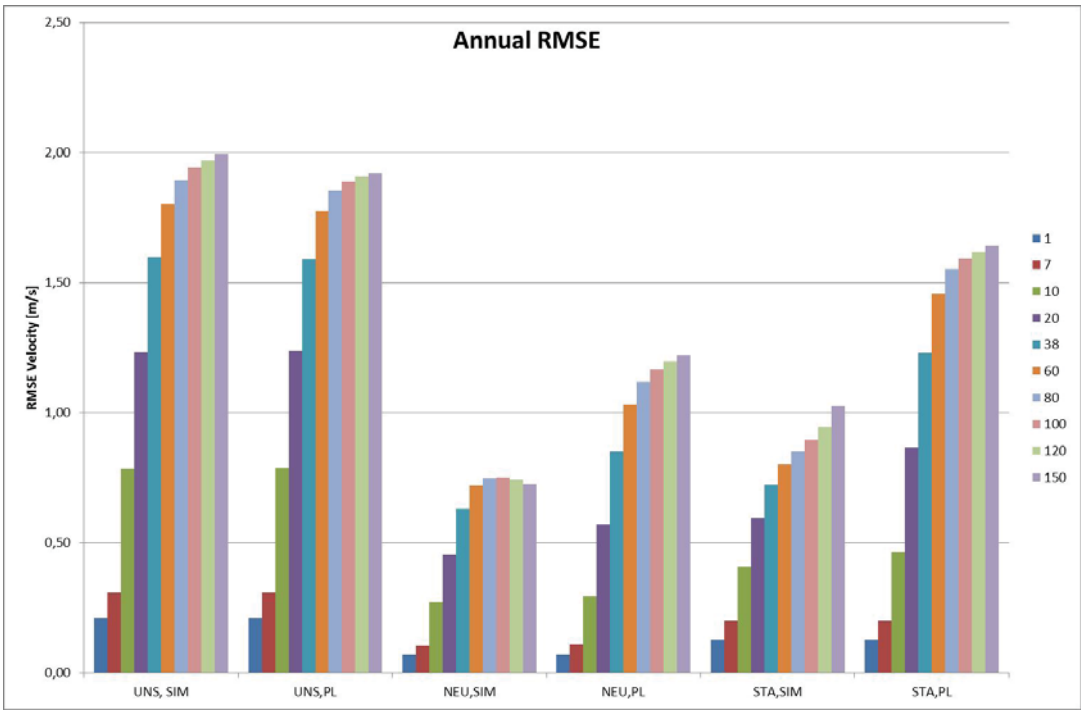

Figure 4.14: Annual RMSE for the two methods (SIM=similarity, PL=power law) and for the three stability conditions: unstable (UNS), neutral (NEU) and stable (STA). At each color corresponds a different height, indicate on the right legend (in m).

Chapter 5

Wind forecast by regional model

In this chapter the methodology to calculate wind power forecast is presented. The model used for the forecast is the Regional Atmospheric Model System (RAMS) with resolution of 3 km. All the output have been verified utilizing 42 Synop stations located in South Italy, distributed through the Telecommunication System Global web (GTS). For this verification temperature and humidity also the parameters that we focus on, i.e. the wind speed and wind direction are used.
The wind velocities at different levels are tested utilizing a experimental data set from wind Lidar for the period between July and November 2013: this instrument is located in Calabria, a region of South Italy, near the UOS CNR-ISAC of Lamezia Terme (Catanzaro). As results of this work we obtained a methodology to calculate the power curve of wind plant knowing data of a power plant for a limited period, or to forecast the energy produced by theoretical power curve knowing the forecast on wind speed.

5.1 The RAMS model and its configuration

RAMS is a mesoscale atmospheric computer model originally developed at Colorado State University and updated continuously in the years at ISAC-CNR Federico [23]. Since its birth the model goal is to simulate meteorological phenomena and to be adaptable at applications ranging from operational weather forecasting to air quality regulatory applications to support of basic research.
RAMS is the result of two earlier atmospheric modeling programs conducted independently during the 1970's. A cloud model developed under the direction of Dr. William R. Cotton contributed state-of-the-art methods for modeling microscale dynamic systems and cloud processes. A mesoscale model developed under the direction of Dr. Roger A. Pielke contributed expertise in the modeling of mesoscale systems and the influence of land-surface characteristics of the atmosphere. In 1986, the process was begun of merging the capabilities of the two models into a unified multi-purpose modeling system, and thus was born the new RAMS Pielke et al. [58].
RAMSs̀ codes were developed for research in phenomena on the mesoscale with multiple

selectable options for the modeling of specific physical processes, in flexible domain and boundary conditions, variable computational techniques, and multiple coordinate systems. The atmospheric model is constructed around the full set of primitive dynamical equations which govern atmospheric motions, and supplements these equations with optional parametrizations for turbulent diffusion, solar and terrestrial radiation, moist processes including the formation and interaction of clouds and precipitating liquid and ice hydrometeors, sensible and latent heat exchange between the atmosphere, multiple soil layers, a vegetation canopy, surface water, the kinematic effects of terrain, and cumulus convection. All these characteristic make RAMS a powerful tool for atmospheric research also in environment with a complex orography like Italy.
A detailed description of the RAMS model is given in Cotton et al. [20], while the following is a brief description of the model setup used in this work. Two two-way nested domains at 12 km and 3 km horizontal resolutions, respectively, are used.
RAMS is a limited-area model, but it may be configured to cover an area as large as a planetary hemisphere for simulating mesoscale and large scale atmospheric systems. Two-way interactive grid nesting in RAMS allows local fine mesh grids to resolve compact atmospheric systems such as thunderstorms, while simultaneously modeling the large scale environment of the systems on a coarser grid. In our studies two-way nested domains at 12 km and 3 km horizontal resolutions, respectively, are used. The choice of these resolutions is inside the possibility to reproduce effects on scale of few kilometers as marine and mountain breezes. The first grid covers the Central Mediterranean Basin while the second extends over the whole southern Italy (Table 5.1, Fig. 5.1). Thirty-five vertical levels, up to 21797 m in the terrain-following coordinate system, are used for both domains. Levels are not equally spaced: layers below 1500 m a.g.l. are between 50 and 200 m thick, whereas layers in the middle and upper troposphere (>7000 m a.g.l.) are 1000 m thick.
The Land Ecosystem-Atmosphere Feedback model (LEAF) is used to calculate the exchange between soil, vegetation, and atmosphere [3]. LEAF is a representation of surface features, including vegetation, soil, lakes and oceans, and snow cover, and their influence on each other and on the atmosphere.

Parameters	Domain D1	Domain D2
N° Points Longitude	261	254
N° Points Latitude	241	222
N° Points Altitude	35	35
Dimension Longitude	3120 km	759 km
Dimension Latitude	2880 km	663 km
Dimension Altitude	21797 m	21797 m
Resolution	12 km	3 km
CENTLAT ($\circ$)	42.0	39.8
CENTLON ($\circ$)	12.5	15.7

Table 5.1: Setup up parameters

Seven precipitation categories are provided by implemented explicit micro-physics prognostic equations: cloud water, rain (liquid), pristine ice, snow, aggregates (completely frozen), graupel, and hail (mixed-phase categories) Federico et al. [25]. The scheme uses a generalized gamma size-spectrum and uses a stochastic collection rather than a continuous accretion. The scheme includes a heat budget equation for each hydro-meteor class, allowing heat storage and the existence of mixed phase hydrometeors.
Sub-grid-scale effect of convective and non-convective clouds is parametrized following Mastrantonio et al. [47] who proposed a simplified form of the Kuo scheme Ferretti et al. [29] that accounts for updrafts and downdrafts. This scheme is utilized to parametrize deep cumulus convective process and, then, it is responsible to simulate precipitation. The Kuo method is attractive because it is simple and economical relative to mass-flux method and it depicts a physically reasonable link between large-scale moisture convergence and cumulus convection. In the Kuo convective parametrization, the moisture that is supplied by large-scale environment and evaporation from the surface maintains penetrative cumulus convection. The cumulus heating and moistening imparted to the large-scale environment is assumed to be proportional to the temperature and water vapor mixing ration difference between the environment and cloud,; in this way the environmental temperature profile moves through the depth of a cloud toward a low level moist adiabatic.
The RAMS parametrizes the unresolved transport using K-theory: in this method the covariance is formalized as the product of an eddy mixing coefficient with the gradient of the transported quantity. The turbulent mixing in the horizontal directions is parametrized following Smagorinsky [63] which relates the mixing coefficients to the fluid strain rate and includes corrections for the influence of the Brunt-Vaisala frequency and the Richardson number Pielke et al. [58].
A full-column, two-stream single-band radiation scheme is used to calculate short-wave and long-wave radiation Chen and Cotton [19]. The Chen and Cotton scheme accounts for condensate in the atmosphere, but not whether it is cloud water, rain, or ice.
Using this RAMS model configuration, a one-year forecast (1 December 2012- 30 November 2013) was made. The forecast starts, for each day, at 12 UTC and lasts 84 h and the model output is available every hour. The first 12 hours of each forecast are spin-up time and are discarded from the verification process. This time is enough to reach a dynamical equilibrium of the physical and dynamical components of the model, as reported in a previous study Federico et al. [24]. Initial and boundary conditions are given by the ECMWF operational analysis and forecast cycle at 12 UTC.
The code is written almost exclusively in FORTRAN 77 with some common extensions, although some C code is used to facilitate I/O procedures and dynamic memory allocation.

5.2 Verification of the model performance

A evaluation of model performance is evaluated to test the goodness of the predictions and to prove the validity of the wind power estimation. In particular our attention is focused

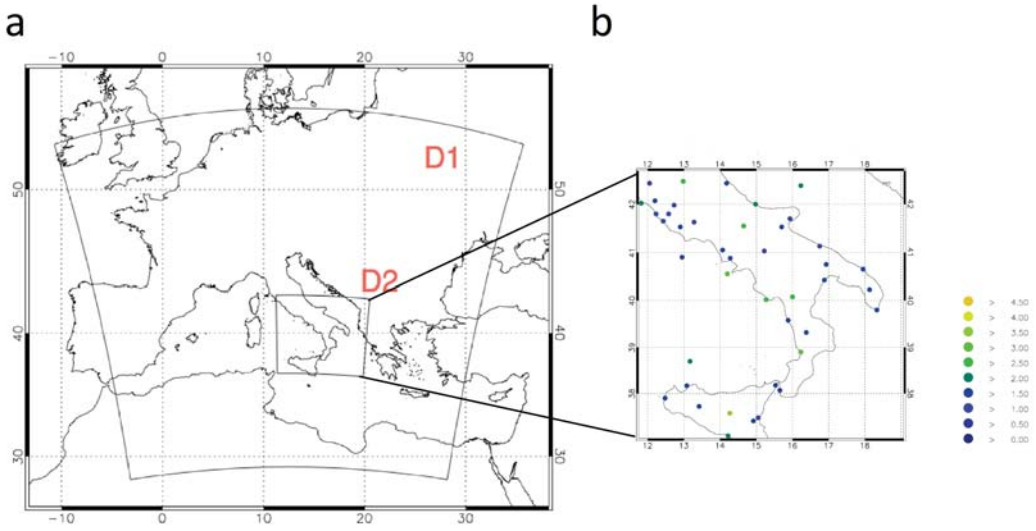

Figure 5.1: a) RAMS domains, and; b) GTS stations employed for errors calculation over the second domain.

for the following surface parameters: temperature, relative humidity, wind speed and wind direction.
Other previous studies Federico et al. [26] verify the performance of model, but, it is the first time that a better resolution (from 6 km of Federico et al. [26] to 3 km of our work) and a statistical technique are used to reduce the errors between observations and predictions.

5.2.1 Data from Ground Telecommunication System

The observational data set used to quantify the model performance is formed by the reports of the SYNOP stations, which are distributed through the Ground Telecommunication System (GTS).
All the data of GTS respect a specific standard that could be summarize in this six design principles (for more information VV. [71])
Principle 1
The Global Telecommunication System shall be designed as an integrated network for the collection, exchange and distribution of information on a worldwide basis, with a view to meeting, efficiently and effectively, the requirements of all National Meteorological Services and also the requirements of World and Regional Specialized Meteorological Centres, within the agreed World Weather Watch (WWW) system.
Principle 2
The system shall comprise an integrated network of point to point circuits, point to multipoint circuits, broadcast and multipoint to point circuits which are reliable and have suitable technical and operational characteristics. These circuits may be established via a

combination of terrestrial and satellite telecommunication links, and data-communication network services.
Principle 3
The circuits to be provided and the techniques to be employed shall be adequate to accommodate the volume of meteorological and related information and its transmission within the required time limits to meet the needs of World, Regional Specialized and National Meteorological Centres.
Principle 4
In the planning of the circuits and transmission schedules, daily volume of traffic to be passed over any one circuit shall not exceed 80 per cent of its theoretical capacity. The circuits shall be designated to ensure the highest practicable reliability and availability.
Principle 5
The system shall be based mainly on the interconnection of a number of centres, namely, National Meteorological Centres (NMXs), Regional Specialized Meteorological Centres (RSMCs), Regional Telecommunication Hubs (RTHs) and World Meteorological Centres (WMCs). The WMCs, RSMCs and RTHs shall be provided with suitable equipment for selection and editing in order to provide NMCs with the data selected to meet the NMC-sśpecified needs.
Principle 6
Provision shall be made for alternative routeings where practicable, to ensure the reliability and efficiency of the system, particularly the reliability and efficiency of the Main Telecommunication Network.

All the forecast is bi-linearly interpolated to the position of the SYNOP observations. Statistics have been calculated over the RAMS nested domain (southern Italy) where GTS counts 42 surface stations (Fig. 5.1). The availability of the number stations varies from 10 to 42 depending on the day and on the time of the day. Even if there are comparatively more stations in the coastal areas than inland, the reports of the SYNOP stations are reliable and stable in time giving a unique sample for the forecast verification.

5.2.2 Scores

The statistical scores computed for the meteorological parameters are:

- Bias or mean error (hereafter also BIAS): measures the mean difference between observation and simulation:

$$BIAS = \frac{1}{N}\sum_{i=1}^{N}[Forecast_i - Observation_i)] \tag{5.1}$$

- Mean absolute error (hereafter also ABS): measures the mean amplitude of the sim-

ulation error with respect to the observation:

$$ABS = \frac{1}{N}\sum_{i=1}^{N} Forecast_i - Observation_i \tag{5.2}$$

- Root mean square error (hereafter also RMSE): measures the mean square gap between observed and modeled data:

$$RMSE = \sqrt{\frac{1}{N}\sum_{i=1}^{N} (Forecast_i - Observation_i)^2} \tag{5.3}$$

where N is the total number of observation-forecast pairs entering the statistic. This number varies from data availability, for example with season or forecasting time, depending on the number of available GTS reports.
These errors have been calculated for 12 months (1 December 2012- 30 November 2013) and shown for different seasons: in this way it is possible understand better the performance of the model related at the importance of the seasonal cycle in the Mediterranean Basin climate.

5.2.3 Variability of errors on seasonality and on forecasting time

All the scores calculated could said us more on climate and on ability of model to predict the principal characteristics of the wind speed and wind direction if we related them at the variability on the seasonality and on forecasting time Tiriolo et al. [68]. A example of this variability is shown in Fig. 5.2: there is a different behavior of the wind speed for winter and fall compared to summer and spring. Meanwhile in winter and fall the forecast underestimates the observed values for all forecasting times, (values ranging from -0.3 m/s to -0.7 m/s), in summer and spring a clear diurnal cycle is shown with negative values at midnight and small values, positive or negative depending on the forecasting time, for midday.
The RMSE for wind speed (Fig. 5.2) ranges between 2.0 and 2.8 m/s. The largest values are for winter and spring and the smallest values for summer and fall.
The BIAS of wind direction (Fig. 5.3) ranges between -6.5 and 3 degrees, depending on the season and forecasting time, but anyway there is no particular behavior related to seasonality changes: instead, this aspect is connected at the rather homogeneous distribution of GTS data set (Fig. 5.1). The positions of the stations are both inland and on seaside, with sea at west or east side, on sea level and up to a mountain, and for this the direction depend also on the preferential direction of each measure station.
With RMSE, because of definition itself (Eq. 5.3), it is possible to seen a variability on season and forecasting time (Fig. 5.3b): RMSEs range between 56 and 74 degrees, but there is a small increase of the error with forecasting time superimposed to a diurnal cycle.

In the summer the errors (especially at 00 UTC) are more evident in according to increasing of diurnal cycle.
If we compare Fig 5.2 and Fig 5.3 we can see that the wind speed has a lower error in summer, while the wind direction has a lower error in winter. Another time, this effect could be caused by the positions of SYNOP stations. Most of them are collocated near the sea and in the summer local climate (sea breeze) play a major role than synoptic circulation (perturbation) and this causes a behavior of RMSE related more at particular position of the station Federico et al. [28]. In addition to these consideration in summer, the wind speed is lower and has a larger diurnal cycle than in winter. In these conditions the wind direction is variable, especially for low wind speed, as at midnight (Fig. 5.3). In winter the wind speed is higher than in summer and the circulations are focused on specific directions, which are determined, from case to case, by the synoptic scale forcing. A wind-speed diurnal cycle is also present in winter, but its amplitude is lower than in summer.
The forecast is less able to follow the larger variability of the wind direction in summer (depending on the position of the measure stations) compared to the more focused direction in winter (depending only by global circulation), so the errors for wind directions are larger in summer than in winter. It is also noticed that the forecast overestimates the amplitude of the diurnal cycle in winter, and this is another source of error causing a larger RMSE for wind speed in winter compared to summer.
On the other hand, the model is more able to predict the lower wind speed and its regular diurnal cycle in summer compared to the stronger winds occurring in winter.
To analyze more in detail the diurnal cycle of the errors and the different behavior among seasons, Fig.s 5.4a and Fig. 5.4b show the time series of the observations and forecast for temperature and wind speed in summer and winter. Time series are computed by averaging the observations and the forecast over the second domain of the RAMS forecast (Fig. 5.1).
Considering the temperature in winter and summer, we notice the larger amplitude of the diurnal cycle in summer showing, indirectly, the importance of local circulations in this season. Both in winter and summer the model underestimate the observed temperature, especially during the daylight hours.
Also in Fig. 5.4b than in Fig. 5.5b it is possible to see, how reported above, that the wind velocities are larger in winter than in summer. Finally we notice that the forecast underestimates the wind speed both in summer and winter (see also Fig. 5.2a).

5.3 Statistical forecasting by MOS

Meteorological parameters estimated by the model are affected by errors and therefore require methods of correction for a more adequate prediction. To minimize the BIAS errors and to improve all the scores of a a-posteriori correction technique (Model Output Statistics, MOS) is used (Glahn and Lowry [32], Carter et al. [16], Kalnay [43],Wilks [73]). The MOS technique, was applied to the surface of different meteorological parameters:

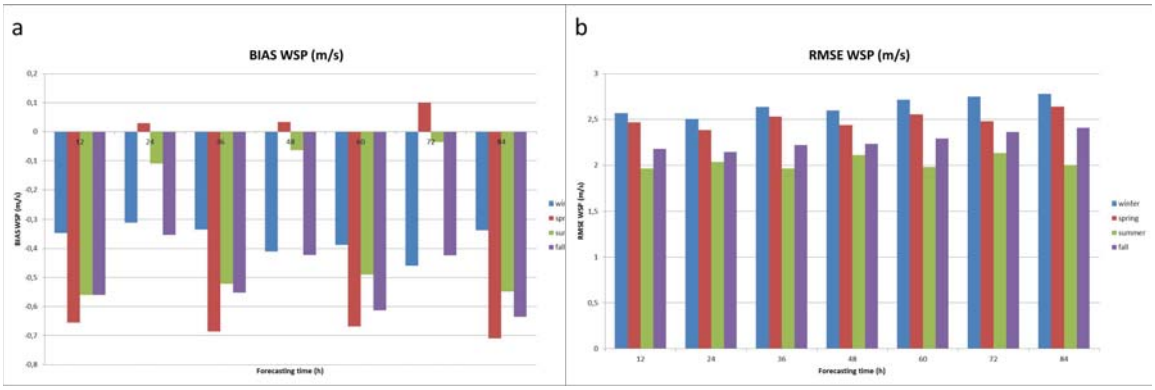

(a) BIAS (b) RMSE

Figure 5.2: BIAS (a) and RMSE (b) for wind speed for the four seasons.

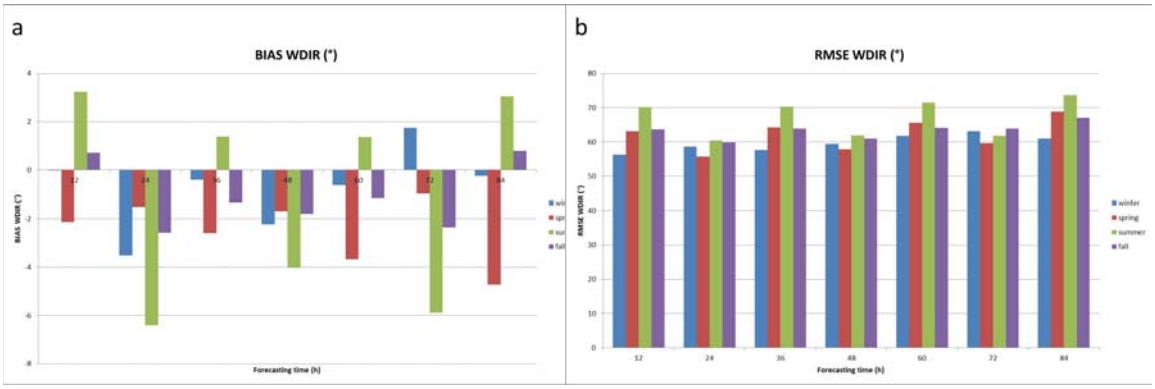

(a) BIAS (b) RMSE

Figure 5.3: BIAS (a) and RMSE (b) for wind direction for the four seasons.

temperature, relative humidity, wind speed and wind direction.
There are two basic reasons to apply the MOS technique to the output of numerical weather prediction models:

1. The numerical models are not perfect and have systematic errors (biases). Statistical forecast may compensate and correct those biases.

2. The surface conditions are homogenize by the models because they represent reality with a finite number of grid points. In this representation many important small-scale effects that may have an important impact on local weather and climate are missed (for example the presence of small surface water bodies or local topography). Statistical relationship may be derived between the models output and the desired forecast quantities to give a closer representation of the real world.

The used linear regression curve has as a predictor the prediction model in correspondence of a station and as predictand the observed value at the same station. For each predictor

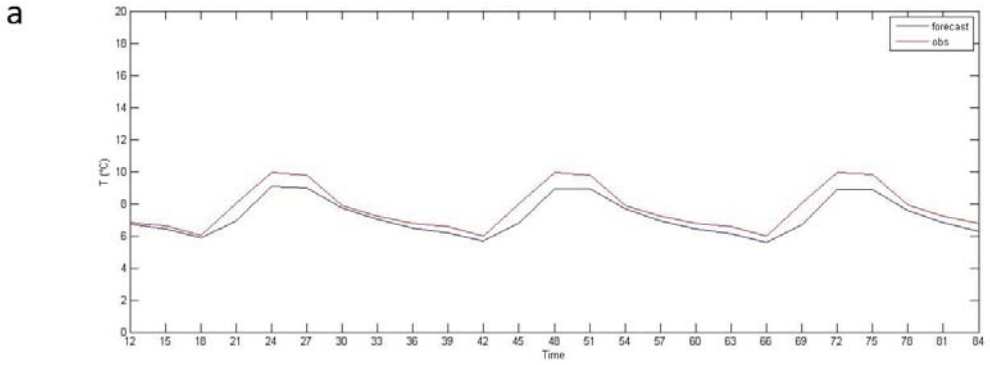

(a) Temperature

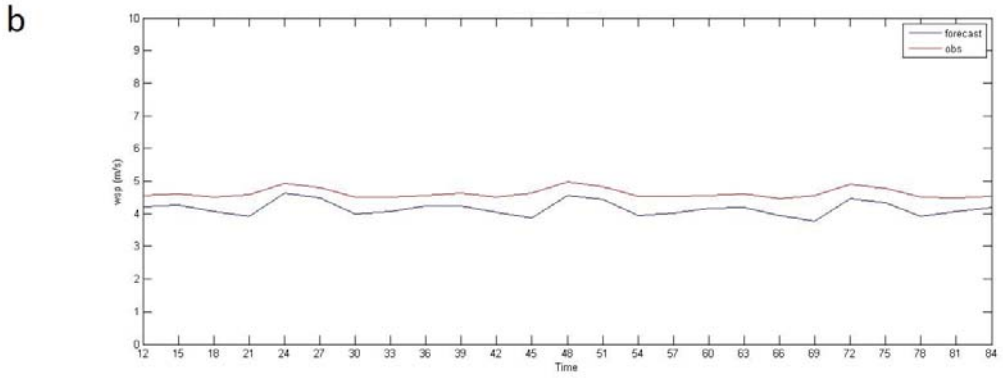

(b) Velocity

Figure 5.4: Time series for the forecast and observations for temperature (a) and wind speed (b) in winter.

is considered only one predictand.
To make the correction, the MOS was applied to 90% of the sample, then using the remaining 10% to perform the prediction using the regression parameters obtained through the MOS.
This procedure was applied 50 times, each time using different data randomly selected for the MOS and for the prediction.
Figure 5.6a shows the difference between RMSEs ($\Delta RMSE$) without using the MOS and using the MOS for surface temperature for spring; this season was chosen for brevity, but similar results were found for other seasons.
A positive value means that the forecast is improved by the MOS. Considering the average of the $\Delta RMSE$ for the fifty-MOS applications, an improvement of ~ 0.4 K is gained for all forecasting times. The improvement is about 30% of the RMSE without MOS, showing an important impact of the MOS on the forecast. The result is statistically robust because

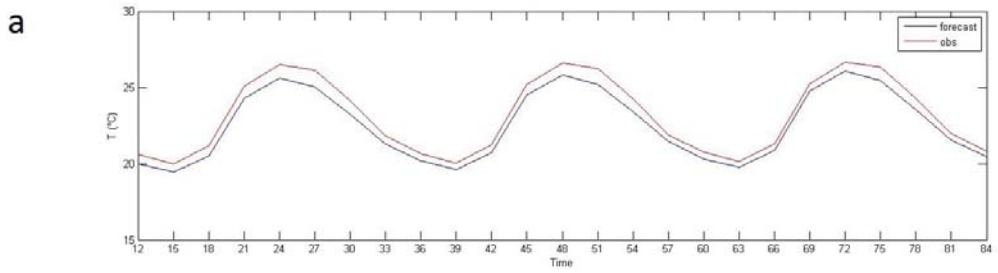

(a) Temperature

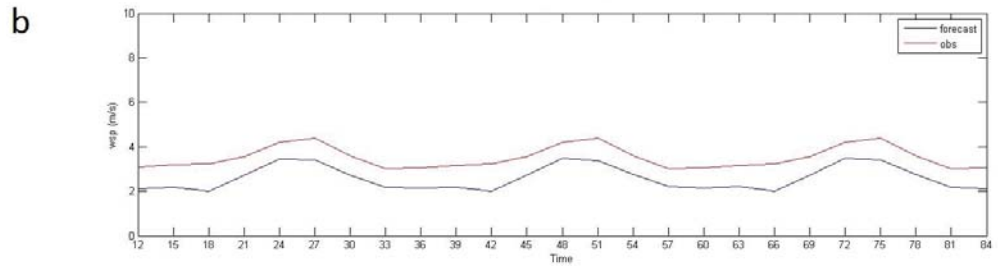

(b) Velocity

Figure 5.5: Time series for the forecast and observations for temperature (a) and wind speed (b) in summer.

there is an improvement for all the fifty MOS tried and the 25th percentile shows always values larger than 0.2 K, i.e. larger than 10% of the RMSE without MOS.
To further quantify the improvement of the forecast gained by MOS, we performed the forecast of the spring season without using the second RAMS domain (3 km horizontal resolution, Figure 5.1). For this forecast the horizontal resolution is 12 km and considering the complex orography of the studied area, an important impact of the horizontal resolution on the surface temperature forecast is expected. The dashed line in Figure 9a shows the RMSE difference between the forecast using only one grid (G1, 12 km horizontal resolution) and the forecast using both domains (G2, 3 km horizontal resolution). A positive difference shows an improvement of the forecast using both domains. As expected the impact of increasing the horizontal resolution is noticeable with maximum values of the RMSE difference between G1 and G2 around 0.6 K. It is interesting to note, however, that the improvement gained by enhancing the horizontal resolution from 12 km to 3 km is comparable with that gained by the MOS.
These results show the importance of using a statistical correction as MOS to the RAMS forecast, especially considering the limited amount of computing time required for the MOS application.
Figure 5.6a quantifies the impact of the MOS on the relative humidity forecast. The improving using the MOS is about 2.5% that must be compared with the RMSE of ~ 15 without using the MOS. Results are statistically robust and the improvement of the 25th

percentile is larger than 2% for most forecasting times.
The result for wind speed, Figure 5.6c, shows again a positive and important impact of the MOS. The $\Delta RMSE$ is above 0.3 m/s for all forecasting times, i.e. between 10 and 20% of the RMSE without MOS (2.5 m/s, Figure 5.2b). Also this time result is statistically robust because all the fifty MOS applications give a forecast improvement, which is larger than 10% most of forecasting times.
In both previous cases the improvement introduced by MOS is larger than that obtained increasing the forecast resolution from 12 to 3 km. Figure 5.6d shows the result of the MOS application to the forecast of the wind direction. The $\Delta RMSE$E average shows positive values for all forecasting times and there is an improvement to the forecast using the MOS. However, the impact of MOS is negligible for midday-early afternoon while it increases at night, when values of $\Delta RMSE$ are around 5∘. For wind directions results are statistically less robust compared to other parameters because the forecast using MOS is sometimes worse than that without MOS ($\Delta RMSE < 0$). Nevertheless, as noticed above, the average of $\Delta RMSE$ is positive for all forecasting times and the 25th percentile of the $\Delta RMSE$ is also positive for most of the forecasting times, showing the usefulness of the MOS also for the forecast of the wind direction.

The our results show that RMSE is almost 2.0-2.8 m/s for wind speed and $56 - 74$∘ for wind direction and that the performance varying with the season and with the forecasting time.
The error increases by 10% of its initial value between the first and third forecast day.
The statistical method used is a widely used post-processing technique, namely Model Output Statistics (MOS). The MOS implemented has one predictor, i.e. the model forecast at the observational point for the meteorological parameter being predicted, for each predictand, which is the observed meteorological parameter. For our verification the MOS reduces the RMSE by $10 - 30$%, depending on the forecasting time, on the season and on the meteorological parameter. This results is true for all parameters, except for the wind direction, where the RMSE reduction at night is > 10% with negligible effects during day hours.

An important subject investigated in this study is the improvement of the forecast performance by statistical forecasting through MOS. The MOS is an effective and computational cheap way to reduce the forecast error because it compensates for model biases and for the missing of important small-scale effects that may have an important impact on the local weather. Anyway it is impossible to replace the improvement on the resolution with the application of a statistical method. MOS is unable to estimate the phenomena at little scales such as breeze or the particular interactions between wind and the orography, that it is possible to do only using an model resolution increasing: finally it is possible to conclude that both improvements are necessary to reduce all scores.

a

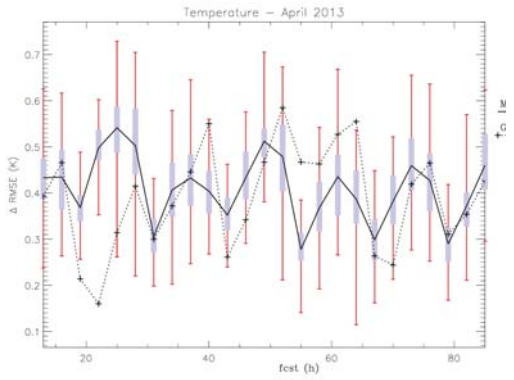

(a) $\Delta RMSE_{Temperature}$

b

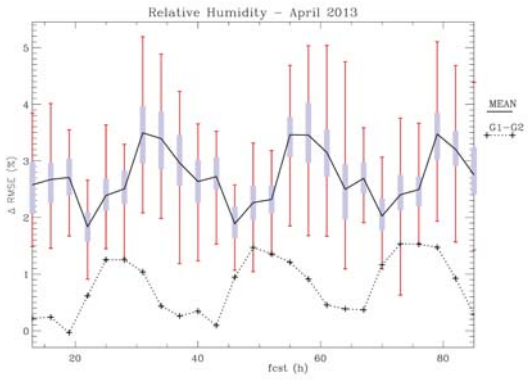

(b) $\Delta RMSE_{humidity}$

c

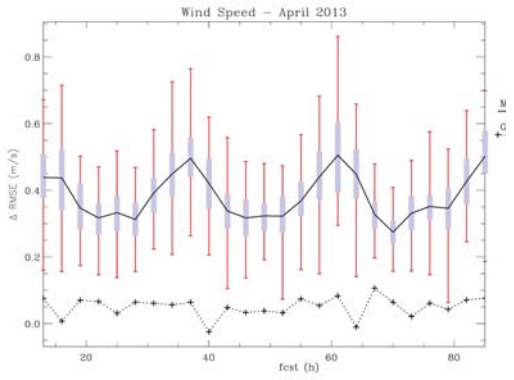

(c) $\Delta RMSE_{Velocity}$

d

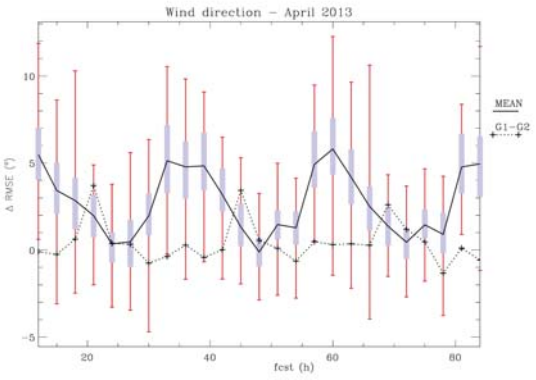

(d) $\Delta RMSE_{Direction}$

Figure 5.6: The RMSE difference (ΔRMS)

5.4 Wind and power energy verification with Wind Lidar

The RAMS output are also tested with data acquired from wind LIDAR located at Lamezia Terme CNR-ISAC experimental field (see the specific section). In the comparison with wind LIDAR we matched observed and model data for four levels (20, 80, 150, 200 m) on the

period July-November 2013.

For wind speed lowest and highest levels present lower errors, meanwhile intermediate ones have higher errors, maybe due to the presence of low level jet, not predicted by model (Fig. 5.7). Low level jet (known also as nocturnal jet) occurs when the wind on land usually decreases its intensity or presents calm, meanwhile at bigger heights the wind tends to accelerate, also toward super geostrophic velocity B. [6]. That particular phenomenon is caused when the bottom of Residual Layer (well mixed neutral layer present since sunset, where the pollutants are trapped inside it and can interact between them creating more complex forms) that does not interact with the ground begins to transform and to interact with the ground. This transition is characterized by air statistically stable with weak and sporadic turbulence. The statistically steady air tends to generate turbulence, meanwhile the nocturnal jet that are developing increase interaction with the underlying and the overlying atmosphere layers. These interaction generates turbulence that, some times, takes place in a relatively short burst that can cause mixing within the Stable Boundary Layer (SBL). These conditions are favored by a falling of cold air from the hills located in the east direction of the experimental field Whiteman et al. [72].
For wind direction errors are higher in the lowest levels because of the increased number of events of calm winds (Fig. 5.8): this effect is more evident for the lower levels.

5.5 Wind power forecast

5.5.1 Power curve from wind forecast

After obtaining a verification of RAMS model at ground level with the GTS data and for different level with data from Lidar, a wind power forecast in Central Italy is been achieved. The previous grids are moved to reproduce, with resolution of 3 km, the output data of the considered wind farm located in a complex topographical region (Fig. 5.9).
The power data are provided by Edison Energia inside a benchmark proposed by COST Action ES1002 WIRE. In this power plant there are different kind of turbine, with capacity varying from 1.2 to 16.8 MW and they are placed in six different boroughs, away also tens of kilometers. In addition the terrain where the power plant is located presents a very complex orography Tiriolo et al. [67].

The procedure for the forecast of the power production by the wind farm was divided in two phases:

1. finding a law representing the power curve of the production of the whole wind farm for the whole spectrum of wind speed in the area;

2. forecasting the power produced by the wind farm starting from the RAMS forecast for the next 48 h using the power curve obtained in 1.

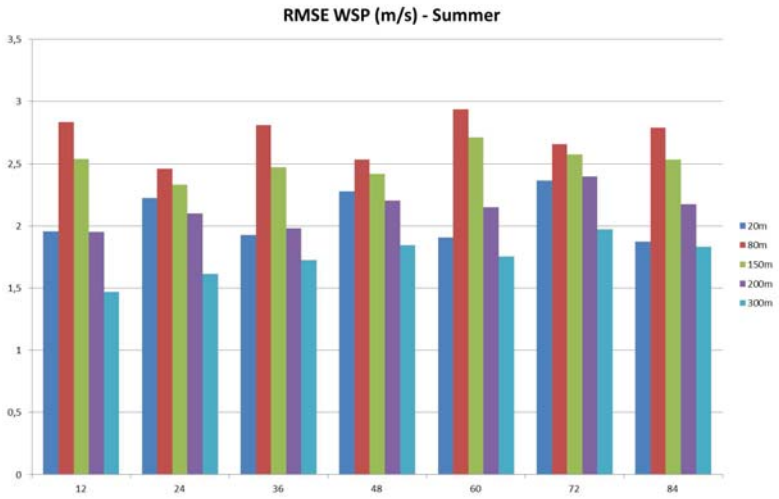

(a) Summer

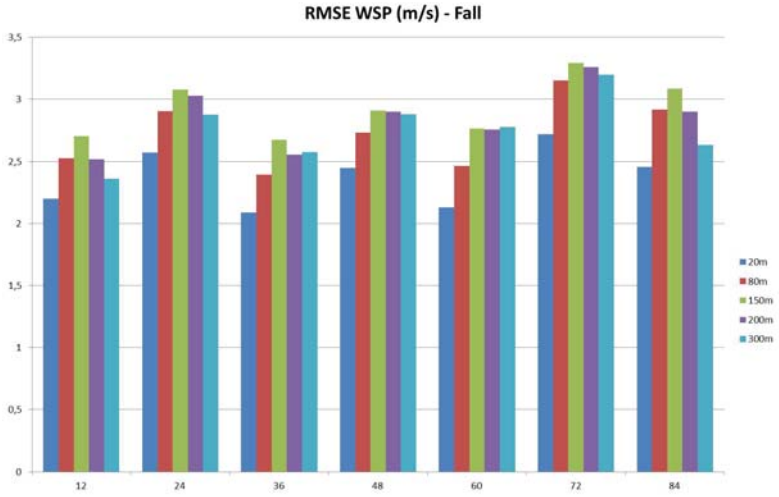

(b) Fall

Figure 5.7: Comparison between wind forecast from RAMS and data from wind Lidar located at Lamezia Terme CNR-ISAC experimental field for Summer 2013 (a) and Fall 2013 (a)

For the step a) a two years period (2010-2011) has been considered. For this period, the RAMS model was run for 12 hours (starting at 12 UTC) using ECMWF (European Centre for Medium range Weather Forecast) analysis as initial and boundary conditions (hindcast). The results of the hindcast have been used to find the power curve (Fig. 5.10) of the wind farm. To fit the data, the sample has been divided in bins 0.5 m/s wide; for each bin, we computed a power output (fitting power) by minimizing the variance between the power values inside the bin and the fitting power. As second step 2. A one year forecast

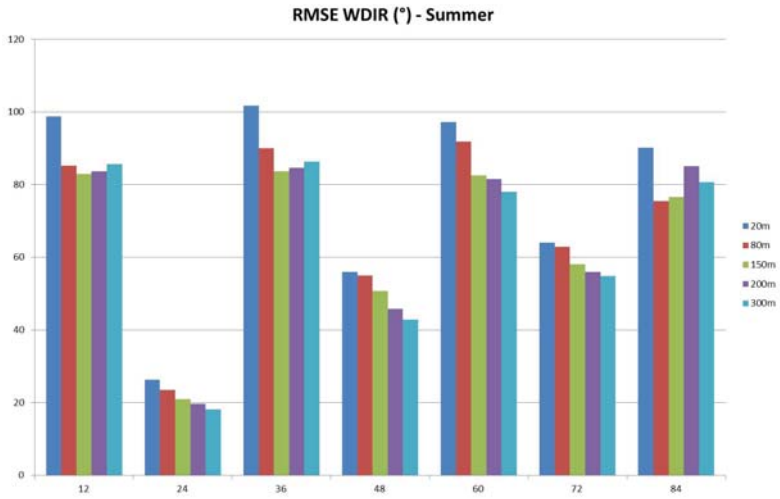

(a) Summer

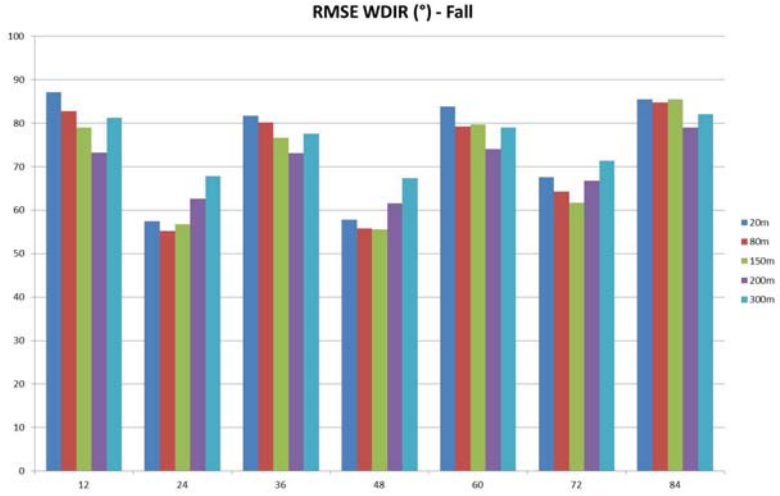

(b) Fall

Figure 5.8: Comparison between wind direction forecast from RAMS and data from wind Lidar located at Lamezia Terme CNR-ISAC experimental field for Summer 2013 (a) and Fall 2013 (a)

(2011) has been considered, producing RAMS forecast for the following two days. Initial and boundary conditions are given by the ECMWF 12 UTC analysis/forecast cycle. The wind speeds obtained by the outputs of this model where then used to produce the power forecast, by employing the power curve obtained in a).
To better evaluate the forecast performance, the procedure of the points 1. and 2. has been repeated using the forecast issued by the IFS (Integrated Forecasting System) model of European Centre for Medium-Range Weather Forecasts (ECMWF).

The performance of the wind power forecast is evaluated for both RAMS and IFS forecast for the whole 48 h. Statistics were computed for each season as well as for the whole year. In every case RAMS model gives better performance 5.2.

In Fig. 5.11 there is the comparisons among wind power calculated from RAMS, from IFS and observed values for the period 15th-20th December 2012: this period is chosen as example to compare the different data. The RAMS and IFS show a similar behavior of wind forecast (not shown) but the RAMS values are larger for this period. The RAMS power forecast follows more closely the observed power compared to IFS.
The period 15-20 December 2012 was characterized by the passage of cyclones over the Mediterranean Basin. For example, on 19 December 2012 the RAMS hindcast at 00 UTC shows the passage of a cyclone in central Italy (5.12a). The cyclone evolved in a cut-off at 500 hPa and air masses crossed the central Italy from west to east. The orography of the Apennines generates gravity waves (5.12b), and the interaction between air-masses and orography is simulated better by RAMS compared to IFS because of its higher horizontal resolution.

5.5.2 Wind power maps

For all other portions of the grid the power forecast is calculated using a theoretical power curve, i.e. that of a Vestas Wind Turbine with nominal power of 600 kW art [2]. An example is shown in the Fig.s 5.13 e 5.14 for the city of Cosenza in the South Italy. How it is possible to see the wind are more intense on sea than in land due the presence of obstacles and roughness that, in land, slow down the wind force. In this way also the power energy predicted is higher on the sea that on land. In particular it is possible to note that in the middle of the land, there are some peaks because the presence of mountains. In little words it is possible say that the power energy is related to altitude of the point where it is calculated.
Finally there is a zone with high power predicted at the bottom of the Fig. 5.14. These place is characterized by a gap (the Marcellinara gap) between the mountains, that link

Figure 5.9: Wind Farm in Abruzzo, in the Central Italy

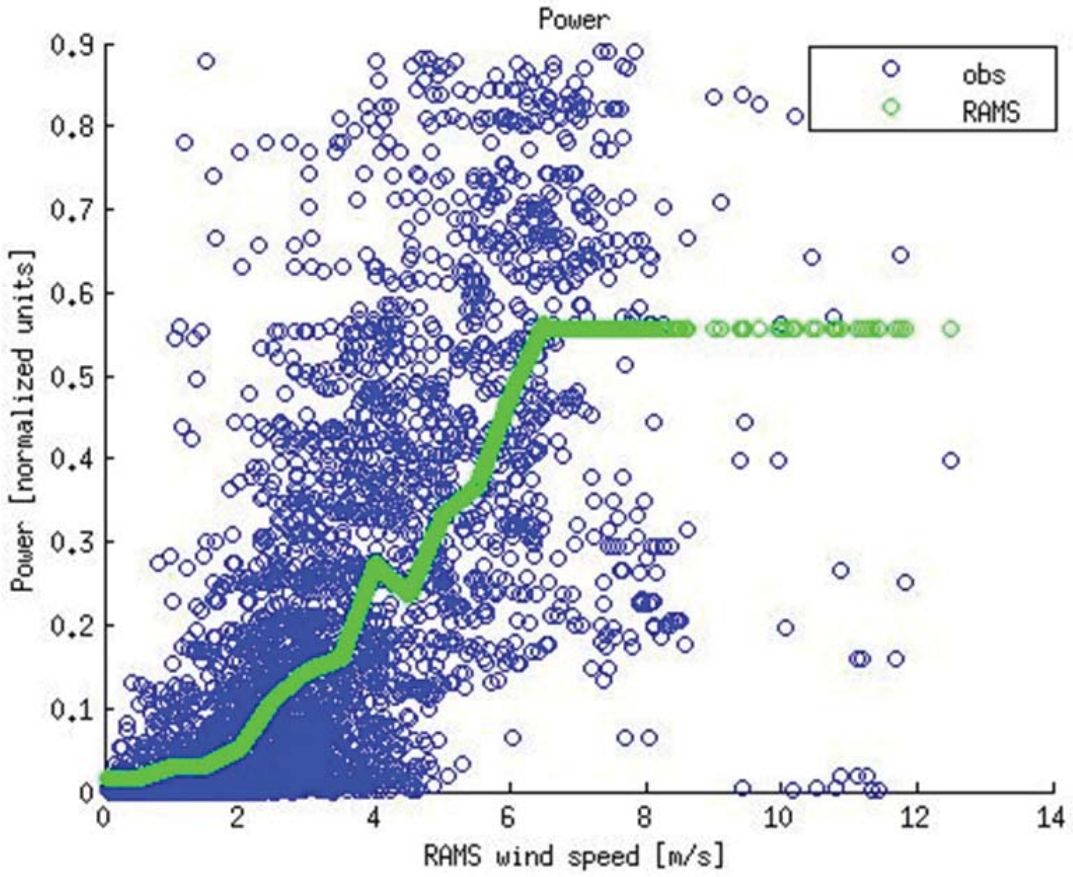

Figure 5.10: This figure shows observed wind energy power (blue dots) and calculated wind energy power (green dots) against model wind velocity. The green dots are calculated with the methodology described above and all together have the characteristics of a typical power curve shape.

Periods	Statistics	Error (RAMS) [W]	Error (IFS) [W]
Winter			
	ABS	12374	14031
	BIAS	3786	1329
	RMSE	17086	19948
Spring			
	ABS	10121	11510
	BIAS	-2236	-4204
	RMSE	14060	16980
Summer			
	ABS	10411	10604
	BIAS	-1881	-3168
	RMSE	16864	17743
Fall			
	ABS	9517	11129
	BIAS	-2986	-5113
	RMSE	14851	18708
Whole Year (2011)			
	ABS	10598	11827
	BIAS	-850	-2782
	RMSE	15752	18375

Table 5.2: Errors for power forecast for RAMS and IFS for all the seasons and for the whole year (2011).

the Ionian and Tyrrhenian sea: here there is a convergence between the sea breeze fronts that leads to an increment of wind speed and, then on the wind power.

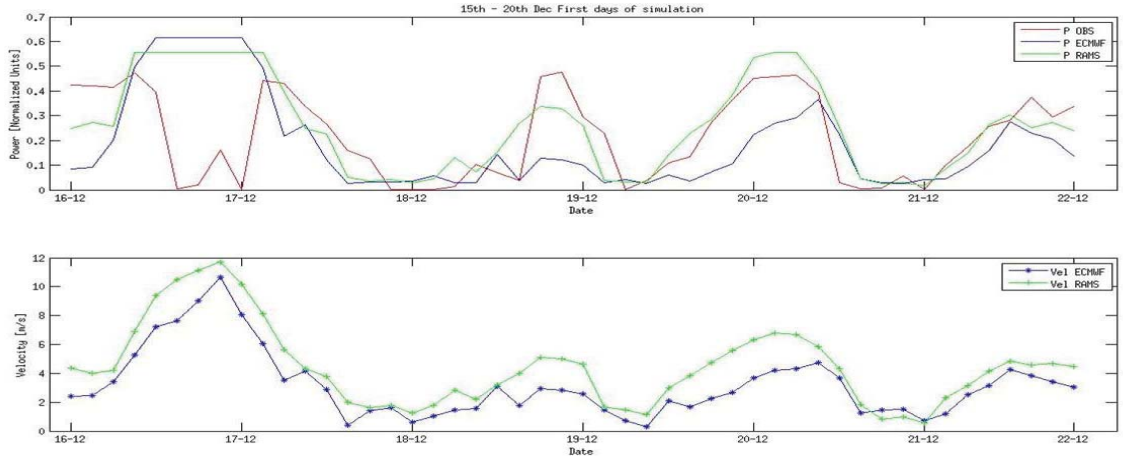

Figure 5.11: *Upper panel* Comparison between power predicted by RAMS (green), IFS (blue) and observation (red).*Bottom panel* Comparison between velocity predicted by RAMS (green) and IFS(blue).

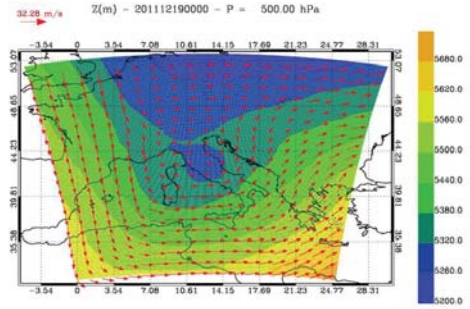

(a) For RAMS hindcast in the 19th December 2012 at 00 UTC there was a passage of a cyclone in central Italy

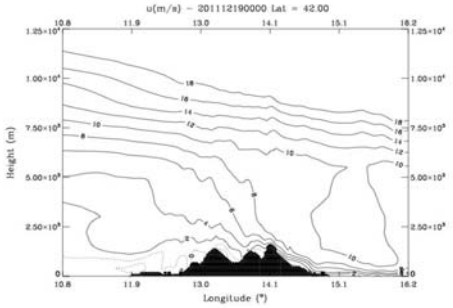

(b) Evolution of the velocity predicted by the model at different heights.

Figure 5.12: Comparison between RMSE and IFS

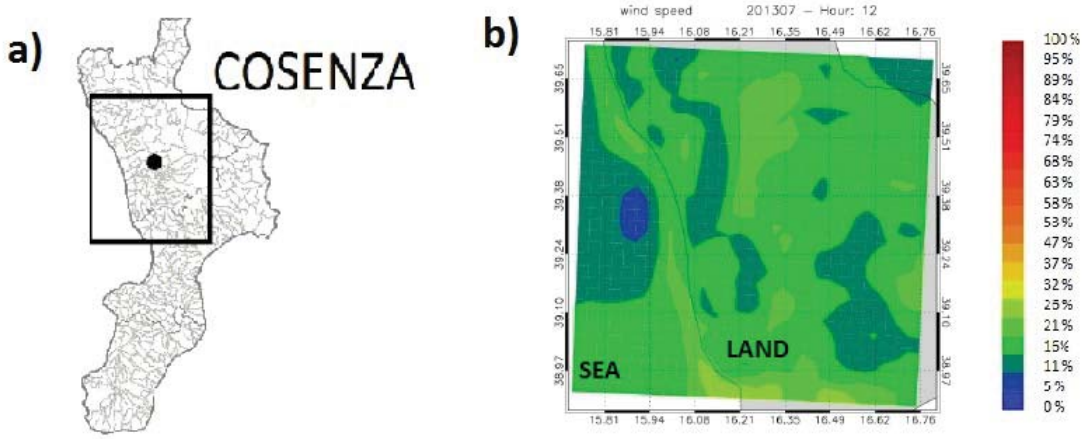

Figure 5.13: Calabrian zone where forecast is calculated (a) and example of velocity output by RAMS model (b).

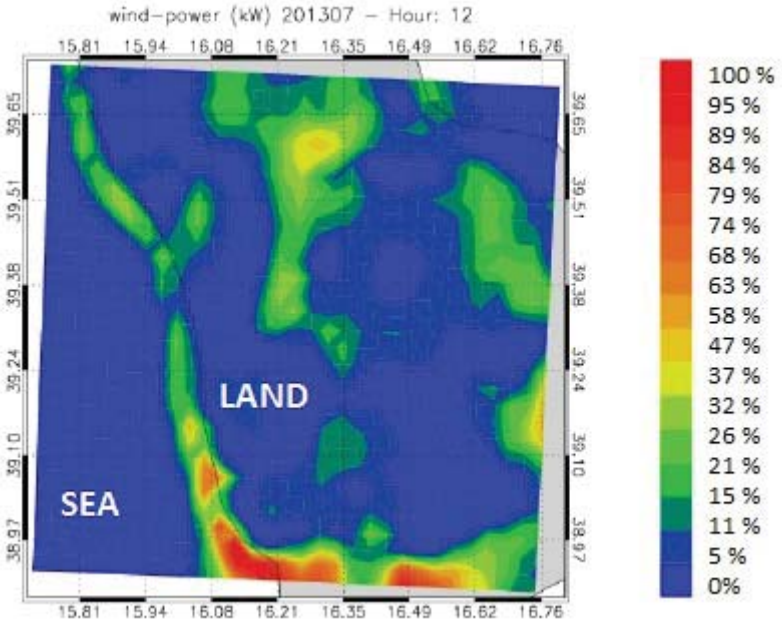

Figure 5.14: Example of calculated power by RAMS utilizing a power curve of a Vestas wind turbine.

Chapter 6

A study of wind behavior on Mediterranean basin

In this chapter we want to show another approach for the study of wind considering synoptic scale. In particular we focus our attention to analyze the behavior of extreme wind speed to characterize the Italian regions climate. To do this we developed a methodology that define the extreme wind speed for each area of interest and select zones with the same wind characteristics. Below the global circulation and the typical variables to analyze it are described; these variables are, then, calculated using a 30 years simulation of European Centre for Medium-Range Weather Forecasts (ECMWF) on a wide grid that include Italy. In this way it was possible to make a valuation of different climate zones,according to the different wind intensities and wind direction.
The study shown in this chapter is an application of the work made inside the nation project PON A300308 GELMINCAL - "Generatore Eolico a Levitazione Magnetica in Calabria", in collaboration with University of Reggio Calabria.

6.1 Global Circulation

The motion of atmospheric fluid could be divided in two wide classes, depending on the presence of irregular distribution of diabatic [1] heating in the atmosphere:

- motions driven both indirectly that directly from horizontal thermal gradients in the stratified stable atmosphere takes into account the 98% of the kinetic energy of weather. Almost all the kinetic energy is associated with fields of wind horizontal scales synoptic and planetary, which has a mean square error of the overall speed of

[1] Diabatic process: fast changing conditions inhibit the system to adapt the its configuration during the process, then the probability density remains unchanged. Typically there is not a eigenstate of final Hamiltonian with the same functional form as initial. Adiabatic process: gradually changing conditions allow the system to adapt its configuration, then the probability density changes during the process. If the system begins with an initial eigenstate of the Hamiltonian, it will end with the corresponding eigenstate of the final Hamiltonian.

about $17m/s$. Some of the small-scale motions observed in the atmosphere derive their energy from horizontal wind fields on a large scale.

- motions driven by convective instability take into account the rest of the kinetic energy remaining. Convection is continually broken into discrete regions of the atmosphere which results in a vertical gradient of adiabatic heating. The resulting motions have spatial scales ranging from 30 km in the storms larger than 1 mm in microscale motion within the surface layer. In spite of their small contribution to the kinetic energy atmospheric convective driven motions play an important role in the upward transport of sensible and latent heat.

From a dynamic point of view, the horizontal motions at large scale owe their existence to the force caused by the pressure gradient that drives a horizontal flow rate through the isobars from the highest to the lowest pressure. Due to the rotation of the Earth that flow through the isobars induces a movement parallel to the isobars which speeds tend toward a state of geostrophic balance with the horizontal pressure gradient.

6.2 The current map of the extreme winds

The existent map of extreme wind does not take account neither the previous consideration about global circulation nor the presence of the Apennines in the middle of Italy; this map was produced by Ballio et al Ballio [7] and uses statistical methods to analyze the extreme winds characteristic and divide Italy in different climatic zones.
In this work, data on intensity and direction on wind velocities are acquired from 42 stations of ITAV (Telecommunications and Flight Assistance Inspectorate) and from 27 stations of ENEL (Italian Electric Power Company). The first data are every three hours on a period of 10 years; the latter cover smaller period, but the frequency is better (10 minutes).
For each station the following parameters are considered: latitude, longitude, time interval of available data, the altitude above sea level, position classification of the station (airport, city centre, hilly zone, small island, littoral, mountainous area, plain promontory or isolated relief, valley). In order to ensure that a wind data base be correctly submitted to statistical analysis, it is necessary that same be representative, reliable and homogeneous. Defined as representative is a data base acquired over a sufficiently extended arc of time by an adequately located station; reliable is an error-less data base; homogeneous is a data base composed of values recorded under uniform conditions. The data for this study are judged to be representative in Ballio et al. [8],Ballio et al. [9] and Ballio et al. [10]. Utilizing then a correct database, it is possible to define a value v_c as the corrected velocity averaged on temporal range T and measured by an anemometer placed at height z in a point P of a territory Δ.

6.2.1 The two methods of the probabilistic analysis

Two alternative methods are used for the previous study, applied on a transformed and corrected databases: asymptotic analysis and process analysis. Process analysis guarantees solutions which are generally better than those given by asymptotic analysis Lagomarsino and Solari [45], but this is true only if the time interval interested is small: for bigger data set as that of ITAV calculations became harder and no improvement in the results.
For this reason the 42 ITAV stations are analyzed using asymptotic technique and the 27 ENEL stations by process analysis. The first technique regard use of Gumbel extreme values law to obtain the distribution function F_M of the maximum yearly value of the average wind speed, it is possible to obtain the distribution function F_M of the maximum yearly value of the average wind velocity using the Gumbel extreme values law (Gumbel [35]).
The process analysis considers the average wind speed as a stochastic stationary process and for this the distribution function F_M is related to a Possonian Gomes and Vickery [33]. The average wind velocity with mean return period $\overline{R}$ is deduced from the extreme distribution by setting $\overline{R} = 1/\left[1 - F_M(\nu)\right]$.

6.2.2 Zoning and wind map in Italy according Ballio et. al

Starting form the reference velocity processed, stations are divided into two classes: those at sea level and those at higher altitude. The stations of the first class are divided (Fig. 6.1) as a result of statistical studies on the values of v_{ref} (mean value, standard deviation and variance) in 5 geographical areas:

A) Valle d'Aosta, Piemonte, Lombardia, Veneto, Trentino Alto Adige, Friuli Venezia Giulia (except Trieste), Emilia Romagna;

B) Toscana, Umbria, Marche, Lazio, Abruzzo, Molise, Campania, Puglia, Basilicata, Calabria (except Reggio Calabria);

C) Provincia di Reggio Calabria, Sicilia and Sardegna;

D) Liguria;

E) Trieste and islands (except Sicilia and Sardegna).

6.2.3 Return criterion for mean wind profile

Return criterion was used to evaluate the mean wind profile: this method estimates velocities v^e_{ref}, where z is the height and e exposition category, considering reference speed v_{ref}, roughness factor z_0, topography c_t and terrain factor k_r:

$$v^e_{ref}(z) = v_{ref} c_t k_r \ln \frac{z}{z_0} \tag{6.1}$$

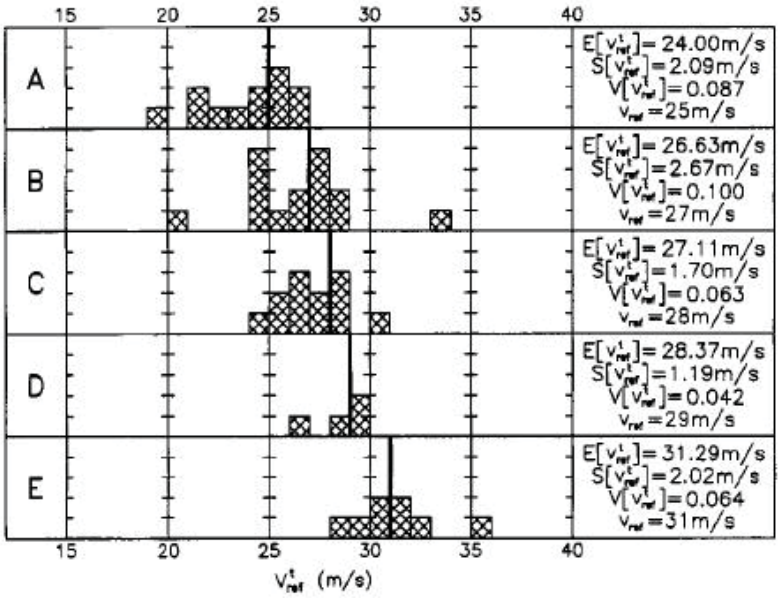

Figure 6.1: Subdivisions of the first class stations.

This equation was applied for all the nine identified zones and for all the heights with $z > z_{min}$, where z_{min} is the minimum reference height (AA. [3]). Five expositions category are defined to utilize this method: local roughness, geographic position, distance from coast, altitude and prevalent direction of extreme winds.

Fig. 6.2 shows the results of attribution criterion for the studied sites: this classification is similar also for other european countries AA. [3].

Vantages of this analysis are in the balance attribution of the dependency of categoriza-

tion by sea distance and by altitude. Considering these variable, Italy was subdivided in 9 zones, determinate by a well defined set of characteristic variables. An other evident advantage of this study is the wide availability of data on land, coming form a sensor web with sufficient spatial dislocation and relative to time periods.

A problem of this zoning, mostly of a physical nature, is instead related to lack of considering the origin of synoptic perturbation that guide the development of extreme events and the climatology of the wind. Refinements to this technique can be performed, trying to consider how the Apennines, and physiographic features in general, affect the distribution of extreme winds. In Fig. 6.1, and in particular in zone 3, in fact, the Ionian and Tyrrhenian windy areas are treated as homogeneous; there are numerous studies (a specific example in southern Italy is the work of De Leo et al. [21]) that identify the two areas as climatically different. On the other hand, the zoning must be studied in function of the disturbances and their origin: Atlantic disturbances impacting Italy in a completely different way than the Arctic or Siberian affecting more islands than in the north of the peninsula.

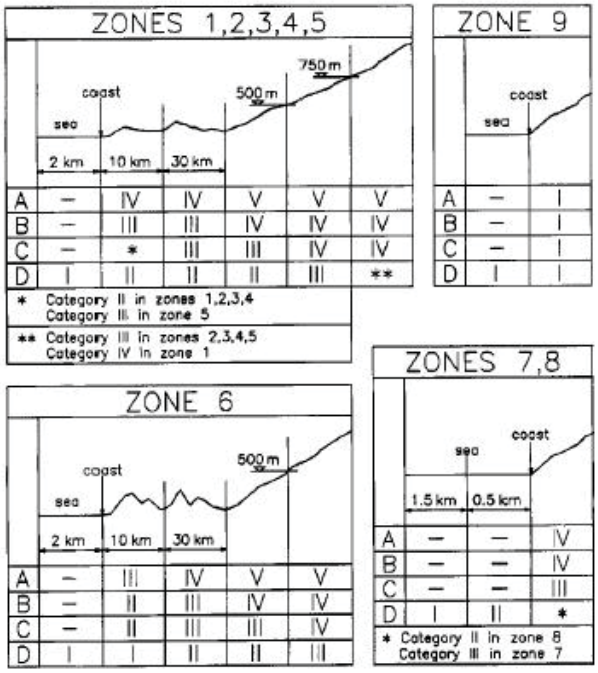

Figure 6.2: Exposition categories.

6.3 The improvement with model simulation

The assumption, in the creation of new maps of wind, is that the extremes are caused by perturbation coming from the Atlantic, Arctic and Siberian zones and located, principally, in the central basin of the Mediterranean. The detection of maximum wind, in off-shore locations, provides useful indications of the impact on the ground of such events(Zhong and Takle [77],Mora [53], Mellouki and Ravishankara [50]).
The start point of this study is the location of the maximum events that characterize the largest possible period: to identify this period we used data modeled from from ECMWF. The scale resolution of the model is 15 km for data that cover a period from the 1st January 1975 to 31th December 2004 (30 years).
ECMWF makes significant contributions to support research on climate variability: an innovative approach has pioneered, known as reanalysis, which involves feeding weather observations collected over decades into a NWP system to recreate past atmospheric, sea- and land-surface conditions over specific time periods to obtain a clearer picture of how the climate has changed. Reanalysis provides a most comprehensive and accurate four-dimensional picture of our atmosphere and effectively allows monitoring of the variability and change of global climate, thereby contributing also to the understanding and attribution of climate change. The ERA is a project of the ECMWF reanalysis meteorological data from previous simulations forecast of a global nature. The first product reanalysis, ERA-15 reanalysis generated for about 15 years, from December 1978 to February 1994 The second product, ERA–40 (originally intended as a re-analysis of 40 years) began in

1957 (the Geophysical Year International) and covers 45 years until 2002, as a precursor to a product reanalysis extended revised to replace ERA–40, ECMWF ERA–Interim recently released, covering the period from 1979 to the present.
For this study ECMWF ERA–INTERIM data set is used and verified using observed data from meteo stations of Ustica and Lampedusa (Italian Air Force) and Venezia (CNR–ISMAR, Acqua Alta).

The ECMWF data set acquired is used to drive analysis towards the extreme events. The methodology here shown considers both the statistical tools used by Ballio, 1999 (Ballio [7]) and the two physical motions considerate in Subsection 6.1. Then the analysis start considering the causes that origins extreme disturbances, and, to do this, extremes from RAMS simulation have been singled out. For each 30 events wind velocity and directions have been studied considering 3 days evolution time of the perturbation, using the distribution of wind probability density. How it is possible to seen in Fig.s 6.3

it is not correct to describe the sample with a single distribution. For example in Fig. 6.3b it is particular evident that there are at least 4 contributions: the different distributions indicate different wind regimes affecting different areas. In the bottom panels of 6.3, where only velocities up to $10m/s$ are isolated, there is just one event that evolves over time and interest different areas: the perturbation originates in the Atlantic Ocean and breaks into the Mediterranean through the Strait of Gibraltar. From here, due to a low pressure center located in Africa, tends to trigger high speed in the channel of Sardinia and in the proximity of Sicily, presenting a peak speed exceeding 20 m/s at 06 : 00, in the vicinity of coast of Sardinia, where the extreme has been singled out. It is important to note that all the velocities up to 10 m/s are recorded off-shore: in land orography and roughness are responsible for a large decrease of velocities.

6.3.1 Threshold wind velocity

In the previous section, velocities are filtered up to an arbitrary speed ($10m/s$), just to explain better the evolution of perturbation: now we define the threshold velocity as the peak of the last distribution (towards the highest speeds) that describes the probability density.
Usually the velocity distribution of wind velocities are described by a Weibull statistical distribution (Justus et al. [41], Seguro and Lambert [60]), that it expresses the dependency by velocity v throw two parameter: a (in unit of m/s) is the scale factor which is closely related the wind speed for the location, and b is the dimensionless shape factor which describes the form and width of the distribution.

$$f(x) = \frac{a}{b}\left(\frac{x}{b}\right)^{(b-1)} \exp -1\left(\frac{x}{a}\right)^{b} \tag{6.2}$$

Fig. 6.4 shown a fit of probability density function of modeled velocities in Ustica for 1989 using a Weibull distribution: this distribution well fit all the the data.

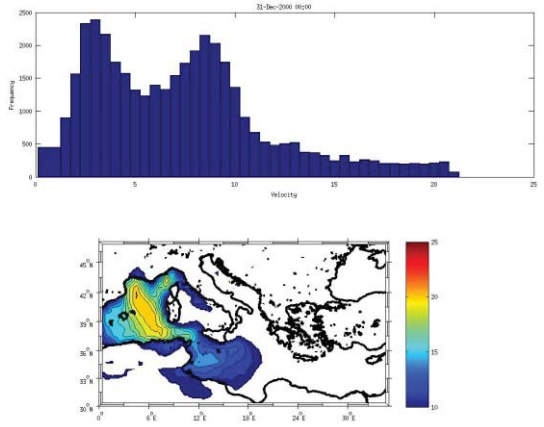

(a) 00 : 00

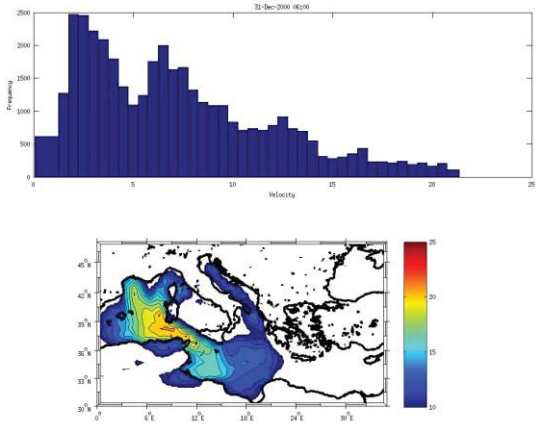

(b) 06 : 00

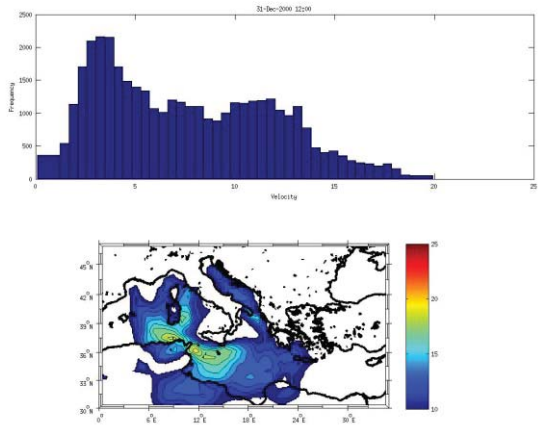

(c) 12 : 00

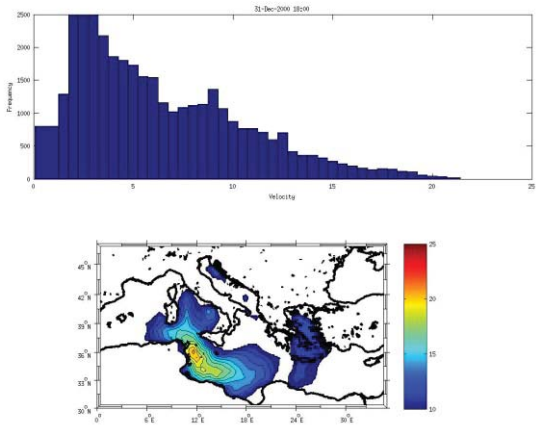

(d) 18 : 00

Figure 6.3: Atmospheric disturbances which affected the Mediterranean area during the 31th December 2000 analyzed using the ECMWF reanalysis. The graphs places in the high parts of each panel show the occurrence frequency for each speed (bin of $0.5m/s$): in the lower portions of the panels shows the maps of a speed above $10m/s$. Clockwise provides the following hours: 00 : 00, 06 : 00 (maximum speed), 12 : 00 and 18 : 00.

Then, considering the Weibull distribution, a little group of velocities are selected from then and defined as "extreme" following the definition of Intergovernmental Panel on Climate Change (IPCC IPCC [39]):

> *An extreme weather event is an event "rare" in reference to its statistical distribution. The definition of "rare" vary, but it is usually understood as less then a tenth percentile or more then ninetieth percentile of the mother distribution.*

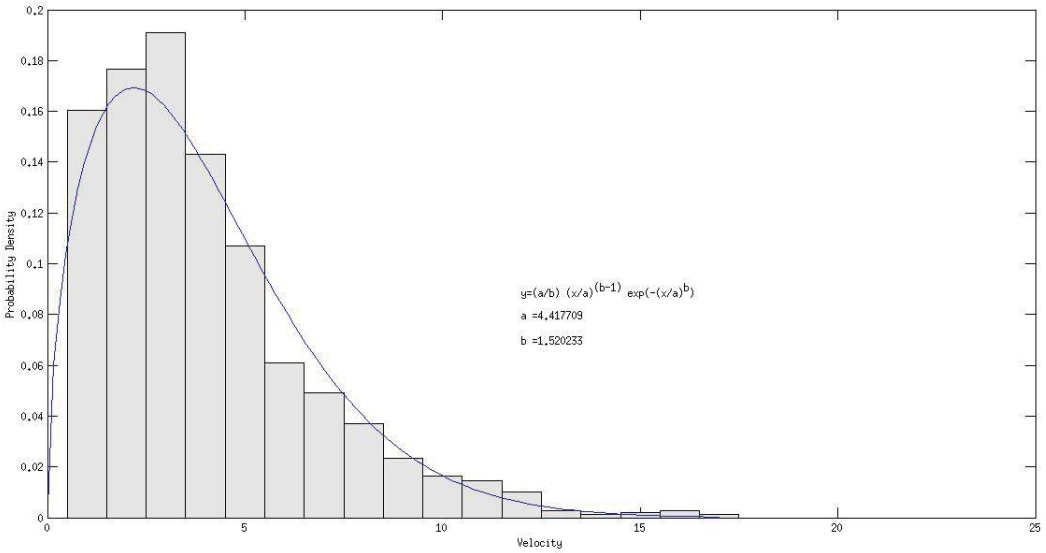

Figure 6.4: Probability density of velocity in Ustica for 1989 (gray bars) and its relative Weibull fit (blue line).

Utilizing extreme three methods are used to simulate their probability density

- Gumbel distribution
- Weibull distribution
- logarithmic function

This study was applied to case of figure 6.4 obtaining figure 6.5: here it is important to note that, even if the logarithmic fit seems to reproduce better the peak of the velocity distribution, at the tail of highest velocities (Fig 6.6) all the distributions underestimate the frequencies. All of this distributions show the same error respect the data: analogous considerations are obtainable considering the other 30 maximum events singled out for all data set. The conclusion is that it is not possible to describe extreme frequency with a single theoretical distribution (Weibull, Gumbel or logarithimics distributions). This is because, in the single instant in time, it is conceivable that a disturbance is occurring more frequently involves high speed in a very specific area of the region of interest. Considering, therefore, the peak of the theoretical distribution which incorporates the most number of high speed it is possible to define, in effect, a filter (threshold velocity) to follow the effects caused by the perturbation on the interested area.

All the threshold velocity are reported, for each year, in 6.1

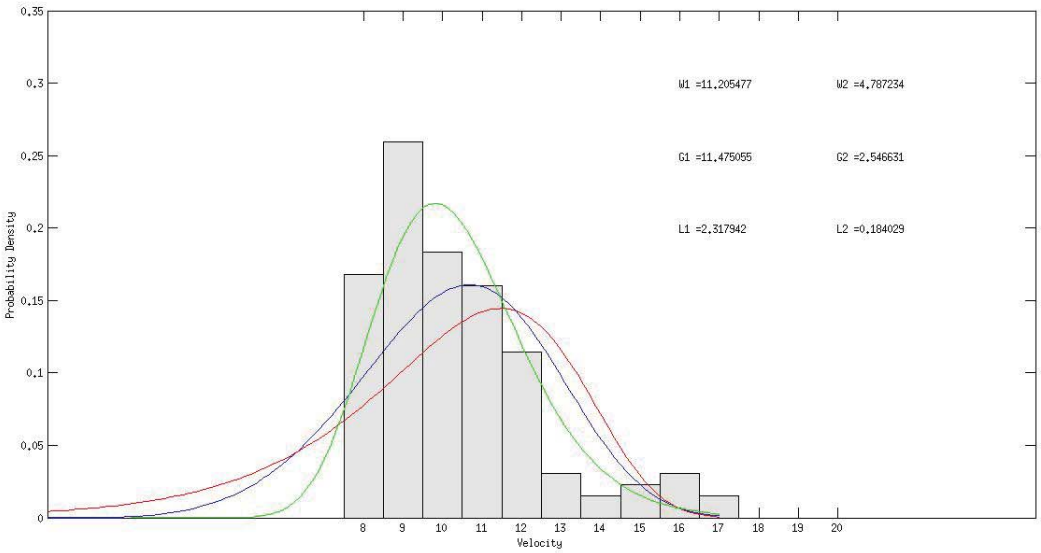

Figure 6.5: Probability density of velocity for 1989 in Ustica (gray bars). Blue line represents fit according to the Weibull (coefficients W1 and W2), red line is respect Gumbel (G1 and G2), and green line according to a logarithmic distribution (L1 and L2).

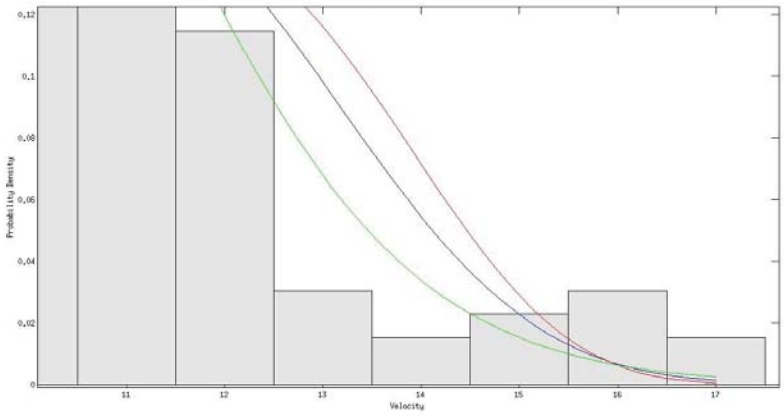

Figure 6.6: Zoom of previous figure. Logarithmic (green line) and Weibull fit (blue line) underestimate more data respect the Gumbel fit (red line).

6.4 Identification and analysis of extreme winds

In order to follow the above procedure for the identification of areas most affected by extremes wind, maps that consider the average of the 30 extreme events previously selected have been made. To compare the modeled data with the previous work of extreme winds zoning (Ballio [7]) only the wind behavior in-land is shown.
As is to be expected, and also based on the results obtained, the maximum speeds recorded in the whole domain in positions off-shore, or at least, outside the territorial boundaries Italian. This implies that the speed in-land are, of course, much lower than those identified around the maximum. For this reason critical speed in-land necessities of a redefinition: it has been set equal to half of the critical speed on average 30 events.
Clearly this reduction does not change the physical interpretation of the events, but it does make it more readable and easy to interpret the maps produced. In fact, possible sources of mesoscale disturbances include instabilities that occur intrinsically on the mesoscale, forcing by thermal or topographic sources, nonlinear transfer of energy from either macroscale or microscale motions, and interaction of cloud physical and dynamical processes (Holton [36]). The Fig. 6.7 shows the average speed on 30 extremes identified only when it exceeds a threshold value redefined and equal to half of the average value of the speed threshold. Respect to Figure 75, this map hows more clearly the areas affected by extreme winds. Here it is important to note that, in particular, Sardinia and Sicily are frequently involved by disturbances. The Tyrrhenian coast of Tuscany, in central and southern Italy appear affected by winds often even higher than 10 m/s.
Mountains waves created by flow over individual peaks are generally regarded as small-scale phenomena. But flow over large mountain ranges can produce orographic disturbance in the 10-100 km mesoscale range, and, then, it could be provided by the model. Under some conditions of mean flow and static stability flow over mountain rages, such as the southern Apennines, can lead to strong down-slope wind storm. The Puglia region of the lower Adriatic, on the other hand, are often affected by sustained winds, especially (as we shall see) for current North East.
To study the origins of extreme events, all of them are classified according to the wind directions: Figures 6.8, 6.9, 6.10 and 6.11 show the wind speed and related areas.
These four maps are those that identify the areas of the Italian Peninsula affected by winds higher than average, and can be associated with significant disruption and creating extreme winds.
When the winds (extremes) are directed to the NE (Figure 6.8), which is seen as being the main direction for the occurrence of the maximum annual rate, we see that the areas affected by sustained winds are Puglia and Emilia Romagna on the Adriatic coast, and a large portion of the Tyrrhenian side of the peninsula (except Calabria and Sicily), in areas directly descendants of the Apennine Mountains. This observation is surprising at first sight, since they seem interested in many areas not directly exposed to the current north-east; in fact, as mentioned previously, this situation is related to the fact that the currents from the NE, undergo an acceleration in the descending phase the Apennines, reaching the speed values reported. The area at relatively higher in the regions sub-central

and northern Apennines. When the winds come from the extreme SE (Figure 6.9), Puglia and small areas of Calabria on Ionian side are the only areas affected by winds higher than average. In Calabria areas these disturbances usually carries on violent thunderstorm: the water vapor exchanging between the sea and overlaying air masses, which travel a long fetch over the Ionian Sea, is an important physical factor that causes these storms (Federico et al. [27], Petrucci and Polemio [57]).
When the winds are from SW (Figure 6.10), appearing mainly affected some parts of Sicily and most areas in central and southern Italy (high Tyrrhenian coast and inland areas, Basilicata, Campania to the central areas of the Lazio).
When the currents are from NO (Figure 6.11), management often though not always affected by extreme winds (as seen above), the regions suffering from the effects of currents are only Sardinia and Sicily.
It is interesting to note that in most regions, especially central and southern extreme winds are associated with a defined direction of origin. This classification allows to identify the potentially most significant wind regimes, and to understand the circumstances in which the disturbances that generate extreme winds may involve, and how, the areas of the Peninsula.

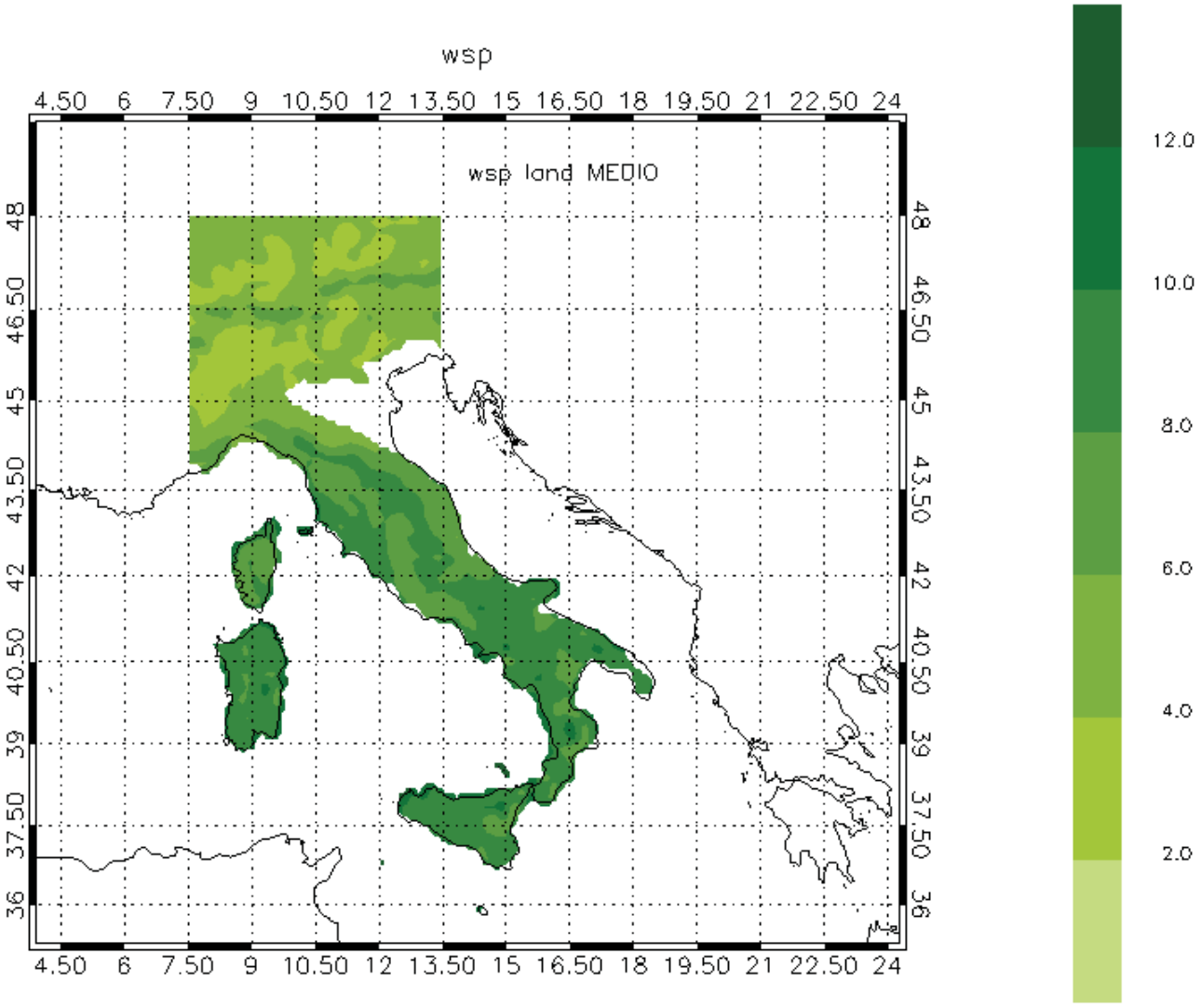

Figure 6.7: Average speed simulated in-land for only 30 ends identified.

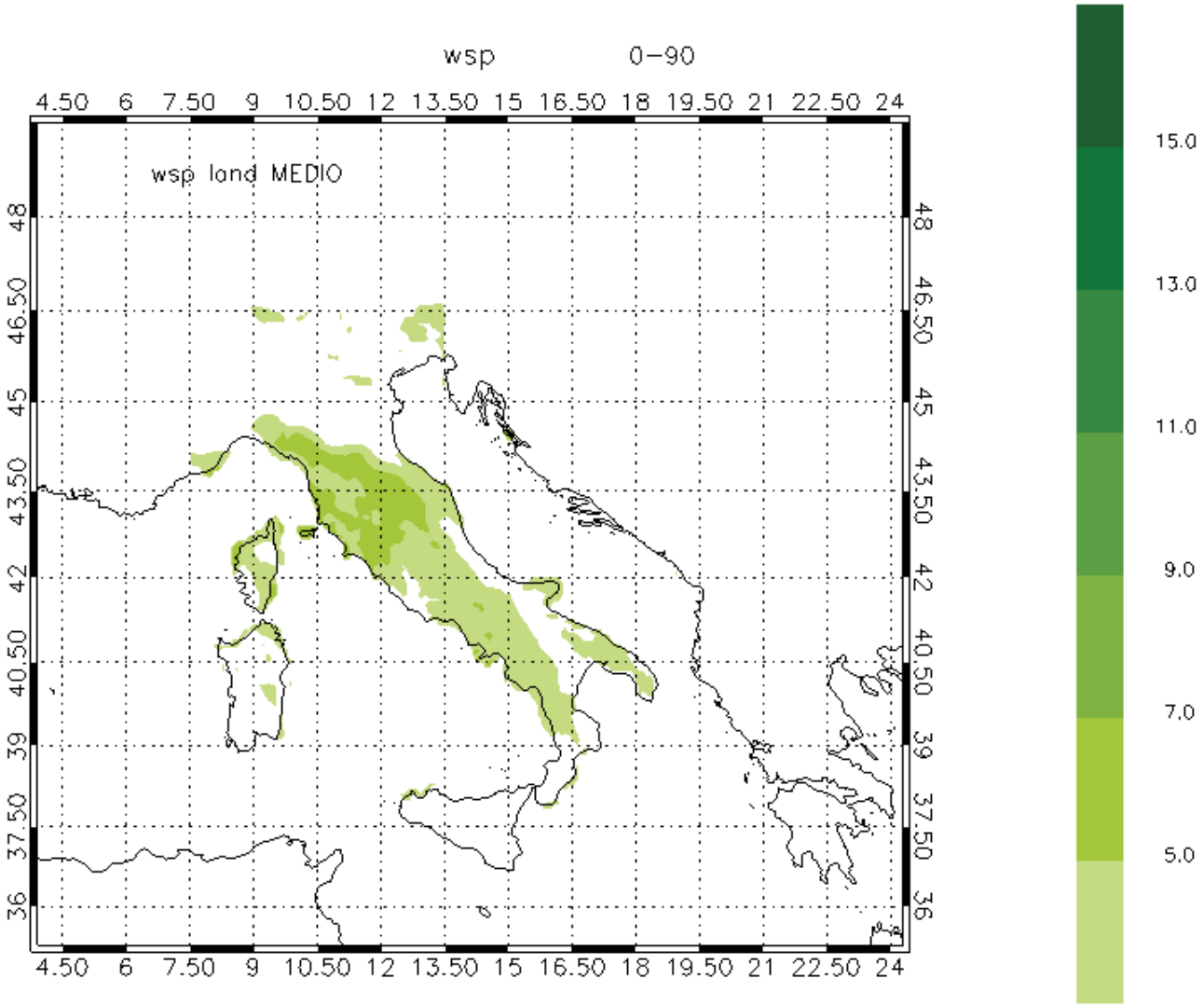

Figure 6.8: Average speed simulated in-land for only 30 ends identified, selected for wind direction on sector $0 - 90\circ$.

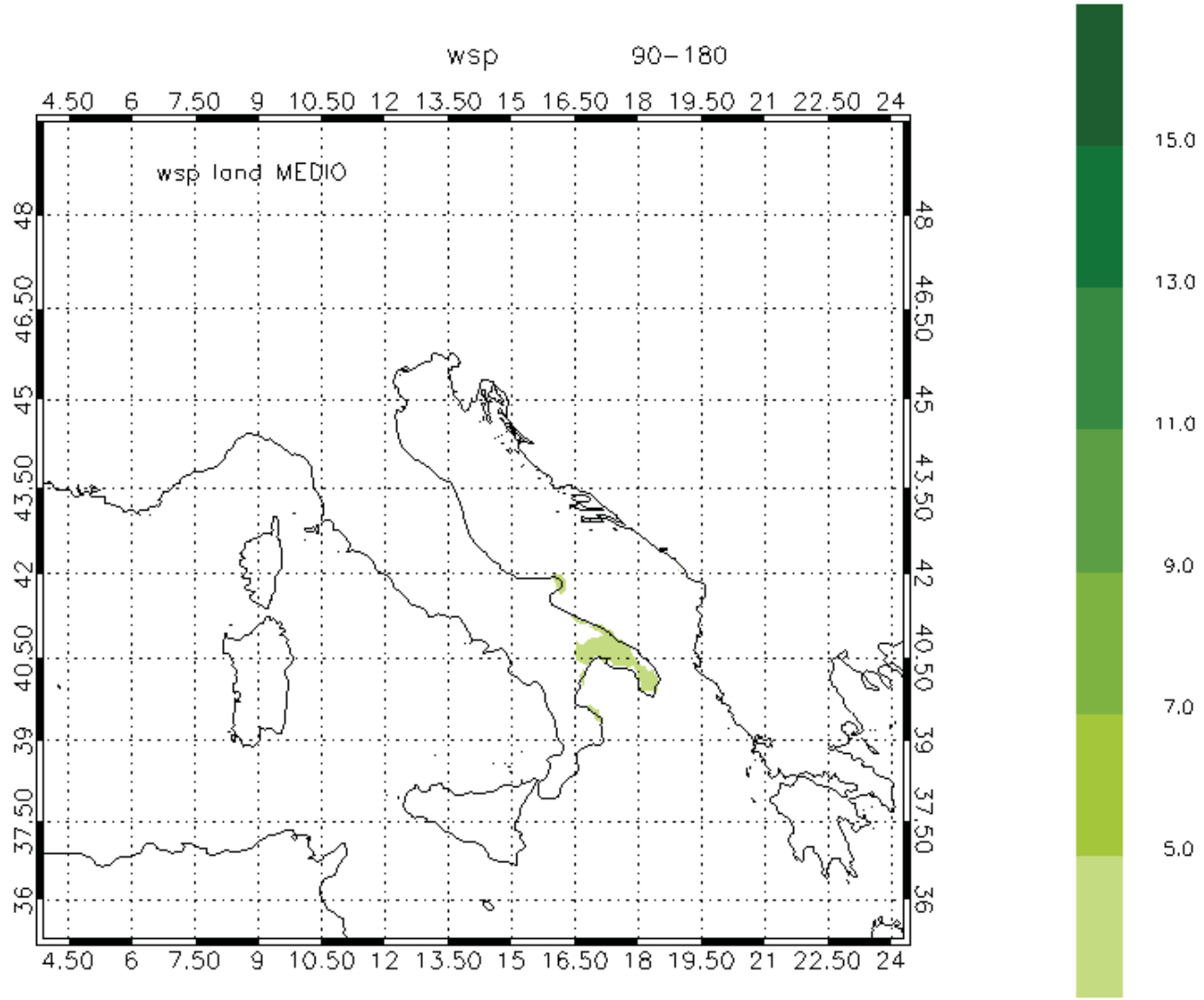

Figure 6.9: Average speed simulated in-land for only 30 ends identified, selected for wind direction on sector $90 - 180\circ$.

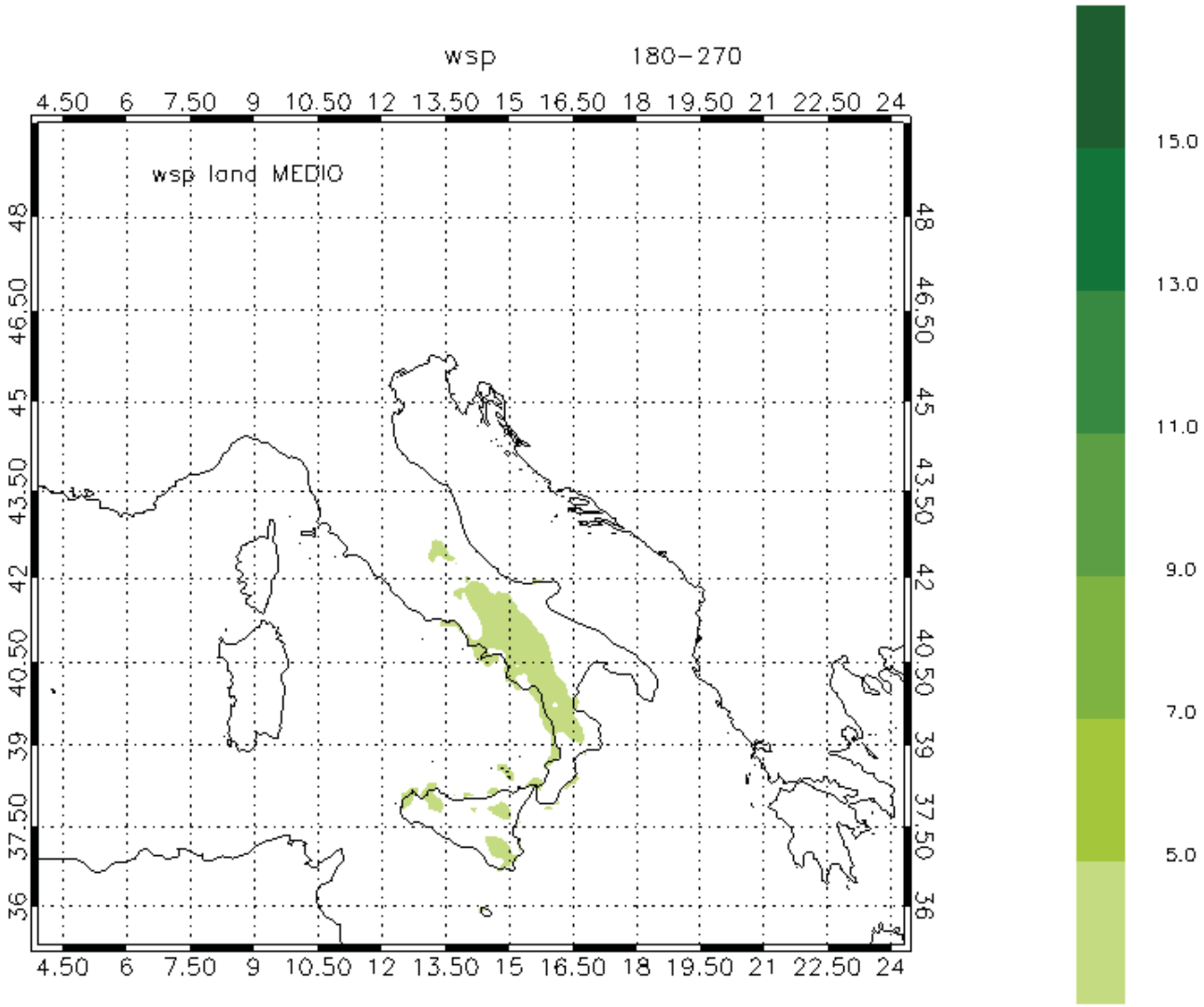

Figure 6.10: Average speed simulated in-land for only 30 ends identified, selected for wind direction on sector $180 - 270\circ$.

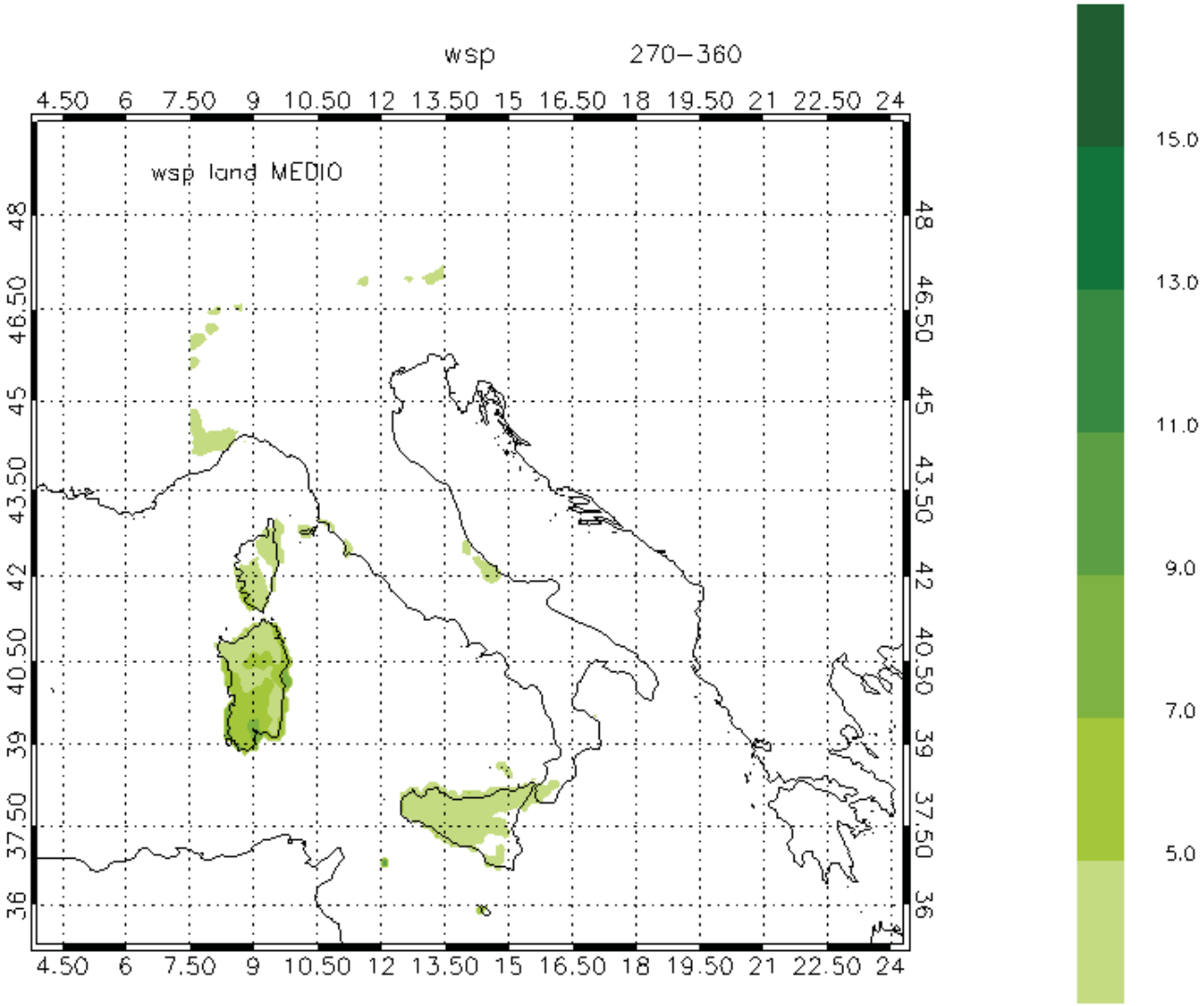

Figure 6.11: Average speed simulated in-land for only 30 ends identified, selected for wind direction on sector $270 - 360\circ$.

Table 6.1: Threshold velocities for each maximum events.

Date	$v_{threshold}$ $[m/s]$
1975/11/18 09:00	15.7
1976/12/02 12:00	18.6
1977/12/11 18:00	11.9
1978/11/28 18:00	14.0
1979/12/31 15:00	22.2
1980/01/15 12:00	19.0
1981/01/21 09:00	24.0
1982/03/23 06:00	13.4
1983/12/02 15:00	16.0
1984/02/10 12:00	17.2
1985/01/17 00:00	18.0
1986/02/01 00:00	18.0
1987/11/24 21:00	15.1
1988/01/31 21:00	17.8
1989/02/26 03:00	17.8
1990/02/27 15:00	10.7
1991/12/20 15:00	15.8
1992/03/26 15:00	19.5
1993/11/26 21:00	14.2
1994/04/05 12:00	18.2
1995/03/13 18:00	16.6
1996/12/01 18:00	11.6
1997/02/28 03:00	14.5
1998/03/25 21:00	16.8
1999/12/28 09:00	22.6
2000/12/31 06:00	18.2
2001/11/11 03:00	16.2
2002/03/11 03:00	12.9
2003/03/17 06:00	16.1
2004/11/14 12:00	16.7

Chapter 7

Conclusion

7.1 Results

A study on three different scales of wind phenomenology (turbulent, medium and climate) was made using different techniques and physical principles. All of them finalized to wind energy applications: if we consider, for example, a feasibility study of a wind turbine, it is necessary to consider perturbations induced by the different types of terrain, the wind changes in magnitude and direction throughout the year and turbulence arising from the interaction between the air masses and the various obstacles or other turbines nearby. The determination of the power curve, in fact, on the site flat or complex terrain, can lead to different results on the performance of the wind turbine, even though it is exposed to the same wind conditions due to the effects of climate and turbulence.
Here below the key characteristic of wind behavior are summarized for each considered scale.

7.1.1 Turbulence

The third–order structure function F_3 satisfy Yaglom's law: in fact using this function it was possible to find a particular ranges scale in every stability conditions. The Yaglom's law express the same results of Kolmogorov law, but it is obtained considering magnetic fluid equations dynamics. This conclusion, in according to the theory of homogeneous and isotropic turbulence, reveals that, also in case far from standard assumptions as in a stratified flow, a general approach throw Yaglom's law is correct. In addition to this, the result of application of Yaglom's law defines the inertial range for atmospheric turbulence, located in the range of scales from some few centimeters up to a fraction of meters, regardless the stability condition and wind regime Chap. 3.8. In principle, then, this study verifies that the same law is more universal than expected by calculation from Navier–Stokes equations: it, in fact, could describe atmospheric situation rather than space turbulence or the behavior of a plasmas in a laboratory (for further information about this please refer to Bruno and Carbone [13], Sorriso-Valvo et al. [64], Forman and Burlaga [30]).
An important application of Yaglom's law is inside the possibility to measure the turbulent

energy injection rate ϵ and to refer it to energy source of the system. In fact, during stable and neutral situations, ϵ is more or less two time smaller than unstable situations.
As the energy system increases also the loss of energy from one eddy to another increases: this means that the wind signal is more intermittent, and it was verified studying the probability density functions (Fig. 3.5) and kurtosis (Fig. 3.7). It is worth noting that scaling exponents obtained in laboratory wind tunnel under controlled situation result to be higher than we found for $n > 3$. This is similar to what is observed in near–wall turbulence in laboratory fluid flows, that intermittency increases going towards the wall due to the presence of strong turbulent structures.
This could causes problems, for example at wind turbine: a wind velocity intermittent signal introduced in a power grid becomes a wind power signal even more intermittent (Milan et al. [51]). To integrate wind power in a electrical grid and respond to energy needs, the sudden variation of wind power need to be properly accounted for in to order to maintain power stability in future grids.

7.1.2 Medium Scales

To give a correct prediction of wind behavior in this study two methods are defined: a foreseen with semi-empirical law, that provide a near real time prediction of wind profile starting from data measured at the surface; a weather forecast system that use data from large scale (obtained by global model) to predict wind velocities and other atmospheric quantities.
In first case prediction on wind and turbulence profiles until 150 m are estimated and compared with data from Wind Lidar installed at CNR-ISAC UOS (Italian National Research Council (CNR) - Institute of Atmospheric Sciences and Climate (ISAC), operational unit support) of Lamezia Terme (CZ). Starting with few parameters measured on soil, it was possible reproduce wind characteristics also in upper heights. Data simulated considering atmospheric stability (similarity method, Fig. 4.10) show a smaller error respect a simple power law (Fig. 4.11): this conclusion reveals the necessity to consider both wind regime that stability conditions to estimate wind behavior on planetary boundary layer.
In the second method the performance of a forecasting system, based on the Regional Atmospheric Model System (RAMS) model and operational at ISAC-CNR, is shown: the application focus over South Italy where the horizontal resolution of the model grid is 3 km. This forecast is an upgrade of the operational setting already available in southern Italy [Federico et al. [27]].
Results show that root mean square error (RMSE) is 2-3 K is 2.0-2.8 m/s for wind speed and $55 - 75°$ for wind direction, depending on forecasting time and season. The RMSE for different parameters shows a clear diurnal cycle, especially in summer. For example the RMSE for temperature in summer is 2 K during the night, while it increases up to 3.2 K during the day. The increase of the RMSE with forecasting time is of the order of 10% of the initial RMSE for all parameters.
All the forecasts are corrected with a a-posteriori correction technique on the forecast error, named Model Output Statistics (MOS). The MOS technique coupled by correct choice on

horizontal resolution is an effective way to improve the model performance at specific location. This point is particularly important for the application of quantitative forecast: the comparison with wind Lidar data (Fig. 4.14) shows that the MOS application reduces the model error for all parameters. In particular, depending on forecasting time, the RMSE reduction is between 10 and 20 % for wind speed and 0, and between 0 and 10% for wind reduction. The MOS reduction permits reduction of BIAS and then to compare directly the physics hypothesis with observation. In this way it was possible to compare wind velocity estimates with wind Lidar observations (Fig. 5.7) and produce an application on wind power forecast in a region of central Italy (Fig. 5.9). In both cases the observations are good reproduced, but there are some interesting point to study in deep. Comparing with wind profiles, effects caused by low level jets are not reproduced (Fig. 4.9): this phenomenon is caused by particular orography of the territory where wind Lidar are placed. On the other hand in the forecast of wind power energy (Fig. 5.11), improvements on correct modeled power curve could be obtained considering the single wind profile and power output for each wind turbine.

7.1.3 Study on extreme events on 30 years data

The structure of the climatological wind data from ECMWF and a further cataloging of extreme events are been given.
The influence of orography on the cyclonic systems development has been confirmed, and in this regard it would be desirable to have a higher resolution grid data for the study of such systems in the Mediterranean.
Depending on wind directions, preferential areas of maximum disturbance development have been identified. A different approach respect the actual Italian wind map Ballio [7]]has been developed: in the previous work, in fact, many observed data are collected for 10 years from station homogeneously distributed on Italian territory, meanwhile in our study model simulation for a period of 30 years are analyzed. The two approaches are not comparable, but both pf them reveals the necessity to combine all possible data to aggregate information on the single observation point to a more complex situation of disturbance generation on large scale.

The aim of this thesis is to show the complexity and the heterogeneity of the techniques needed to use to understand the wind behavior. In particular, considerations on all scales are necessary to apply his characteristics to practical applications. An example is the wind energy. The first step of the feasibility study, for installing a wind farm within an area, needs the estimate of the potential energy availability. This is done by mapping the wind climate in the region in terms of sector-wise mean wind speed and direction and sectoral Weibull probability distribution function. Anyway results and methodology of this study could be applied at every field concerning by wind variability.

Bibliography

[1] http://www.gillinstruments.com, .

[2] http://www.vestas.com, .

[3] VV. AA. Eurocode 1: Basis of design and actions on structures, part 2-4: Wind actions. *European Committee for Standardization*, 1994.

[4] E. Anahua, S. Barth, and J. Peinke. Markovian power curves for wind turbines. *Wind Energy*, pages 11, 219, 2008.

[5] E. Avolio and al. Comparison of wind climatology from dynamical downscaling with other methodologies. *Proceeding at EWEC 2012*, 2012.

[6] Stull R. B. An introduction to boundary layer meteorology. *Journal of Fluid Mechanics*, 224, 1991. doi: 10.1017/S0022112091211921.

[7] G. Ballio. Probabilistic analysis of italian extreme winds: Reference velocity and return criterion. *Wind and Structures*, pages 51–68, 1999.

[8] G. Ballio, S. Lagomarsino, G. Piccardo, and G. Solari. A first step towards the map of the italian extreme winds. part 1: General principles and analysis methodology. *Costruzioni Metalliche, ACS-ACAI Servizi Srl Milano*, pages 147–172, 1991.

[9] G. Ballio, S. Lagomarsino, G. Piccardo, and G. Solari. A first step towards the map of the italian extreme winds. part 2: Results, repercussion on standards, design implications. *Costruzioni Metalliche, ACS-ACAI Servizi Srl Milano*, pages 209–242, 1991.

[10] G. Ballio, S. Lagomarsino, G. Piccardo, and G. Solari. A new map of italian extreme winds. *Giornale del Genio Civile*, 1994.

[11] R.G. Barry and R.J. Chorley. *Atmosphere, Weather, and Climate*. Routledge, 1992. ISBN 9780415077613. URL `http://books.google.it/books?id=EsQ9AAAAIAAJ`.

[12] E Batchvarova and S. E. Gryning. Applied model for the growth of the daytime mixed layer. *Boundary-layer Meteor.*, pages 261–274.

[13] Roberto Bruno and Vincenzo Carbone. The solar wind as a turbulence laboratory. *Living Reviews in Solar Physics*, 2:4, 2005.

[14] V Carbone, R Marino, L Sorriso-Valvo, A Noullez, and R Bruno. Scaling laws of turbulence and heating of fast solar wind: the role of density fluctuations. *Physical review letters*, 103(6):061102, 2009.

[15] D.J. Carruthers, R.J. Holroyd, J.R.C Hunt, W.S. Weng, A.G. Robins, D.D. Apsley, Smith F.B., D.J. Thomson, and B. Hudson. Uk atmospheric dispersion modeling system. *Proceedings of the 19th NATO/CSSM Int. Techn. Meeting on Air Pollution Modeling and its Application, Ierapetra, Greece*, 1991.

[16] G. M. Carter, J. P. Dallavalle, and H. R. Glahn. Statistical forecasts based on the national meteorological centerś numerical weather prediction system. *Weather Forecasting*, pages 401–412, 1989.

[17] B. Castaing, Y. Gagne, and E. J. Hopfinger. Velocity probability density functions of high Reynolds number turbulence. *Physica D-nonlinear Phenomena*, 46:177–200, 1990. doi: 10.1016/0167-2789(90)90035-N.

[18] S. Chandrasekhar. An introduction to the study of stellar structure. *New Yorker:Dover*, pages 82–84, 1967.

[19] C. Chen and W. R. Cotton. A one-dimensional simulation of the stratocumulus-capped mixed layer. *The Boundary Layer Meteorology*, pages 289–321, 1983.

[20] W. R. Cotton, R. A. Sr. Pielke, R. L. Walko, D.E. Lista, C. J. Tremback, H. Jiang, R. L. McAnelly, J. Y. Harrington, M. E. Nicholls, G. G. Carrio, and J. P. McFadden. Rams 2001: Current status and future directions. *Meteorol. Atmos. Phys.*, pages 5–29, 2003.

[21] L. De Leo, S. Federico, A. Sempreviva, L. Pasqualoni, and E. Avolio. Study of the development of the sea breeze and its micro-scale. *14th International Symposium for the Advancement of Boundary Layer Remote Sensing*, 2008.

[22] J. W. Deardoff. Parametrization of the planetary boundary layer for use in general circulation models. *Mon. Weather Rev.*, pages 93–106, 1972.

[23] S. Federico. Verification of surface minimum, mean, and maximum temperature forecasts in calabria for summer 2008. *Natural Hazards and Earth System Sciences*, pages 487–500, 2011.

[24] S. Federico, E. Avolio, C. Bellecci, and M. Colacino. On the performance of a limited area model for quantitative precipation forecast over calabria. *Il Nuovo Cimento C*, pages 663–676, 2003.

[25] S. Federico, C. Bellecci, and M. Colacino. The precipitation field over calabria: large scale correlations. *Il nuovo Cimento C*, pages 553–567, 2003.

[26] S. Federico, E. Avolio, C. Bellecci, and M. Colacino. The meteorological model rams at crati scrl. *Advances in Geosciences*, pages 177–180, 2005.

[27] S. Federico, E Avolio, L. Pasqualoni, and C. Bellecci. Atmospheric patterns for heavy rain events in calabria. *Natural Hazards and Earth System Sciences (NHESS) and Discussions (NHESSD)*, pages 1173–1186, 2008.

[28] S. Federico, L. Pasqualoni, A. M. Sempreviva, L. De Leo, E. Avolio, C. R. Calidonna, and C. Bellecci. The seasonal characteristics of the breeze circulation at a coastal mediterranean site in south italy. *Adv. Sci. Res.*, pages 47–56, 2010.

[29] R. Ferretti, G. Mastrantonio, S. Argentini, R. Santoleri, and A. Viola. A model-aided investigation of winter thermally driven circulation on the italian tyrrhenian coast: A case study. *Journal of Geophysical Research*, page 4777, 2003.

[30] M.A. Forman and L. F. Burlaga. in the solar wind at l1 in june 2000, in solar wind ten, (eds.) velli, m., bruno,r., malara, f., proceedings of the tenth international solar wind conference, pisa, italy, 17-21 june 2002. *AIP Conference Proceedings, American Institute of Physics, Melville, U.S.A.*, pages 554–557, 2003.

[31] U. Frish. *Turbulence: The legacy of A. N. Kolmogorov*. Cambridge Univ. Press, Cambridge, 1995.

[32] H. Glahn and D. A. Lowry. The use of model output statistics in objective weather forecasting. *J. Appl. Meteor.*, pages 1203–1211, 1972.

[33] L. Gomes and B. J. Vickery. On the prediction of extreme wind speeds from the parent distribution. *Journal of Industrial Aerodynamics*, pages 359–377, 1977.

[34] A. Gottschall and J. Peinke. How to improve the estimation if power curves for wind turbines. *Environ. Res. Lett.*, pages 3, 015005, 2008.

[35] E. J. Gumbel. Statistics of extremes. *Columbia University Press, New York*, 1958.

[36] J.R. Holton. *An Introduction to Dynamic Meteorology*. Number v. 1 in An Introduction to Dynamic Meteorology. Elsevier Academic Press, 2004. ISBN 9780123540157. URL `http://books.google.it/books?id=fhW5oDv3EPsC`.

[37] A.A.M. Holtslag, E.I.F. De Bruijn, and H.L. Pan. A high resolution air mass transformation model for short-range weather forecasting. *Mon. Weather Rev.*, pages 1561–1575.

[38] G.C. Holzworth. Estimates of maximum mixing depths in the contiguous united states. *Mon. Weather Rev.*, pages 235–242, 1964.

[39] IPCC. Climate change 2001: the scientific basis. *Cambridge University Press, UK*, page p 881, 2001.

[40] J. S. Irwin. A theoretical variation of the wind profile power-law exponent as a function of surface roughness and stability. *Atm. Env.*, pages 191–194.

[41] C. G. Justus, W. R. Hargraves, A. Mikhail, and Graber D. Methods for estimating wind speed frequency distributions. *J. Appl. Meteor*, pages 350–353. doi: doi:http://dx.doi.org/10.1175/1520-0450(1978)017<0350:MFEWSF>2.0.CO;2.

[42] J. C. Kaimal, J. C. Wyngaard, Y. Izumi, and O. R. Coté. Spectral characteristics of surface-layer turbulence. *Quarterly Journal of the Royal Meteorological Society*, 98(417):563–589, 1972. ISSN 1477-870X. doi: 10.1002/qj.49709841707. URL `http://dx.doi.org/10.1002/qj.49709841707`.

[43] E. Kalnay. Atmospheric modeling, data assimilation and predictability. *Cambridge University Press ISBN 0-521-79179-0-ISBN 0-521-79629*, 2002.

[44] A. N. Kolmogorov. The local structure of turbulence in incompressible viscous fluid for very large reynolds number. *Dokl. Akad. Nauk. SSSR*, pages 434, 92, 1941.

[45] S. Lagomarsino and G. Solari. The dynamic behavior under wind loads of the rozzano tower, milan, italy. *Studi e Ricerche, Scuola di Perfezionamento in Costruzione in c.a. Fratelli Pesenti, Milan Polytechnic*, pages 231–266, 1995.

[46] G. Magnus. Versuche über die spannkräfte des wasserdampfs. *Ann. Phys. Chem*, pages 225–247, 1844.

[47] G. Mastrantonio, A. P. Viola, S. Argentini, G. Fiocco, L. Giannini, L. Rossini, G. Abbate, R. Ocone, and Casonato. Observation of sea breeze events in rome and the surrounding area by a network of doppler sodars. *Boundary Layer Meteorology*, pages 67–80, 1994.

[48] D. Matsushita, H. Matsumiya, Y. Hara, S. Watanabe, and A. Furukawa. Studies on numerical site calibration over complex terrain for wind turbines. *Science China*, pages 53, 8–12, 2010.

[49] H. A. McGowan. Book reviews : Simpson, j.e. 1994: Sea breeze and local winds. *Progress in Physical Geography*, 21:622–624, 1997. doi: 10.1177/030913339702100419.

[50] A. Mellouki and A.R. Ravishankara. *Regional Climate Variability and its Impacts in the Mediterranean Area*. Nato Science Series: IV: (closed). Springer, 2007. ISBN 9781402064296. URL `http://books.google.it/books?id=sSjBwHNt244C`.

[51] P. Milan, M. Watcher, and Peinke J. Turbulent character of wind energy. *Physical Review Letter*, pages 110, 138701, 2013.

[52] A.S. Monin and A.M. Obuhov. Basic laws of turbulent mixing in the atmosphere near the ground. *Tr. Akad. Nauk, SSSR Geophiz. Inst.*, pages 1963–1987, 1954.

[53] Carla Mora. Sea breeze and local weather conditions in a coastal mediterranean mountain setting. *Weather*, 69(7):184–190, 2014. ISSN 1477-8696. doi: 10.1002/wea.2258. URL `http://dx.doi.org/10.1002/wea.2258`.

[54] D.M. Murphy and T. Koop. Review of the vapour pressures of ice and supercooled water for atmospheric applications. *Q.J.R. Meteorol. Soc.*, pages 1539–1565, 2005. doi: 10.1256/qj.04.94.

[55] P Nielsen. Klim denmark case study. *http://www.emd.dk/*, 2001.

[56] F. T. M. Niewstadt. The steady-state height and resistance laws of the nocturnal boundary layer: theory compared with cabauw observations. *Boundary-Layer Meteor.*, pages 3–17, 1981.

[57] O. Petrucci and M. Polemio. The role of meteorological and climatic conditions in the occurrence of damaging hydro-geologic events in southern italy. *Nat. Hazards Earth Syst. Sci.*, pages 105–118, 2009. doi: www.nat-hazards-earth-syst-sci.net/9/105/2009/.

[58] R.A. Pielke, W.R. Cotton, R.L. Walko, C.J. Tremback, W.A. Lyons, L.D. Grasso, M.E. Nicholls, M.D. Moran, D.A. Wesley, T.J. Lee, and J.H. Copeland. A comprehensive meteorological modeling system - rams. *Meteorology and Atmospheric Physics*, 49(1-4):69–91, 1992. ISSN 0177-7971. doi: 10.1007/BF01025401. URL `http://dx.doi.org/10.1007/BF01025401`.

[59] David C. Powell and C. E. Elderkin. An Investigation of the Application of Taylor's Hypothesis to Atmospheric Boundary Layer Turbulence. *Journal of The Atmospheric Sciences*, 31:990–1002, 1974. doi: 10.1175/1520-0469(1974)031<0990:AIOTAO>2.0.CO;2.

[60] J.V. Seguro and T.W. Lambert. Modern estimation of the parameters of the weibull wind speed distribution for wind energy analysis. *Journal of Wind Engineering and Industrial Aerodynamics*, 85(1):75 – 84, 2000. doi: http://dx.doi.org/10.1016/S0167-6105(99)00122-1.

[61] A. M. Sempreviva, T. Lofeudo, C. R. Calidonna, Courtney M., R. Wagner, E. Avolio, L. De Leo, and S. Federico. Experimental evolution of the inland vertical structure of a coastal atmospheric boundary layer in the central mediterranean using surface and ground-based remote sensing measurements. *Proceedings*, 2010.

[62] J. E. Simpsono and R. E. Britter. A laboratory model of an atmospheric mesofront. *Quarterly Journal of The Royal Meteorological Society*, 106:485–500, 1980. doi: 10.1256/smsqj.44906.

[63] J. Smagorinsky. General circulation experiments with the primitive equations. part i, the basic experiment. *Mon. Wea. Rev*, 91 (3):99–164, 1963.

[64] L. Sorriso-Valvo, V. Carbone, P. Veltri, G. Consolini, and R. Bruno. Intermittency in the solar wind turbulence through probability distribution functions of fluctuations. *Geophysical Research Letters*, pages 1801–1804, 1999.

[65] L. Sorriso-Valvo, R. Marino, V. Carbone, A. Noullez, F. Lepreti, P. Veltri, R. Bruno, B. Bavassano, and E. Pietropaolo. Observation of inertial energy cascade in interplanetary space plasma. *Phys. Rev. Lett.*, 99:115001, Sep 2007. doi: 10.1103/PhysRevLett.99.115001. URL `http://link.aps.org/doi/10.1103/PhysRevLett.99.115001`.

[66] O. G. Sutton. Micrometeorology. *McGraw-Hill, Book Co., Ink, New York*, page 333 p., 1953.

[67] L. Tiriolo, R. C. Torcasio, S. Montesanti, A. M. Sempreviva, C. R. Calidonna, and S. Federico. Forecasting wind power production from a wind farm using the rams model. *EMS Annual Meeting Abstracts, EMS2014-231-1*, 2014.

[68] L. Tiriolo, R. C. Torcasio, S. Montesanti, A. M. Sempreviva, C. R. Calidonna, and S. Federico. Real time weather forecasting in southern italy: a detailed verification. *EMS Annual Meeting Abstracts, EMS2014-17-2*, 2014.

[69] I. Troen and L Mahrt. A simple model for the atmospheric boundary layer: sensitivity to surface evaporation. *Boundary-layer Meteor.*, pages 129–148, 1986.

[70] A. P. Val Ulden and A. A. M. Holslag. Estimation of atmospheric boundary layer parameters for diffusion application. *J. Clim. Appl. Meteor.*, pages 1196–1207, 1985.

[71] AA. VV. Manual on the global telecommunication system. *WMO-No. 386*, 2007.

[72] C. D. Whiteman, X. Bian, and S. Zhong. Low-level jet climatology from enhanced rawinsonde observations at a site in the southern great plains. *Journal of Applied Meteorology*, pages 1363–1376, 1997. doi: 10.1175/1520-0450.

[73] D. S. Wilks. Statistical methods in the atmospheric sciences. *Academic Press*, 2006.

[74] G. E. Willis and J. W. Deardorff. Laboratory Observations of Turbulent Penetrative-Convection Planforms. *Journal of Geophysical Research*, 84, 1979. doi: 10.1029/JC084iC01p00295.

[75] J. C. Wyngaard and S. F. Clifford. Taylor' s hypothesis and hight-frequency turbulence spectra. *Journal of The Atmospheric Sciences*, 34:922–929, 1977. doi: 10.1175/1520-0469(1977)034<0922:THAHTS>2.0.CO;2.

[76] A. M. Yaglom. Local structure of the temperature field in a turbulent flow. *Dokl. Akad. Nauk SSSR*, pages 743–746, 1949.

[77] S. Zhong and S. Takle, E. The effects of large-scale winds on the sealand-breeze circulations in an area of complex coastal heating. *J.Appl. Meteor.*, pages 1181–1195. doi: http://dx.doi.org/10.1175/1520-0450(1993)032<1181:TEOLSW>2.0.CO;2.

[78] C. D. Zilitinkevich, X. Bian, and S. Zhong. On the determination of the height of the ekman boundary layer. *Boundary-layer Meteor.*, pages 141–145.